

Numerical Analysis of Fluid-Structure Interaction in The Aortic Arch Considering Various Blood Flow Rates

Hamid Zandvakili, Kamran Hassani*, Siamak Khorrammehr

Department of Biomedical Engineering, College of Medical Science and Technologies, Tehran Science and Research Branch, Islamic Azad University, Tehran, Iran

E-mail: dr.zandvakili@gmail.com, k.hasani@srbiau.ac.ir, s.khorrammehr@srbiau.ac.ir

*Corresponding author

Received: 7 February 2023, Revised: 26 July 2023, Accepted: 10 April 2023

Abstract: Hemodynamic forces are felt by the biomechanical receptors of the arterial wall to give an appropriate response to maintain homeostasis. On the other hand, baroreceptors are a type of biomechanical receptors that are sensitive to abnormal stretch sizes. It is very important to predict the distribution of stress and strain caused by the hemodynamic field to the vessel wall in pressure-sensitive areas to evaluate the function of these receptors. In the present study, a three-dimensional (3-D) model of the aortic arch is presented. The geometry was reconstructed based on the CT images. Also, numerical analysis was performed using the fluid-structure interaction method. First, the hemodynamic field containing the pressure and velocity distribution in the blood area was obtained. Then, the deformation and stress fields in the solid domain were analyzed. The results show that the highest vertical stress occurs in the posterior supra aorta. So, the amount of this maximum vertical stress increases up to 5 kPa in some places; these points have higher tensions, and they can be susceptible to rupture and aneurysm diseases. Higher normal stress happened at the aortic root and the supra-aortic branches and reached approximately 200 kPa at Peak Systole. Also, the highest amount of strain occurs in the posterior supra aorta, reaching 0.001.

Keywords: Aortic Arch, FSI Method, Hemodynamics, Numerical Modeling, Perfusion

Biographical notes: **Hamid Zandvakili** received his BSc in Mechanical Engineering from Shahid Bahonar University of Kerman. He received his MSc in biomechanics from the Science and Research Branch of Islamic Azad University and is currently a PhD candidate in biomechanical and biomedical engineering at this university. **Kamran Hassani** received his PhD in biomedical engineering from Amirkabir University. He is currently an associate professor at the Science and Research Branch of Islamic Azad University. His field of research is mainly cardiovascular system biomechanics. **Siamak Khorrammehr** received his PhD in biomedical engineering from the Science and Research Branch of Islamic Azad University. He is currently an Assistant Professor in Medical Sciences and Technologies at the Science and Research Branch of Islamic Azad University. His field of research is mainly biomechanics, ergonomics, and rehabilitation engineering.

Research paper

COPYRIGHTS

© 2024 by the authors. Licensee Islamic Azad University Isfahan Branch. This article is an open access article distributed under the terms and conditions of the Creative Commons Attribution 4.0 International (CC BY 4.0)

<https://creativecommons.org/licenses/by/4.0/>



1 INTRODUCTION

Cardiovascular diseases are one of the common diseases in today's societies that can be caused by problems in the blood vessels and the behavior of the blood in the veins. In order to recognize these diseases, there must be enough information about the behavior of the blood, such as changes in blood pressure and velocity profiles, as well as changes in tension and changes in the shape of the walls of the vessels. On the other hand, the baroreflex is a homeostasis mechanism of the body that is used to keep blood pressure constant. This reflex is involuntary and is considered a quick self-regulation. The baroreceptor system plays an important role in the short-term regulation of blood pressure, which is mediated by baroreceptors. These receptors are located in the carotid arteries, the aortic arch, and the walls of the heart cavities and are activated in response to the increase in blood pressure. High blood pressure causes the heart rate to decrease, and then the blood pressure decreases. Low blood pressure reduces the activity of the baroreceptor reflex, and as a result, heart rate and blood pressure increase. Our current knowledge of identifying different components of the baroreceptor reflex is the result of numerous preliminary studies that have been carried out on humans and animals. Although the importance of baroreceptors in the control of arterial pressure under resting conditions has never been doubted, there are disagreements about how they function, considering various blood flow rates.

Donald and Edis, in their research on the isolated carotid baroreceptors of dogs, showed for the first time that the baroreflex performance curve undergoes a re-adjustment during exercise compared to the resting state without changing the sensitivity of the baroreceptors [1]. Later studies confirmed this finding in humans and showed that the amount of this re-regulation has a direct relationship with the intensity of exercise. Feng et al. and his colleagues conducted studies on the numerical modeling of aortic arch baroreceptors. They combined finite element modeling with laboratory work on the aortic arch of a rat. Numerical simulation in this study could show the functional role of axial loading in the baroreceptor region of the aortic arch. The laboratory studies that were done on the aortic arch of the mouse confirmed the validity of the numerical simulation [2-6]. Lee et al. proposed the CFD method on several carotid bifurcations and illustrated how the zones interacted with the connection among the geometric construction and flowed fluctuation as oscillatory shear parameters [7]. Also, Dong et al. performed blood flow downstream at the carotid branches, resulting from the downstream arterial impedance [8]. According to the FSI analysis of the aortic wall, the study of Suito et al. is performed on the thoracic aorta of the human vascular system. They constructed the geometry of the aorta based on CT images and

concentrated on the connection of the WSS distribution in the centerline [9]. Lantz et al. carried out an FSI model of the human aorta using MRI images. They simulated the impact of arterial wall movement on WSS variation by considering the outcomes related to rigid arterial wall results [10]. In this regard, Crosetto et al. proposed similar mathematical modeling with an identical approach. The boundary conditions applied for the vessel outlets were received results in a one-dimensional simulation [11]. In the current study, a three-dimensional aortic arch model is presented as considering various blood flow rates. The mathematical modeling was considered by the FSI method to reach the hemodynamic forces applied to the arterial vessel wall and results in abnormal stresses. Also, more fluid details were analyzed concerning average peak and mean blood velocities corresponding to the ascending aorta inlet blood flow with respect to the previous literature review. Simulation models of different parts of the carotid vascular system have been presented in recent years [12]. A three-dimensional and accurate mathematical model can help to investigate the baroreflex system's performance accurately. The present study investigated a three-dimensional aortic arch model as the expected maximum stress and deformation locations, considering various blood flow rates.

2 METHOD AND MATERIALS

This research intends to quantitatively study the deformation of the aortic wall by creating an accurate three-dimensional model that considers the properties using the fluid-structure interaction (FSI) method. In order to simulate the arteries of the human body, the real dimensions were determined using Mimics software, which modeled the arteries obtained from the positron emission tomography-computed tomography (PET-CT) imaging method. In order to simulate the arteries of the human body, the real dimensions have been determined using Mimics software from the modeling of the arteries obtained from the positron emission tomography-computed tomography (PET-CT) imaging method. Then, the CT scan was transferred to computational fluid dynamics software for the fluid flow part, as well as finite element software for the solid part; modeling and factors such as stress, strain, and deformation were studied. For numerical simulations, the direct interaction between blood and the solid wall of the vessel is used. Strains and deformations will be desired to calculate the response of the flexible vessel wall. While considering the externally applied loads, the velocity, acceleration, and displacement vectors in the vessel domain, along with the pressure and flow fields, are calculated by solving the Equations of motion in the fluid domain. Also, the blood flow in the vessels of the human body is considered a

Newtonian fluid that obeys the dynamic relationships of fluids with specific density and viscosity. Solving the governing Equations in solid-fluid interaction problems is similar to fluid problems with moving boundaries.

2.1. Governing Equations of The Fluid Region

The governing Equations of blood flow are the mass continuity and momentum conservation Equations. The law of conservation of mass is generally expressed as “Eq. (1)”.

$$\frac{\partial \rho}{\partial t} + \frac{\partial(\rho u_i)}{\partial x_i} = 0 \quad (1)$$

In three-dimensional flow $i = 1, 2, 3$, ρ is density, \mathbf{u} is velocity, and \mathbf{t} is time. The momentum Equation in its general form for incompressible flow and constant viscosity is given by “Eq. (2)”.

$$\rho \left(\frac{\partial u_i}{\partial t} + \frac{\partial(u_i u_j)}{\partial x_j} \right) = - \frac{\partial p}{\partial x_i} + \mu \frac{\partial}{\partial x_i} \left(\frac{\partial u_i}{\partial x_j} + \frac{\partial u_j}{\partial x_i} \right) + \rho f_i \quad (2)$$

In this Equation, f_i is the volumetric force on the fluid flow, which can represent the forces acting on the fluid due to gravity.

2.2. Equations Governing the Solid Region of The Vessel

Solving the solid field in problems that include fluid-structure interaction is the same as solid problems, with the difference that after each step of solving the fluid field and its convergence, the forces acting on the solid must also be updated. In the problems of fluid-structure interaction, the solid medium generally exhibits non-linear behavior. The computational domain in fluid-structure interaction problems with dynamic elastic Equations, which include the momentum Equation and the equilibrium Equation, is described by the momentum “Eq. (3)” and the equilibrium “Eq. (4)”.

$$\rho \frac{\partial^2 \mathbf{d}}{\partial t^2} = \frac{\partial \sigma_{ij}}{\partial x_j} + \rho \mathbf{f}_i \quad (3)$$

$$\sigma_{i,j} \times n_j = \tau_i^s \quad (4)$$

In these Equations, ρ is the density of the solid substance, $\partial^2 \mathbf{d} / \partial t^2$ represents the acceleration of the point mass of the solid, \mathbf{d} is the displacement of the point mass, $\boldsymbol{\sigma}$ is the Cauchy stress tensor, \mathbf{f} is the external forces applied at time \mathbf{t} , τ_i^s is the stresses applied to the external surface at time \mathbf{t} , and \mathbf{n} is the normal vector to the surface.

2.3. Fluid-Structure Interaction

In order to achieve more realistic results, the physical conditions governing the problem must be fully considered. In the analysis of problems, considering the interaction of fluid and solid, the effect of flow on the

wall and the effect of the deformation of the solid wall on the movement of the fluid is considered. In this type of analysis, two separate models are prepared, and the computational domain is divided into two parts: fluid domain and solid domain. When solving these two domains, they should be coupled together and solved simultaneously. The solid model is based on the Lagrangian system. In the Lagrangian view, the motion of a single particle is followed, and its displacement is unknown. The fluid model alone is always analyzed with the Eulerian coordinate system. For fluid-solid interaction problems, a combination of Eulerian and Lagrangian perspectives should be used, which is known as the arbitrary Lagrangian-Eulerian system (ALE). In fact, the Eulerian point of view is used for fluid domain Equations, the Lagrangian point of view is used for solid Equations, and the ALE point of view is used for common boundaries of solid and fluid. In fluid-structure interaction problems, the stresses and deformations of the solid domain are calculated simultaneously with the flow parameters that are in contact with the solid domain. In other words, the changes in the shape of the solid domain are caused by fluid pressure gradients, and in a similar way, the pressures and velocities in the fluid domain are also dependent on the changes in the shape of the solid domain structure.

2.4. Computational Model-Building Steps

The geometry used in this project is from hospital images in DICOM format, which are taken in two dimensions from the body of a healthy person. After importing in the Mimics software, the complete geometry of the cardiovascular system is imaged by specifying the range of rays irradiated to the patient's body and based on the soft tissue, which includes the cardiovascular system as well as the respiratory system. By adjusting the lower and upper limits of the pixels, the images can be seen. Then, by selecting the geometry of the cardiovascular system, which includes the ventricles, atria, and aorta, as well as blood vessels and pulmonary vessels, it was extracted separately, as shown in “Fig. 1”.

2.5. Geometry and Boundary Conditions

Based on the research of Gabe et al. [13], the maximum and minimum average blood velocity in the ascending aorta is 0.66 cm/s and 0.11 cm/s . Current studies consider three velocities of 0.66 cm/s , 0.385 cm/s , and 0.11 cm/s for blood flow simulation [14]. The blood flow at the velocity of 0.11 cm/s is laminar. However, the blood flow at the velocities of 0.66 cm/s and 0.385 cm/s the blood flow is turbulent. The present study is simulated with the $k - \epsilon$ turbulence model based on the study of James et al. [15]. Based on the assumption of Vinoth et al. [16], boundary condition data related to a relative pressure of 120 mm Hg is assumed at all aortic branch outlets. Blood density is 1050 kg/m^3 , and its dynamic viscosity is 0.0035 Ns/m^2 . Based on

Giannakoulas et al.'s study [17], Young's modulus is equal to 4.66 Mpa, Poisson's ratio is 0.45, and a density of 1062 kg/m³ was considered. For all inlets and outlets, the fixed support boundary condition is applied [18]. The amount of displacement in fixed support boundary conditions is zero.

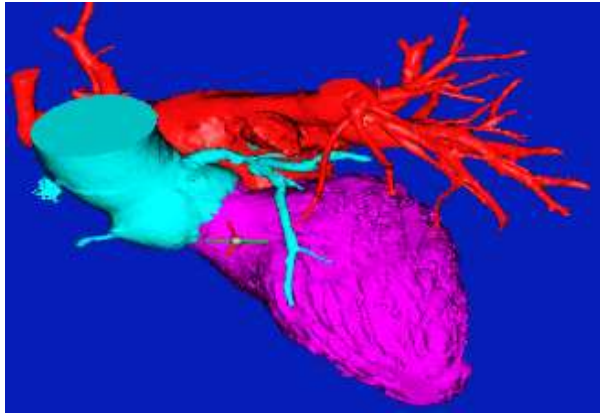


Fig. 1 The generated geometry of the cardiovascular system extracted by Mimics software for a 45-year-old male.

2.6. Mesh Construction

Due to the curved geometry of the blood vessel and its asymmetry during grid generation, it has been tried to use the meshing of tetrahedral elements and boundary layer elements in the vessel wall to achieve more accurate results. The total number of meshes used is selected after checking meshing independence. The grid is made with average Orthogonal Quality=0.78, Skewness=0.21, and Aspect Ratio=1.80 ("Fig. 2").



Fig. 2 The geometry of the aorta and the mesh created in the computational model.

In this simulation, the mesh sensitivity analysis was studied. It needs a mesh sensitivity analysis to ensure the problem is independent of the mesh size. In this research, several mesh samples with different sizes and inflation mesh on the vessel walls with a growth rate of 1.2 have been used to achieve better results. Current results considered the amount of equivalent pressure created at

the vessel wall as a criterion for the appropriateness of the number of calculation elements, as shown in "Fig. 3".

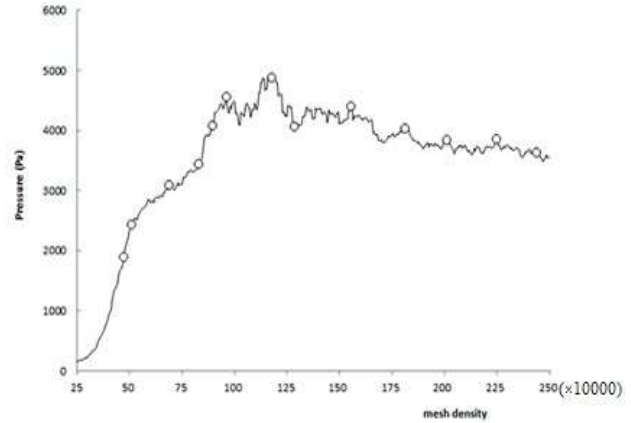


Fig. 3 Mesh sensitivity analysis in the computational model.

The measured maximum and minimum pressure at each location are shown in "Table 1". The measured pressures are relatively low, which is probably due to the patient being anesthetized (part of the standard clinical procedure). The pressure drops, as opposed to the absolute pressure, define the flow through the vessel in the absence of interaction between the fluid and the mechanical properties of the vessel wall; thus, the relatively lower magnitude of the measured pressures would not affect the predicted flow under the present simulation conditions. Table 1 shows that the individual values of Pmax and Pmin at each outlet are within 6% of the pulse pressure. The pulse pressure at each outlet is within 3.5%. In the AA, the maximum pressure is close to the value measured and the mismatch for minimum pressure is 8% of the pulse pressure. Two additional invasive measurements in the distal arch and mid-abdominal aorta (in the TL) were compared with the CFD values for further validation. These were found to be in close agreement as shown in "Table 1" [19].

Table 1 Minimum and maximum pressure values at various locations throughout the domain, measured experimentally and derived from the simulations. The boundaries are labelled: AA-ascending aorta, BT-brachiocephalic trunk, LCC - left common carotid artery, LS-left subclavian artery, DA-descending aorta

	Pressure	AA	BT	LCC	LS	DA
Exp.	P _{min}	56	50	50	N/A	52
	P _{max}	103	97	96	N/A	99
CFD	P _{min}	52.7	52	51.9	52.3	51.1
	P _{max}	103.3	97.9	97.3	97.6	98.1

3 RESULTS AND DISCUSSION

This research used the FSI method based on the leading models obtained from the aorta by real images obtained from PET-CT imaging devices. After running in the Mimics software for modeling based on the actual dimensions and geometry of the vessel, the obtained model is transferred to the Ansys software for analysis and is analyzed in different conditions using the finite volume method. In the present study, blood is considered a Newtonian, incompressible, and isothermal fluid, which is continuous. In simulating the geometry of the aorta, the continuity and Navier-Stokes Equation are the governing Equations for the 3-D blood movement. Also, the boundary condition of the fluid and solid interaction introduces forces from the blood side to the vessel wall. This section draws the pressure and velocity contours for the blood flow domain and the deformation, strain, and stress contours for the vessel's solid domain. These contours are drawn for three blood inflow velocities of 11 cm/s, 38.5 cm/s, and 66 cm/s. Figure 4 shows the static pressure contours in the middle and transverse planes. The maximum amount of pressure occurs in the supra-aorta, reaching 16.04 kPa, 16.41 kPa, and 17.32 kPa at velocities of 11 cm/s, 38.5 cm/s, and 66 cm/s, respectively. Baroreceptors are located at the place of application of this maximum pressure. Also, the lowest pressure occurs in the descending aorta, and the minimum amount at the velocities of 11 cm/s, 38.5 cm/s, and 66 cm/s is 15.98 kPa, 15.84 kPa, and 15.58 kPa, respectively. Therefore, in the descending aorta, the low-pressure area causes blood to be sucked toward the abdominal aorta.

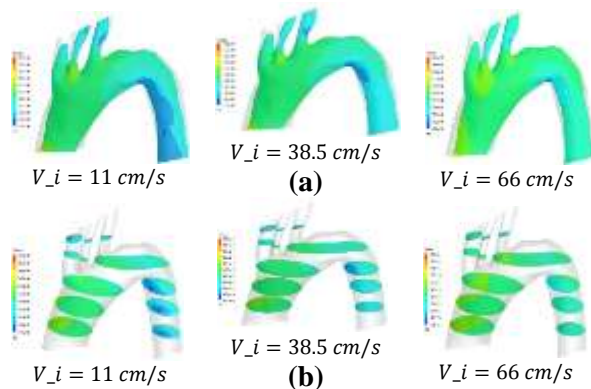


Fig. 4 Static pressure contour at different inlet velocities to the aorta for: (a): middle plane, and (b): transverse planes.

Figure 5 shows the instantaneous velocity contours in the middle and transverse planes. The highest instantaneous velocity occurs in the supra-aorta, and these amounts in inlet velocities of 11 cm/s, 38.5 cm/s, and 66 cm/s reach 0.31 m/s, 1 m/s, and 1.7 m/s, respectively. Also, the lowest instantaneous velocity occurs in the internal arch

of the ascending aorta and the internal arch of the descending aorta, so the instantaneous velocity reaches zero at some points.

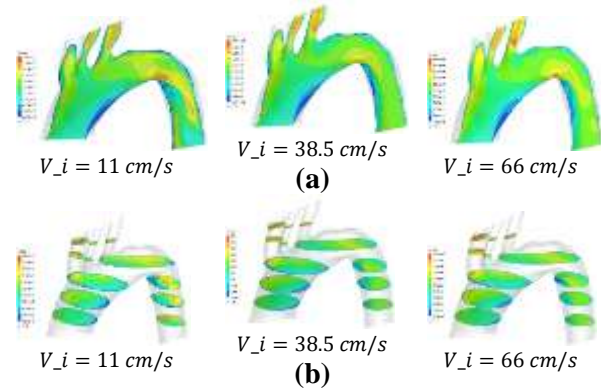


Fig. 5 Instantaneous velocity contour at different inlet velocities to the aorta for: (a): middle plane, and (b): transverse planes.

Figure 6 presents the contours of normal stress and wall strain. The highest normal stress occurs in the posterior supra aorta. So, the amount of this maximum vertical stress increases up to 5 kPa in some places; these points have higher tensions and can be susceptible to rupture and aneurysm diseases. This could be an area of potential aneurysm development based on clinical evidence of rupture locations. Also, the highest strain occurs in the posterior supra aorta, reaching 0.001. Figures 6a and 6b show almost the same distributions because of the direct relation between stress and wall strain alteration.

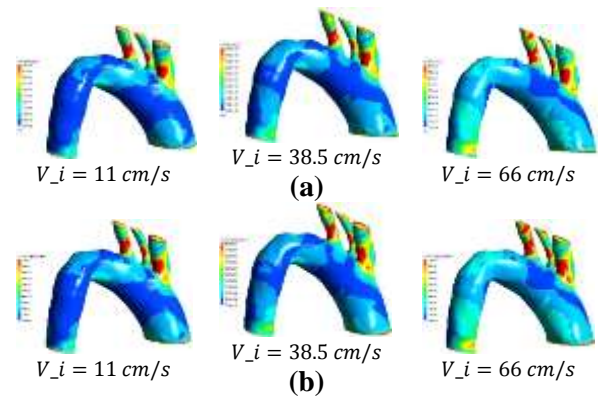


Fig. 6 Normal stress and wall strain contours at different inlet velocities to the aorta for: (a): normal stress, and (b): wall strain.

Baroreceptors are usually located in the adventitia layer of the aortic arch. Aging is usually accompanied by a hardening of the arterial walls or atherosclerosis, which leads to a decrease in the ability of blood pressure receptors to heart rate and control blood pressure [20-21]. Therefore, the factor that determines the location of baroreceptors can be the maximum normal stress, which

can be calculated by solving the problem in the form of fluid and structure interaction in the vessel wall. Hence, the value of Young's coefficient of the vessel wall plays a key role in determining the location of baroreceptors.

4 CONCLUSIONS

This research investigates the blood flow and wall shape changes in the aorta during different blood flow rates as much as possible. Steady flow with a Newtonian fluid in a realistic aorta geometry was investigated. This enables us to investigate more complex boundary conditions in the future than what is used in this research. It has also been tried to better understand flow physics by producing suitable results. In this regard, various flow parameters, such as blood velocity, blood pressure, stress, and strain on the vessel wall, were investigated from different views. The results show that the highest vertical stress occurs in the posterior supra aorta. So, the amount of this maximum vertical stress increases up to 5 kPa in some places; these points have higher tensions, and they can be susceptible to rupture and aneurysm diseases.

REFERENCES

- [1] Donald, D. E., Edis, A. J., Comparison of Aortic and Carotid Baroreflexes in the dog, *J. Physiol*, Vol. 215, No. 2 1971, pp. 521-38, Doi: 10.1113/jphysiol.1971.sp009483.
- [2] Feng, B., Li, B. Y., Nauman, E. A., and Schild, J. H., Theoretical and Electrophysiological Evidence for Axial Loading About Aortic Baroreceptor Nerve Terminals in Rats, *Am J Physiol Heart Circ Physiol*, Vol. 293, No. 6, 2007, pp. 3659-72.
- [3] Carlson, B. E., Arciero, J. C., and Secomb, T. W. Theoretical Model of Blood Flow Autoregulation: Roles of Myogenic, Shear-Dependent, And Metabolic Responses, *American Journal of Physiology-Heart and Circulatory Physiology*, Vol. 295, No. 4, 2008, pp. 1572-1579,
- [4] Rizzo, D. C., *Fundamentals of Anatomy and Physiology*, Cengage Learning, 2015.
- [5] Bisognano, J., Sloand, J., Papademetriou, V., Rothstein, M., Sica, D., Flack, J., and Cody, R. J., An Implantable Carotid Sinus Baroreflex Activating System for Drug-Resistant Hypertension: Interim Chronic Efficacy Results from The Multi-Center Rheos Feasibility Trial, 2006.
- [6] Kroon, A., Schmidli, J., Scheffers, I., Tordoir, J., Mohaupt, M., Allemann, and De Leeuw, P., Sustained Blood Pressure Reduction by Baroreflex Activation Therapy with A Chronically Implanted System: 4-Year Data of Rheos Debut-Ht Study in Patients with Resistant Hypertension: 9D. 01, *Journal of Hypertension*, Vol. 28, No. 441, 2010.
- [7] Lee, S. W., Antiga, L., Spence, J. D., and Steinman, D. A., Geometry of the Carotid Bifurcation Predicts Its Exposure to Disturbed Flow, *Stroke* Vol. 39, No. 8, 2008, pp. 2341-7.
- [8] Dong, J., Wong, K. K. L., and Tu, J., Hemodynamics Analysis of Patient- Specific Carotid Bifurcation: a CFD Model of Downstream Peripheral Vascular Impedance, *Int J Numer Method Biomed Eng*, Vol. 29, No. 4, 2023, pp. 476-91.
- [9] Suito, H., Takizawa, K., Huynh, V. Q. H., Sze, D., and Ueda, T., FSI Analysis of The Blood Flow and Geometrical Characteristics in The Thoracic Aorta, *Comput Mech*, Vol. 54, No. 4, 2022, pp. 1035-45.
- [10] Lantz, J., Renner, J., and Karlsson, M., Wall Shear Stress in A Subject Specific Human Aorta—Influence of Fluid-Structure Interaction. *Int. J. Appl Mech*, Vol. 3, No. 04, 2021, pp. 759-78.
- [11] Crosetto, P., Reymond, P., Deparis, S., Kontaxakis, D., Stergiopoulos, N., and Quarteroni, A., Fluid-Structure Interaction Simulation of Aortic Blood Flow. *Comput Fluids*, Vol. 43, No. 1, 2021, pp. 46-57.
- [12] Klabunde, R., *Cardiovascular Physiology Concepts*, Lippincott Williams & Wilkins, 2011.
- [13] Kougiyas, P., Weakley, S. M., Yao, Q., Lin, P. H., and Chen, C., Arterial Baroreceptors in The Management of Systemic Hypertension, *Med Sci Monit Int Med J Exp Clin Res*, Vol. 16, No. 1, RA1, 2010.
- [14] Gabe, I. T., Gault, J. H., Ross, J. Jr., Mason, D. T., Mills, C. J., Schillingford, J. P., and Braunwald, E., Measurement of Instantaneous Blood Flow Velocity and Pressure in Conscious Man with A Catheter-Tip Velocity Probe, *Circulation*, Vol. 40, No. 5, 1969, pp. 603-14.
- [15] James, M. E., Papavassiliou, D.V., and O'Rear, E. A., Use of Computational Fluid Dynamics to Analyze Blood Flow, Hemolysis and Sublethal Damage to Red Blood Cells in a Bileaflet Artificial Heart Valve, *Fluids*, Vol. 4, No. 19. 2019, <https://doi.org/10.3390/fluids4010019>.
- [16] Vinoth, R., Kumar, D., Raviraj, A., and Vijay Shankar C. S., Non-Newtonian and Newtonian blood flow in human aorta: A transient analysis, *Biomedical Research (India)*, Vol. 28, 2016.
- [17] Giannakoulas, G., Giannoglou, G., Soulis, J., Farmakis, T., Papadopoulou, S., Parcharidis, G., and Louridas, G., A Computational Model to Predict Aortic Wall Stresses in Patients with Systolic Arterial Hypertension, *Med Hypotheses*, Vol. 65, No. 6, 2005, pp. 1191-5, Doi: 10.1016/j.mehy.2005.06.017. Epub 2005 Aug 16. PMID: 16107302.
- [18] Kass, J. S., Mizrahi, E. M., *Neurology Secrets E-Book*. Elsevier Health Sciences, 2016.
- [19] Heesch, C. M., Reflexes that Control Cardiovascular Function, *Adv Physiol Edu*, Vol. 277, No. 6, 1999, pp. 234.
- [20] Klabunde, R., *Cardiovascular Physiology Concepts*, Lippincott Williams & Wilkins, 2011, pp. RA1-8.
- [21] Kougiyas, P., Weakley, S. M., Yao, Q., Lin, P. H., and Chen, C., Arterial Baroreceptors in The Management of Systemic Hypertension, *Med Sci Monit Int Med J Exp Clin Res*, Vol. 16, No. 1, 2010, RA1.

The Effect of Boundary Conditions and Concentrated Mass on The Performance and Vibration Results of Piezoelectric Bimorph Beam by Parallel and Series Layers

Majid Jabbari*

Department of Mechanical Engineering, Khomeinishahr Branch, Islamic Azad University, Khomeinishahr /Isfahan, Iran,
E-mail: jabbari@iaukhsh.ac.ir

*Corresponding author

Sofia Jabbari

Isfahan Healthcare Center, University of Applied Sciences and Technology, Isfahan, Iran
E-mail: jabbari_nik@yahoo.com

Received:25 October 2022, Revised:10 March 2023, Accepted:26 April 2023

Abstract: A variety of parameters influence the performance of piezoelectric sensors and actuators, such as support and concentrated mass. This paper presents a finite element formulation for piezoelectric structures and studies the effect of parameters on them. This method was developed based on the Bernoulli-Euler beam and the model is considered for use as a beam structure using the Variation Principle. The model was used for static and vibration analysis. The effects of support on the deflection of the piezoelectric beam were studied. Modal analysis was also carried out for the electromechanical coupling and uncoupling beams, and the effect of the concentrated mass was deduced. The finite element model was developed with FORTRAN programming Language and was implemented with MATLAB software. A comparison of the results between the analytical method, engineering software, and this program, showed acceptable accuracy.

Keywords: Actuator, Finite Element, Frequency, Piezoelectric Beam, Support

Biographical notes: **Majid Jabbari** is an assistant professor at the Department of Mechanical Engineering in Islamic Azad University, Khomeinishahr Branch. His current research interests are in the field of intelligent piezoelectric structures and computer-aided design and engineering. **Sofia Jabbari** is studying in the field of medical equipment at Isfahan Healthcare Center at University of Applied Sciences and Technology. His current research interest is the field of smart structures in medical.

Research paper

COPYRIGHTS

© 2024 by the authors. Licensee Islamic Azad University Isfahan Branch. This article is an open access article distributed under the terms and conditions of the Creative Commons Attribution 4.0 International (CC BY 4.0)

<https://creativecommons.org/licenses/by/4.0/>



1 INTRODUCTION

The behavior of piezoelectric structures has been extracted by the coupling of electrical and mechanical parameters. In order to study this model, the finite element method can be applied. Finite element formulations for modeling piezoelectric structures have been used in many studies.

The first application of the finite element of the piezoelectric model was extracted by Allik and Hughes [1]. Zemcik [2] developed a piezoelectric shell element and implemented it with ANSYS software. Lazarus [3] presented a finite element model for the nonlinear vibrations of piezoelectric layered beams with application in NEMS. The element for the modeling of smart structures was studied by Kogl and Bucalem [4]. This element was then used by Lazarus [3]. Piefort and Preumont [5] used the Mindlin shell elements for piezoelectric materials. The response can respond in the low amplitude solution to harmonic excitation; Sebald et al. [6] suggested a method to excite the system to jump to the high amplitude solution for broadband piezoelectric energy harvesting. Erturk and Inman [7] investigated the dynamic response, including the chaotic response on high-energy orbits of the bistable Duffing oscillator with electromechanical coupling. Friswell et al [8] proposed a cantilever beam with a tip mass that is mounted vertically and excited in the transverse direction at its base. This device was highly non-linear with two potential wells for large tip masses when the beam was buckled. Bendigeri et al [9] developed finite elements for the dynamic analysis of a structure with the piezoelectric property. An eight noded isoparametric three-dimensional hexahedral element was improved to model the coupled electro-mechanical behavior. In this work, the effects due to piezoelectric for the developed finite element are explained. Ghayour and Jabbari [10] presented the effect of support and concentrated mass on the performance of a piezoelectric beam actuator and frequencies through the finite element method. They also developed a new formulation for coupling beam elements on the numerical solution of the dynamic behavior of nonlinear piezoelectric beams [11].

Jabbari et al [12] studied the energy harvesting of a multilayer piezoelectric beam in resonance and off-resonance cases. They showed that the maximum value of electric power occurs at the optimum resistive load for the selected frequency value and the behavior of energy harvesting depends greatly on the excitation frequency.

Jabbari et al [13] presented the experimental and numerical results of the dynamic behaviour of a nonlinear piezoelectric beam. They showed the effects of the excitation velocity and the position of the concentrated mass on the output voltage.

The effect of strain nodes on the energy harvesting of the cantilever piezoelectric beam with the vibration mode excitation was presented by Jabbari [14]. This research showed that the resistive load affects the voltage and generated power and the optimum resistive load is considered for segmented and continuous electrodes, and then the power output is verified.

Jabbari and Ahmadi [15] studied the electric response of piezoelectric beam using the dynamic stiffness method. In this research, the dynamic stiffness matrix is developed for a two-segmented beam with a tip mass.

Hassannejad et al [16] presented the influence of non-circular cross-section shapes on the torsional vibration of a micro-rod. They demonstrated that the natural frequency of the micro-rod is completely affected by the shape and aspect ratio of the cross-section. These results can be useful in the micro-structure design stage.

Shameli et al [17] studied free torsional vibration analysis of nanorods with non-circular cross-sections. They showed that a small reduction can be observed in the natural frequencies by increasing cross-sectional dimensions.

The element developed within this paper is considered as beam. The node of the beam element has four degrees of freedom. The model presented was developed for piezoelectric actuators and sensors. The object of this research is to study model behavior under variable support and the concentrated mass effect on the frequency analysis of piezoelectric beam. These parameters influence the performance factor for energy harvesting. The results of the developed research are compared with the results of analytical and engineering software.

2 THE FINITE ELEMENT MODEL FOR THE PIEZOELECTRIC BEAM

The model of the beam is a piezoelectric bimorph which can be used as an actuator and sensor. The proposed element contains two nodes, and each node has two structural degrees of freedom (u, θ), and two electrical degrees of freedom ϕ and ψ ("Fig. 1"). The deflection function $u(x)$, and electrical potential ϕ across the beam length and thickness are evaluated by "Eq. (1)" [2].

$$u(x) = [N^u] \{\hat{u}\} \quad \phi = [N^\phi] \{\hat{\phi}\}$$

$$\{\hat{u}\} = \{u_n \quad \theta_n \quad u_{n+1} \quad \theta_{n+1}\}^T$$

$$\{\hat{\phi}\} = \{\phi_n \quad \psi_n \quad \phi_{n+1} \quad \psi_{n+1}\}^T$$

$$[N^u] = [N^{1u} \quad N^{1\theta} \quad N^{2u} \quad N^{2\theta}]$$

$$[N^\phi] = [N^{1\phi} \quad N^{1\psi} \quad N^{2\phi} \quad N^{2\psi}]$$

(1)

Where $\{\hat{u}\}$, is the displacement vector of the nodes, $\{\hat{\phi}\}$, is the nodes potential, $[N^u]$ shows the shape functions of structural degrees of freedom (u, θ) and $[N^\phi]$, shows the shape functions of electrical degrees of freedom (ϕ, ψ). The strain S , and the electric field vector $\{E\}$, can be expressed as “Eq. (2)”.

$$S = [B^u] \{\hat{u}\} \quad \{E\} = -[B^\phi] \{\hat{\phi}\} \quad (2)$$

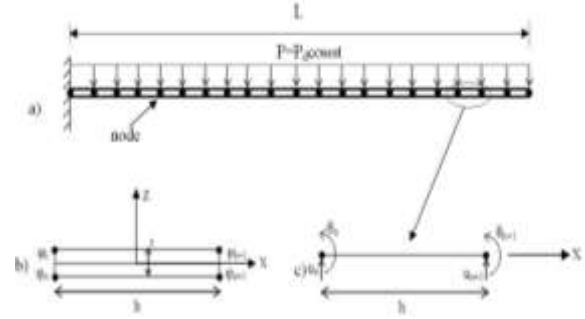


Fig. 1 (a): The finite element model of the piezoelectric beam, (b): Nodes potential degrees of freedom, and (c): Nodes displacement degrees of freedom.

$$[B^u] = z \frac{d^2}{dx^2} [N^u] = z \left[\frac{6}{h^2} \left(\frac{2x}{h} - 1 \right) \quad \frac{-2}{h} \left(\frac{3x}{h} - 2 \right) \quad \frac{6}{h^2} \left(-\frac{2x}{h} + 1 \right) \quad \frac{-2}{h} \left(\frac{3x}{h} - 1 \right) \right] \quad (3)$$

$$[B^\phi] = -\nabla [N^\phi] = - \begin{Bmatrix} \frac{\partial}{\partial x} \\ \frac{\partial}{\partial z} \end{Bmatrix} [N^\phi] = \begin{bmatrix} \frac{1}{2h} + \frac{1}{2hH} z & \frac{1}{2h} - \frac{1}{2hH} z & -\frac{1}{2h} - \frac{1}{2hH} z & -\frac{1}{2h} + \frac{1}{2hH} z \\ \frac{1}{2H} + \frac{1}{2hH} x & \frac{1}{2t} - \frac{1}{2hH} x & -\frac{1}{2hH} x & \frac{1}{2hH} x \end{bmatrix} \quad (4)$$

Where $[B^u]$ and $[B^\phi]$ are the shape function derivatives, H is the thickness and h is the element length. The motion Equations of a piezoelectric structure are obtained with the Hamilton principle. The finite element

formulation can be derived with motion Equation. (“Eq. (5)”, “Eq. (6)”) [3].

$$[m] \{\ddot{u}^n\} + [K^{uu}] \{u^n\} + [K^{u\phi}] \{\phi^n\} = \int_V [B^u]^T \{T^r\} dV + \int_V [N^u]^T \{B\} dV + \int_S [N^u]^T \{t\} dS. \quad (5)$$

$$[K^{\phi u}] \{u^n\} + [K^{\phi\phi}] \{\phi^n\} = - \int_V [B^\phi]^T \{D^r\} dV - \int_V [N^\phi]^T q^v dV - \int_S [N^\phi]^T q^s dS. \quad (6)$$

$$[K^{uu}] = \int_V [B^u]^T [c^E] [B^u] dV$$

$$[K^{u\phi}] = \int_V [B^u]^T [e] [B^\phi] dV.$$

$$[K^{\phi u}] = \int_V [B^\phi]^T [e] [B^u] dV$$

$$[K^{\phi\phi}] = - \int_V [B^\phi]^T [\varepsilon^S] [B^\phi] dV$$

$$[m] = \int_V [N^u]^T \rho [N^u] dV$$

$$\{T^r\} = [c^E] \{S^r\}$$

$$\{D^r\} = -[e]^T \{S^r\} + \{P^r\}$$

Where $\{S^r\}$, is residual strain, $\{P^r\}$ is residual polarization, $[c^E]$, is elasticity tensor under a constant

electric field, $[e]$, is piezoelectric stress matrix, $[\varepsilon^S]$ is the dielectric matrix, $\{D^r\}$: residual displacement of

electric, E is the electric field, $\{T^r\}$: residual stress tensor, $\{B\}$: body load, $\{t\}$: surface load, ρ : mass density and q^v , q^s : electric charges per volume and area. $[K^{u\phi}]$ for the series connection of the piezoelectric layers is presented in “Eq. (7)”.

$$[K^{u\phi}] = 2eb \begin{bmatrix} \frac{H}{4h} & \frac{H}{4h} & \frac{H}{4h} & \frac{-H}{4h} \\ \frac{H}{4} + \frac{5H^2}{24h} & -\frac{H}{4} + \frac{5H^2}{24h} & \frac{-H^2}{24h} & \frac{-5H^2}{24h} \\ \frac{-H}{4h} & \frac{-H}{4h} & \frac{-H}{4h} & \frac{H}{4h} \\ \frac{-H}{2} + \frac{5H^2}{24h} & \frac{-5H^2}{24h} & \frac{H}{2} + \frac{H^2}{24h} & \frac{H}{4} + \frac{5H^2}{24h} \end{bmatrix} \quad (7)$$

$[K^{u\phi}]$ for the series connection of the piezoelectric layers is presented in “Eq. (8)”.

$$[K^{u\phi}] = \frac{ebH^2}{3h} \begin{bmatrix} 0 & 0 & 0 & 0 \\ 1 & -1 & -1 & 1 \\ 0 & 0 & 0 & 0 \\ -1 & 1 & 1 & -1 \end{bmatrix} \tag{8}$$

$$[K^{\phi\phi}] = -\int_V [B^\phi]^T [\epsilon^s] [B^\phi] dV = 2 \frac{\epsilon}{H} \begin{bmatrix} \frac{2H}{3h} + \frac{7h}{12H} & \frac{2H}{3h} + \frac{h}{12H} & -\frac{2H}{3h} - \frac{5h}{12H} & \frac{5H}{12h} + \frac{5h}{12H} \\ \frac{2H}{3h} + \frac{h}{12H} & \frac{2H}{3h} + \frac{h}{6H} & -\frac{2H}{3h} - \frac{h}{12H} & -\frac{H}{12h} - \frac{h}{12H} \\ -\frac{2H}{3h} - \frac{5h}{12H} & -\frac{2H}{3h} - \frac{h}{12H} & \frac{2H}{3h} + \frac{h}{6H} & \frac{H}{3h} + \frac{h}{6H} \\ \frac{5H}{12h} + \frac{5h}{12H} & -\frac{H}{12h} - \frac{h}{12H} & \frac{H}{3h} + \frac{h}{6H} & \frac{2H}{3h} + \frac{h}{6H} \end{bmatrix} \tag{9}$$

$$[M] = \int_V [N^u]^T \rho [N^u] dV \tag{10}$$

Where ϵ , is the permittivity factor.
 For the finite element formulation, the electric potential is specified on the external boundary for the Dirichlet BC problem. The finite element model has been developed with FORTRAN programming Language.

3 SUPPORT EFFECT ON THE PERFORMANCE OF PIEZOELECTRIC BEAM ACTUATOR

The developed finite element program has been named Piezoelectric Beam Analysis (PIBA). The piezoelectric beam has two layers.

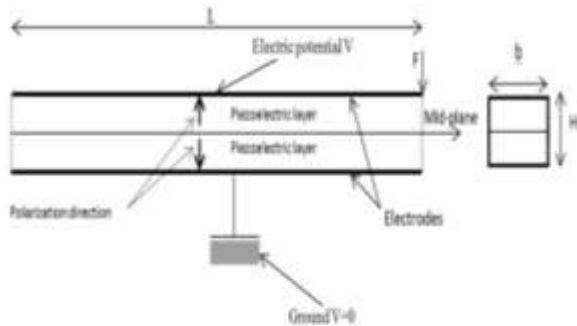


Fig. 2 Series connection of piezoelectric layers.

The parallel connection of the piezoelectric layers represents equal polarities (“Fig. 3”). In this study, the conditions of both series and parallel connections are used in the model.

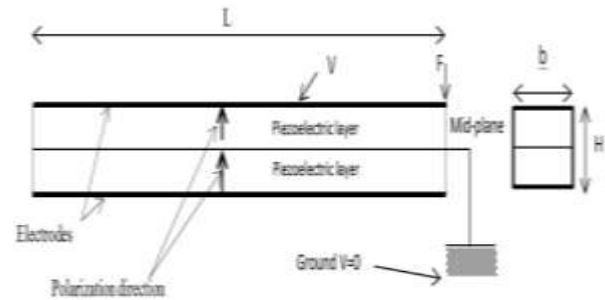


Fig. 3 Parallel connection of piezoelectric layers.

The series connection of the piezoelectric layers represents opposite polarities (“Fig. 2”). The beam presented has $L=100\text{mm}$, $H=0.5\text{mm}$, $b=1\text{mm}$ and is loaded by $V=100\text{V}$ in the actuator. The piezoelectric layer is taken to be PZT-5H [18]. The properties of the piezoelectric material are shown in “Table 1”.

Table 1 The properties of the piezoelectric material

piezoelectric stress matrix \bar{e} [C/m ²]	dielectric permittivity matrix ϵ [F/m]	elasticity constant E[GPa]	Poisson ratio ν [-]	Mass density ρ [kg/m ³]
$\begin{bmatrix} 0 & 0 & 0 \\ 4.4 \cdot 10^{-1} & 4.4 \cdot 10^{-1} & 0 \end{bmatrix}$	$\begin{bmatrix} 0 & 0 & 0 \\ 0 & 0 & 0 \\ 0 & 0 & 106.248 \cdot 10^{-12} \end{bmatrix}$	200	0.3	7760

Figure 4 shows the deflection of the beam Using voltage $V=100V$ (Voltage Driven Electrodes) for the Piezoelectric Beam clamped at one end. The Figure presents that the displacement of the piezoelectric beam has a linear behavior on the length of beam.

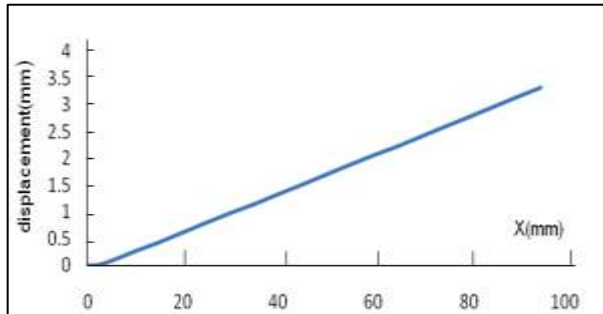


Fig. 4 Deflection of a Piezoelectric Beam Clamped at One End.

The deflection numerical results of the free end of the beam are compared to the analytical method and Ansys software results in “Table 2”. The results show PIBA results have proper adjustment with Analytical results, also the deflection of beam in the parallel case is twice the deflection of beam in the series case.

Table 2 Deflection of the free end of the beam

	PIBA result[m]	Analytical result[m]	ANSYS result[m]
Series case	0.001755	0.00176	0.00132
Parallel case	0.00351	0.00352	0.00264

Figure 5 shows the deflection of the beam using voltage $V=100V$ (Voltage Driven Electrodes) for the Piezoelectric Beam clamped at two ends. The result shows that the deflection of a piezoelectric beam clamped at two ends has harmonic behavior. The deflection direction of the beam changes in the middle of the beam. So, the middle of the beam deflection is zero. This result is important for the behavior of the actuator.

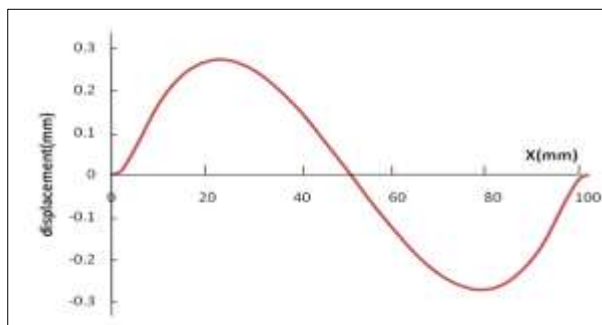


Fig. 5 Deflection of a piezoelectric beam clamped at two ends.

Figure 6 shows the deflection of the beam using voltage $V=100V$ (Voltage Driven Electrodes) for the Piezoelectric Beam clamped at one end and pivoted at the other end. The result shows that the Deflection of piezoelectric beam clamped at one end and pivoted at the other end has harmonic behavior with semi-cycle. The maximum deflection is in $x=40mm$ from Clamped support.

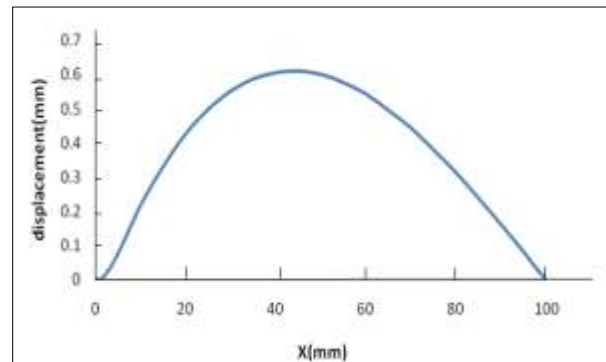


Fig. 6 Deflection of piezoelectric beam clamped at one end and pivoted at the other end.

Figure 7 shows the deflection of the beam using voltage $V=100V$ (Voltage Driven Electrodes) for the Piezoelectric Beam clamped at one end and with vertical translation at the other end. The figure shows that the displacement of the piezoelectric beam has parabolic behavior on the length of the beam.

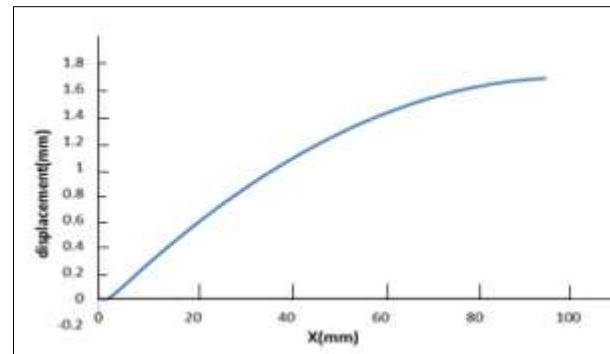


Fig. 7 Deflection of piezoelectric beam clamped at one end and with vertical translation at the other end.

4 EFFECTS OF CONCENTRATED MASS ON THE ANALYSIS OF PIEZOELECTRIC BEAM FREQUENCY

The stiffness matrix of the piezoelectric model depends on the electrical boundary conditions. The piezoelectric coupling parameter can affect Eigen frequencies. The concentrated mass and piezoelectric coupling influence the result. The structure presented in “Fig. 8” has been used for modal analysis. The results of electromechanical coupling and uncoupling and the

concentrated mass effect ($m=0.1\text{gr}$) are presented in “Table 3”. The results of the PIBA program are compared to the results of Ansys software. The piezoelectric beam element is not available in Ansys.

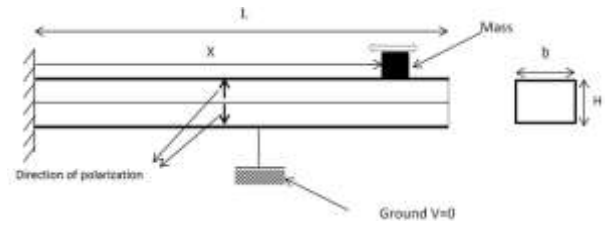


Fig. 8 Piezoelectric model and concentrated mass.

Table 3 The results of electromechanical coupling, uncoupling, and concentrated mass effect ($m=0.1\text{[gr]}$)

Structure model	Mode 1[Hz]		Mode 2[Hz]		Mode3[Hz]		Mode4[Hz]	
	PIBA	Ansys	PIBA	Ansys	PIBA	Ansys	PIBA	Ansys
Beam without coupling and mass	69.3	69.91	437	440	1226	1246	2403	2483
Beam with coupling and without mass	60.5		375		1030		1429	
Beam without coupling and with mass ($X=100\text{mm}$)	34.4	34.67	327.5	329.3	1017	1032.6	2097	2163
Beam with coupling and mass ($X=100\text{mm}$)	30.5		287.2		831		1384	
Beam without coupling and with mass ($X=70\text{mm}$)	48.4	48.8	406.3	408.5	977.6	989.07	2264	2337
Beam with coupling and mass ($X=70\text{mm}$)	41.2		343.3		900.7		1186	
Beam without coupling and with mass ($X=50\text{mm}$)	59.5	60.05	298.8	300.3	1226	1245.7	1926	1976
Beam with coupling and mass ($X=50\text{mm}$)	51.7		279.7		869.3		1163	
Beam without coupling and with mass ($X=20\text{mm}$)	68.9	69.49	380.2	382.9	856.7	868.9	1882	1932
Beam with coupling and mass ($X=20\text{mm}$)	60.0		327.4		792.3		1331	

The effect of concentrated mass position on Eigen frequencies is shown in “Figs. 9-12” (mode 1- 4). Numerical results showed that the frequency of a piezoelectric beam is lower than that of an uncoupling beam. The reason for this problem is the coupling matrix of piezoelectric in the stiffness matrix of the beam.

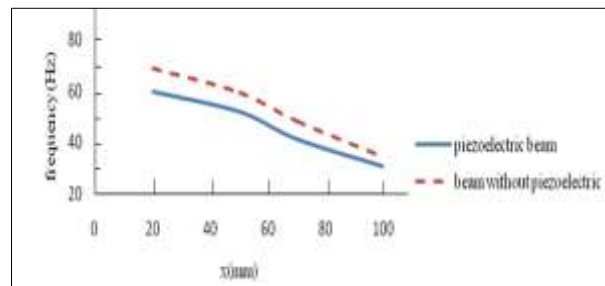


Fig. 9 The effect of position of concentrated mass on the first Eigen frequency.

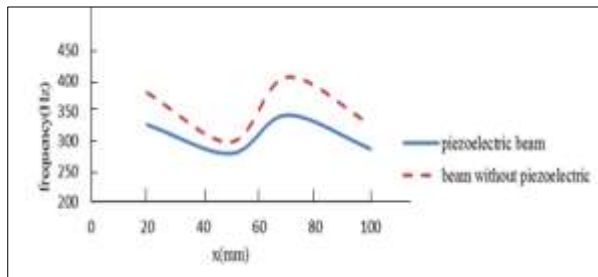


Fig. 10 The effect of position of concentrated mass on the second Eigen frequency.

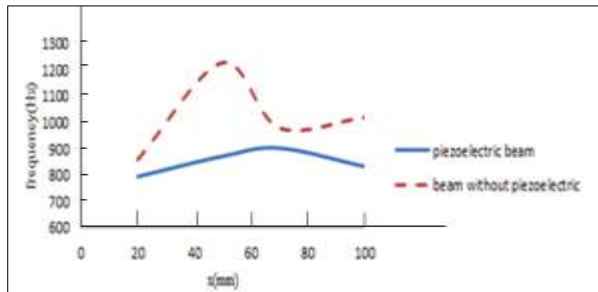


Fig. 8 The effect of position of concentrated mass on the third Eigen frequency.

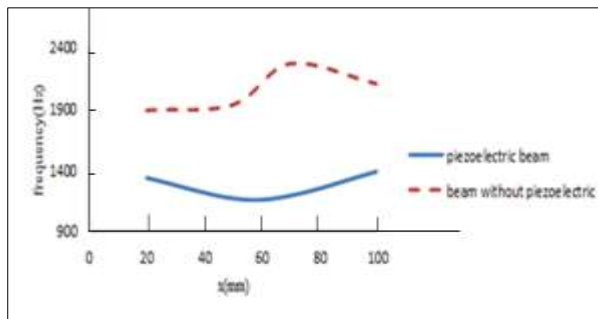


Fig. 8 The effect of position of concentrated mass on the fourth Eigen frequency.

As a second analysis, the position of the concentrated mass was set to vary. Frequency analysis was extended to examine concentrated mass. The results showed a change in Eigen frequency with the position of mass. Comparisons of the coupling and uncoupling beams indicate that the first and second Eigen frequencies change similarly for both models, but changes in the third and fourth Eigen frequencies are discordant for the two models. The reason for this problem is the positive and negative elements in the piezoelectric matrix.

5 CONCLUSIONS

A finite element program for analyzing the behavior of piezoelectric structures has been presented in this article. The beam element is based on the Euler-Bernoulli theory. The electrical boundary conditions of a closed

circuit were considered in a static solution, and electric potentials were applied on the upper and lower beam faces. The model was loaded with electrical and mechanical forces and the results were compared to the analytical method and ANSYS software. The discrepancy was negligent.

The present work was used to study a piezoelectric beam under a variety of boundary conditions. The effects of support on the deflection of the piezoelectric beam would be considerable for actuator structures.

Modal analysis of the beam was also presented. This analysis was carried out for a coupling and uncoupling beam. Numerical results showed that the frequency of a piezoelectric beam is lower than that of an uncoupling beam.

As a second analysis, the position of the concentrated mass was set to vary. Frequency analysis was extended to examine concentrated mass. The results showed a change in Eigen frequency with the position of mass. Comparisons of the coupling and uncoupling beams indicate that the first and second Eigen frequencies change similarly for both models, but changes in the third and fourth Eigen frequencies are discordant for the two models. The reason for this problem is the positive and negative elements in the piezoelectric matrix.

REFERENCES

- [1] Allik, H., Hughes, T. J. R., Finite Element Method for Piezoelectric Vibration, International Journal for Numerical Methods in Engineering, Vol. 2, 1970, pp. 151-157.
- [2] Zemcik, R., Roifes, R., Rose, M., and Tessmer, J., High Performance Four-node Shell Element with Piezoelectric Coupling for the Analysis of Smart Laminated Structures, Int. J. Numer. Meth. Engng, Vol. 70, 2007, pp. 961-934.
- [3] Lazarus, A., Thomas, O., Deu, J. F., Finite Element Reduced Order Models for Nonlinear Vibration of Piezoelectric Layered Beams with Applications to NEMS, Finite Elements in Analysis and Design, Vol. 49, 2012, pp. 51-35.
- [4] Kogel, M., Bucalem, M. L., Analysis of Smart Laminates using Piezoelectric MITC Plate and Shell Elements, Computers and Structures, Vol. 83, 2005, pp. 1163-1153.
- [5] Piefort, V., Preumont, A., Finite Element Modeling of Smart Piezoelectric Shell Structures, 5th National Congress on Theoretical and Applied Mechanics, 2000.
- [6] Sebald, G., Kuwano, H., and Guyomar, D., Experimental Duffing Oscillator for Broadband Piezoelectric Energy Harvesting, Smart Materials and Structures, Vol. 20, 2011, pp. 1-10.
- [7] Erturk, A., Inman, D. J., Broadband Piezoelectric Power Generation on High-energy Orbits of the Bistable Duffing Oscillator with Electromechanical Coupling,

- Journal of Sound and Vibration, Vol. 330, 2011, pp. 2339–2353.
- [8] Friswell, M. I., Faruque, S. A., Bilgen, O., Adhikari, S., Lees, A. W., and Litak, G., Non-linear Piezoelectric Vibration Energy Harvesting from a Vertical Cantilever Beam with Tip Mass, *Journal of Intelligent Material Systems and Structures*, Vol. 23, No. 13, 2012, pp. 1505–1521.
- [9] Bendigeri, C., Tomar, R., Basavaraju, S., and Arasukumar, K., Detailed Formulation and Programming Method for Piezoelectric Finite Element, *Int. J. Pure Appl. Sci. Technol*, Vol. 7, No. 1, 2011, pp. 1-21.
- [10] Jabbari, M., Ghayour, M., The Effect of Support and Concentrated Mass on the Performance of Piezoelectric Beam Actuator and Frequencies, ISAV, 2013.
- [11] Jabbari, M., Ghayour, M., The Numerical Solution of Dynamic Behavior of Nonlinear Piezoelectric Beam, Aero 2014, Tehran University, 2013.
- [12] Jabbari, M., Ghayour, M., and Mirdamadi, H. R., Energy Harvesting of a Multilayer Piezoelectric Beam in Resonance and Off-resonance Cases, *Journal of Engineering Materials and Technology*, Vol. 139, 2017, pp. 031008-1.
- [13] Jabbari M, Ghayour M, Mirdamadi H.R., Experimental and Numerical Results of Dynamics Behavior of a Nonlinear Piezoelectric Beam, *Mechanics of Advanced Materials and Structures*, Vol 23, No 8, 2016, 853-864.
- [14] Jabbari, M., The Effect of Strain Nodes on the Energy Harvesting of the Cantilever Piezoelectric Beam with the Vibration Mode Excitation, *Modares Mechanical Engineering*, Vol. 17, No. 10, 2018, pp. 65-72.
- [15] Jabbari, M., Ahmadi, B., The Electric Response of Piezoelectric Beam Using Dynamic Stiffness Method, *Applied and Computational Sciences in Mechanics*, Vol, 31, No, 2, 2020.
- [16] Hassannejad, R., Hosseini, S. R., and Alizadeh Hamidi, B., Influence of Non-circular Cross Section Shapes on Torsional Vibration of a Micro-rod Based on Modified Couple Stress Theory, *Acta Astronautica*, Vol. 178, No. 2, 2021, pp. 805-812.
- [17] Shamel, R., Aghadavoudi, F., and Hashemian, M., Free Torsional Vibration Analysis of Nanorods with Non-circular Cross-Sections Based on the Second-Order Strain Gradient Theory. *J. Vib. Eng. Technol.*, Vol. 11, 2023, pp. 3039–3055.

Jump Phenomenon Analysis in Vehicle and Chaos Control of Active Suspension System via Extended Pyragas Algorithm

Yavar Nourollahi Golouje, Mahdi Abtahi *

Department of Mechanical Engineering, Faculty of Industrial and Mechanical Engineering, Qazvin Branch, Islamic Azad University, Qazvin, Iran

E-mail: y.noorallahi@advaco.ir, m.abtahi61@gmail.com

*Corresponding author

Received: 9 August 2022, Revised: 22 January 2023, Accepted: 12 February 2023

Abstract: In this paper, the nonlinear phenomenon including hump and chaos analysis along with chaos control of an active suspension in vehicles has been studied. The unstable periodic orbits of the system are stabilized using the novel developed delay feedback control algorithm based on the fuzzy sliding mode system. The chaotic Equations of motions are derived via Newton-Euler relations then, the nonlinear phenomenon such as jump and chaos in the vehicle dynamics has been confirmed using forcing frequency method. The results of the forcing frequency demonstrate the changes in system behaviour from the periodic to the irregular chaotic responses. In order to eliminate the chaotic responses in the vertical dynamics of the vehicle, a new fuzzy sliding delay feedback control algorithm is designed on the active suspension. The controller gain of the sliding feedback control is online estimated via fuzzy logic causing to rejection of the chattering phenomenon in the sliding mode algorithm besides the improvement in the responses of the feedback system. Simulation results of the control system depict a reduction of settling time and energy consumption along with eliminating the overshoots and chaotic vibrations.

Keywords: Chaotic Dynamics, Chaos Control, Extended Pyragas, Jump Phenomenon

Biographical notes: **Yavar Nourollahi** received his BSc and MSc in Mechanical Engineering at the Islamic Azad University of Tabriz, where he is now studying PhD in Mechanical Engineering, Applied Solid Design at the Islamic Azad University of Qazvin, Iran since 2016. His research interest includes nonlinear dynamics and control of specialized chaotic systems. **Mahdi Abtahi** received his PhD in Mechanical Engineering from K. N. Toosi University of Technology in 2013. He is currently an Assistant Professor at the Department of Mechanical Engineering, Islamic Azad University branch of Qazvin in Iran. His current research interest includes dynamic and control system, nonlinear mechanics, and Chaos.

Research paper

COPYRIGHTS

© 2024 by the authors. Licensee Islamic Azad University Isfahan Branch. This article is an open access article distributed under the terms and conditions of the Creative Commons Attribution 4.0 International (CC BY 4.0)

<https://creativecommons.org/licenses/by/4.0/>



1 INTRODUCTION

Nonlinear phenomena including jump, quasi-periodic, and chaos can occur in the heave motion of vehicles. Therefore, some oscillations in the suspension system are returned to this nonlinear phenomenon. Most algorithms in chaos control are designed on the basis of stabilization of unstable orbits that require a complex solution of unstable orbits. Pyragas controller based on the delay feedback control can control the chaotic system without solving the complex orbits [1-4].

Many papers have been recently published about the chaotic dynamics and chaos control of suspension systems. The chaotic dynamics and control of vehicles under the unevenness of the road surface are investigated using numerical and analytical procedures [5-7]. The effect of damping coefficients and the passengers on the chaotic dynamic behavior are considered via the bifurcation diagrams in the vertical model of vehicles under the excitation force of the road surface [8-11]. Pyragas method based on delay feedback control has been used in chaotic systems because of the simple structure and good performance [12]. Zhang et al controlled the chaotic lateral dynamic in an active steering system using the adaptive time delay feedback method which led to the reduction of bounce vibrations [13-15].

In this research, the jump and chaotic responses in heave motion are studied and controlled using the delay feedback control algorithm developed by the fuzzy sliding mode system. The nonlinear jump phenomenon and chaos are analyzed via the forcing frequency diagrams. In order to stabilize the chaotic dynamical system, the Pyragas method is integrated with a new sliding mode algorithm which fuzzy inference system extends the sliding delay feedback. In this novel controller, by online calculation of the controller's coefficient in the developed Pyragas control system based on the sliding mode, the appropriate value of the control gain was estimated via the fuzzy system that the chattering phenomenon caused by the sliding mode behaviour around the sliding surface can be eliminated. The simulation results of the feedback system demonstrate the control of the suspension system without chaos.

2 MATHEMATICAL MODELING

The model of vertical motion is shown in "Fig. 1" that the body has two state variables consisting of the vertical displacement x_b and rotation θ . The rotation around the longitudinal axis of the body and the rotation perpendicular to the passageway can be eliminated due to their small effects. The tire model with nonlinear damping and springs is modeled as unsprung masses.

The front and rear actuators' forces are u_f and u_r in the active suspension system.

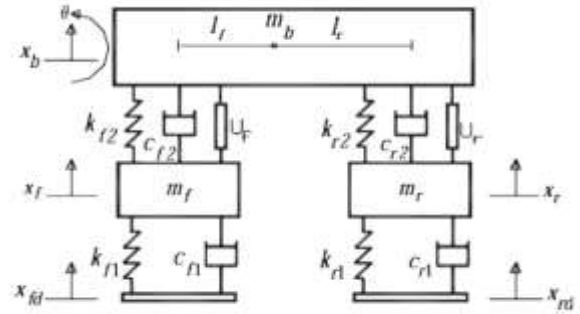


Fig. 1 Vertical model with active suspension.

Nonlinear spring and damper suspension relations are as follows [16]:

$$F_s = K_1 X + K_2 X^3 = K_1(x_b - x_0) + K_2(x_b - x_0)^3$$

$$F_{sc} = C_1 V + C_2 V^3 = C_1 \frac{d}{dt}(x_b - x_0) + C_2 \left(\frac{d}{dt}(x_b - x_0)\right)^3 \quad (1)$$

Where, k and c are the stiffness and dampers coefficient, X_0 is the displacement of the input excitation from the road surface that is expressed by $X_{fd} = A \sin(2\pi ft)$ and $X_{rd} = A \sin(2\pi ft + \alpha)$ for the front and rear tires, where A is the amplitude, f is the frequency of the excitation force and α represents the time delay between the displacement applied by the road surface affecting the front and rear tires. Also, vehicle tires are modeled with nonlinear spring and viscous damper, and the mathematical relationship for tire spring force equals $f_s = k_s \zeta_s$ and $f_{tc} = c_t \zeta_t \dot{x}_t$ as tire damper force. By applying the Newton-Euler laws, the vehicle motion Equations are as follows:

$$m_b \ddot{x}_b = -k_{f2}(\zeta_{bf2}) - c_{f2}(\dot{\zeta}_{bf2}) - k_{r2}(\zeta_{br2}) - c_{r2}(\dot{\zeta}_{br2}) - m_b g + u_f + u_r \quad (2)$$

$$j\ddot{\theta} = (k_{f2}(\zeta_{bf2}) + c_{f2}(\dot{\zeta}_{bf2}))(l_f \cos \theta) - (k_{r2}(\zeta_{br2}) + c_{r2}(\dot{\zeta}_{br2}))(l_r \cos \theta) \quad (3)$$

$$m_f \ddot{x}_f = k_{f2}(\zeta_{bf2}) + c_{f2}(\dot{\zeta}_{bf2}) - k_{f1}(\zeta_{bf1}) - c_{f1}(\dot{\zeta}_{bf1}) - m_f g + u_f \quad (4)$$

$$m_r \ddot{x}_r = k_{r2}(\zeta_{br2}) + c_{r2}(\dot{\zeta}_{br2}) - k_{r1}(\zeta_{br1}) - c_{r1}(\dot{\zeta}_{br1}) - m_r g + u_r \quad (5)$$

Where $\zeta_{bf1} = x_f - \zeta_{sf1} - x_{fd}$,

$\zeta_{bf2} = x_b - \zeta_{sf2} - x_f - l_f \sin \theta$, and that ζ_{sf} are the static

length variations of the suspension springs in tires. The simulation parameters' numerical values are shown in "Table 1".

Table 1 Values of parameters in the numerical solutions

System parameters	Value
M_b	1180 kg
J	633.6 kg m ²
M_f	50 kg
M_r	45 kg
K_{f2}	36952 N/m
K_{r2}	30130 N/m
K_{f1}, K_{r1}	140000 N/m
C_{f2}	500 kg/s
C_{r2}	360kg/s
C_{f1}, C_{r1}	10kg/s
l_f	1.123 m
l_r	1.377 m

3 JUMP ANALYSIS

After simulation of the system based on the values of parameters in "Table 1" and the input excitation of the road surface as $A=0.08m$ and phase $\alpha=\pi/9$ rad, the responses show the occurrence of chaos in the system, which the forcing frequency diagrams is used to prove the nonlinear vibrations. The natural frequencies of the system are calculated as $f_{n1}=1.0750Hz$, $f_{n2}=1.8234Hz$, $f_{n3}=9.4976Hz$, and $f_{n4}=9.8139Hz$ that $f=10823Hz$ is the dominant frequency of the system. In order to verify the values of the natural frequencies, the results obtained in this research were compared with the results of reference [10] in "Table 2", the results of the comparisons showed that the natural frequencies obtained in this research are in the same range as the reference that clearly indicated the correctness of the calculations.

Table 2 Comparison of the results of natural frequencies obtained with reference [10]

Comparison	f_{n1}	f_{n2}	f_{n3}	f_{n4}
Natural Frequency	1.0750 Hz	1.823 Hz	9.4976 Hz	9.8139 Hz
Natural Frequency in Ref [10]	1.28 Hz	1.80 Hz	9.08 Hz	9.26 Hz

The values of the vehicle speed, taking into account the reference [6] and the values of the first and second natural frequency and the jump frequency [$f=1.075, 1.8234, 3.6$] Hz are equal to [$v=13.93, 23.63, 46.66$] km/h.

The dynamic analysis of the frequency control parameter of the road surface excitation force is shown in the graphs of "Fig. 2", which includes the maximum

absolute value of the displacement of the state variables according to the frequency control parameter of the road surface excitation force, which indicates different behaviors in the responses of the system with increasing and decreasing frequency of the driving force. The range of increasing and decreasing frequency, for example, in the frequency range $1Hz < f < 6Hz$ and in parts of the frequency range $3Hz < f < 5Hz$, we see the behavior of frequency jumping.

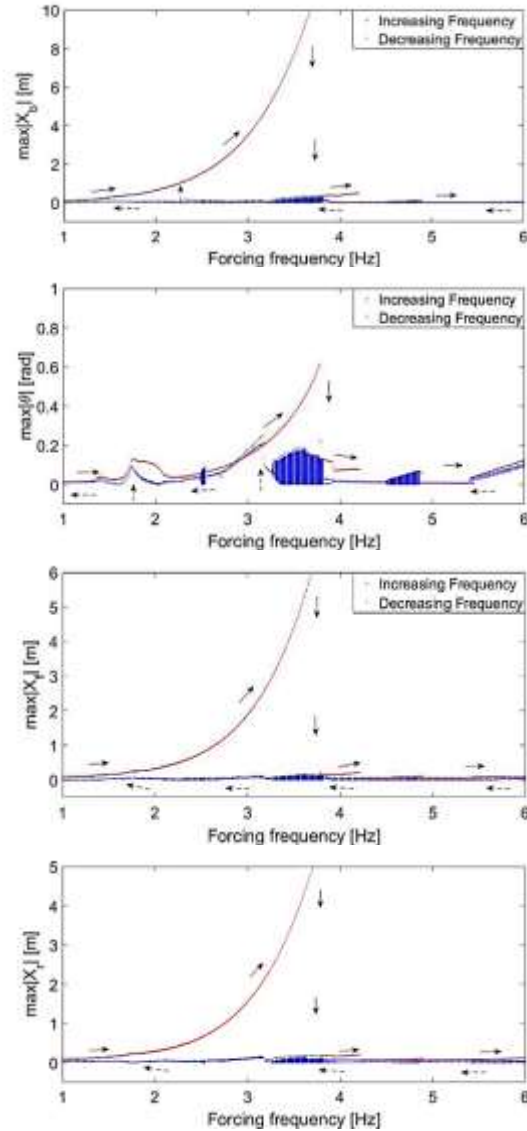


Fig. 2 Frequency response of system.

4 CHAOS CONTROL

Sliding-Pyragas controllers based on the delay feedback control are used to stabilize the unstable orbits which is estimated by a time-delay state variable. The feedback is the difference between the state and its time delay τ , and

the delay time constant is estimated as the periodic of orbits. The main advantage of this method is no need to calculate the orbits. Therefore, the control input signal is derived as $u(t)=k[y(t-\tau)-y(t)]$ that k is control gain [3]. The Pyragas algorithm is a linear feedback to stabilize unstable orbits. If the dynamic system is defined as:

$$\dot{x}^{(n)} = f(t, \underline{x}) + g(t, \underline{x})u \quad (6)$$

Where, x is the state vector, u is the control input signal, f and g are uncertain functions, and in $u=0$, the system has chaotic behavior [17]. For this reason, at first, the delay state is defined. It is $\tilde{x}(t) = \underline{x}(t-T)$. It is obvious that the delay state should meet the following:

$$\dot{\tilde{x}}^{(n)} = f(t-T, \tilde{x}) + g(t-T, \tilde{x})\tilde{u} \quad (7)$$

Where, $\tilde{u} = u(t-T)$. The dynamics of the error system is obtained by distinguishing between two Equations (6) and (7) as follows:

$$\dot{x}^{(n)} - \dot{\tilde{x}}^{(n)} = f(t, \underline{x}) - f(t-T, \tilde{x}) + g(t, \underline{x})u - g(t-T, \tilde{x})\tilde{u} \quad (8)$$

Where, $\underline{e} = \underline{x} - \tilde{x}$ the error and the differential Equation of the error system are expressed as follows:

$$\dot{\underline{e}}^{(n)} = f(t, \underline{e} + \tilde{x}) - f(t-T, \tilde{x}) + g(t, \underline{e} + \tilde{x})u - g(t-T, \tilde{x})\tilde{u} \quad (9)$$

Therefore, the stability of orbits in a chaotic system according to Equation (8) leads to the stabilization of the error dynamics (9) that in order to increase the speed of convergence of the system to its stable fixed points, due to the uncertainties of the system, the robust control strategy based on the sliding mode has been used with definition of the sliding surface as follows [17]:

$$S = \sum_{i=1}^{n+1} \alpha_i \left[\int_T^t e_i(s) ds = \int_T^t e^{(i-1)}(s) ds \right] \quad (10)$$

Where $\alpha_i > 0$ and for stability of sliding mode, the system must be placed in $S=0$ that is defined $V = (1/2)S^2$ as the Lyapunov function. Assuming $g(t, \underline{x}) > 0$ and simplifying the calculations, the control input u is extracted as follows [17]:

$$u = -\frac{1}{\alpha_n g_m(t, \underline{x})} [\alpha_n \hat{f}(t, \underline{x}) - \alpha_n \hat{f}(t-T, \tilde{x}) + \sum_{i=1}^n \alpha_i e_i + K \text{sign}(S)] \quad (11)$$

Where, k in order to satisfy the Lyapunov stability condition of the system must be applied to the following inequality.

$$K \geq \left(\frac{g_M(t, \underline{x})}{g_m(t, \underline{x})} - 1 \right) \left| \sum_{i=1}^n \alpha_i e_i + \alpha_n f(t, \underline{x}) - \alpha_n f(t-T, \tilde{x}) + \alpha_n F(t, \underline{x}) + \alpha_n F(t-T, \tilde{x}) + g_M(t-T, \tilde{x})|\tilde{u}| + \theta \right| \quad (12)$$

5 SIMULATION OF CONTROL SYSTEM

The behaviour of the feedback system under the fuzzy-sliding Pyragas controller is simulated according to ‘‘Fig. 3’’.

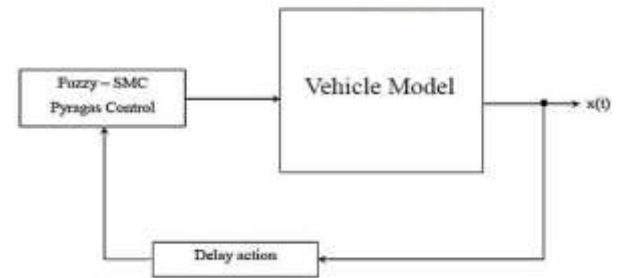
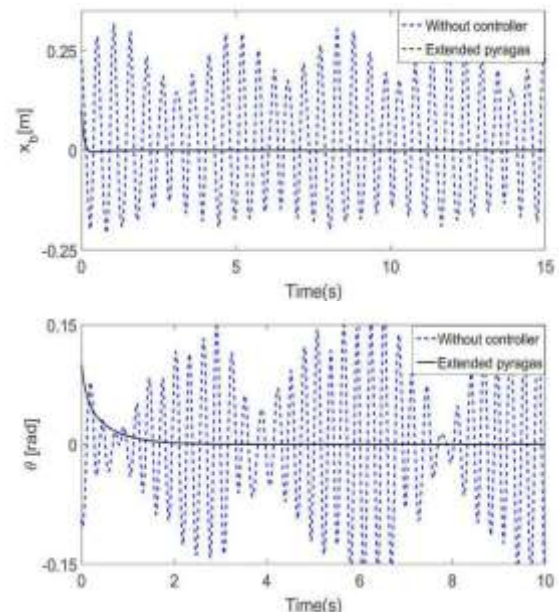


Fig. 3 Block diagram of the Control system.

Responses of the feedback system along with the chaotic open loop of state variables in active suspension are demonstrated in ‘‘Fig. 4’’ that stat the rejection of chaos in the feedback responses.



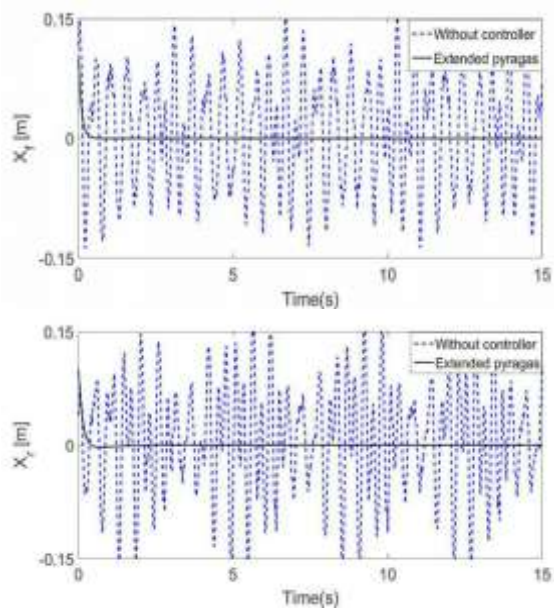


Fig. 4 Responses of the feedback control system.

The responses of the actuators in the active suspension under the Extended Pyragas controller are shown in “Fig. 5” below.

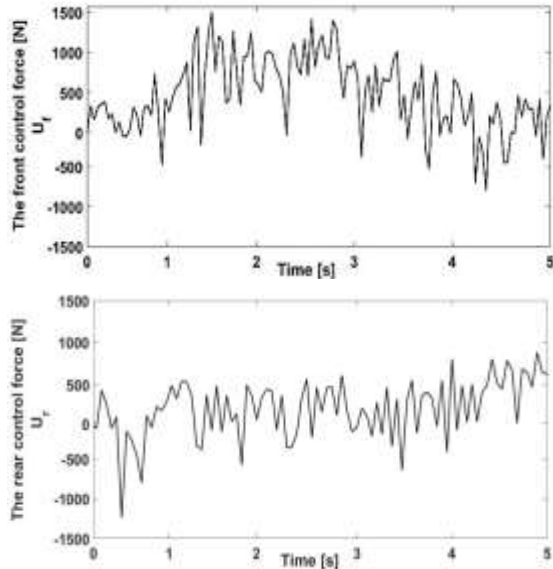


Fig. 5 The front and rear actuators of active suspension. Power consumption of active suspension is determined as the following [18]:

$$P_{ac} = \frac{\int_0^T [U(t) \cdot (S\dot{W}S)(t)] dt}{T} \quad (13)$$

Where, U is the control force and $S\dot{W}S$ is the suspension deflection of the actuator. Figure 6 shows the average

power consumption of the Extended Pyragas controller for the front and rear suspension systems which is equal to 1.2117kW and 0.4114kW.

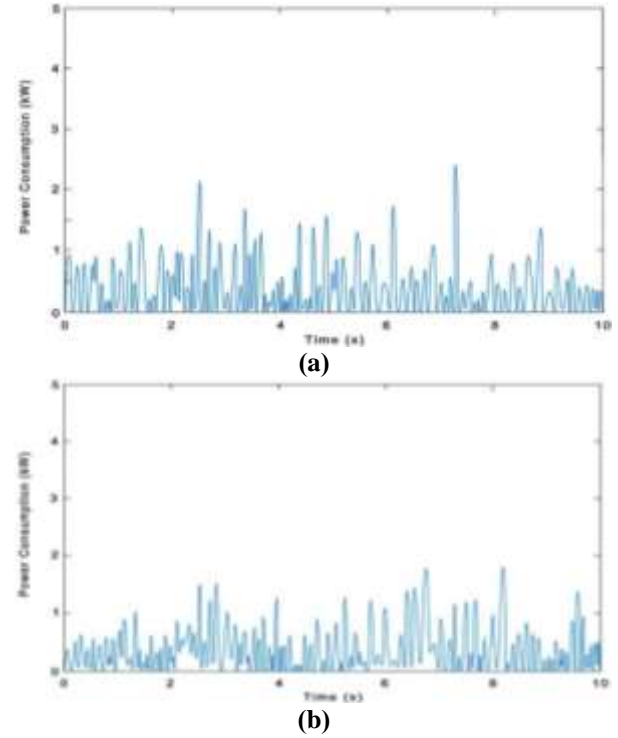


Fig. 5 Power consumption of the controller system: (a): front suspension, and (b): rear suspension.

For stability analysis of the feedback system, after linearization of the system around the fixed point, all of the eigenvalues are placed in the left hand of the complex plane, which depicts the stability of system.

For robustness analysis of the controller against the parametric uncertainties, the inertia of the system model is increased as 8% of simulated values and the new simulation results show the appropriate performance of the feedback controller. Also, in order to analyze the structural robustness of the controller, the control system is applied to the Carsim model as a SUV vehicle with 27 degrees of freedom based on “Fig. 3” that results of this simulation shows the entirely adaptation of responses.

6 CONCLUSIONS

The nonlinear vibrations of the bounce model of vehicle in the face of uneven road surface are investigated in this work and then the irregular oscillations are rejected via a new sliding delay feedback fuzzy controller. Therefore, after simulation of the open loop system, forcing frequency diagrams are used to analyze the jump phenomenon and chaos in the nonlinear dynamics, quasi-periodic and chaotic behavior are demonstrated in

the uncontrolled system relative to changing frequency. In order to control chaos, the delay feedback strategy is developed in the active suspension system. To increase the system's rapid stabilization, a sliding mode control is used in the structure of the Pyragas controller. Also, to eliminate the chattering phenomenon in the sliding mode and to online estimate the controller gain accurately, the fuzzy inference system is combined with the sliding delay feedback system. The simulation results of the Fuzzy SMC-Pyragas controller indicate the rapid stabilization along with the elimination of chaos by reducing the settling time without any overshoot in the responses. Comparison of results in this research with respect to [19] depicts a 15% reduction at the settling time besides rejection of the overshoot. Also in control signals responses, in addition to a 26% reduction in actuators effort and 34% decrease in the energy consumption, the saturation problems in suspension actuators are solved. Consequently, these results are compared with [20] which depicts a 20% reduction in the settling time by the overshoot rejection, a 35% reduction in the amplitude of the controller input in suspension actuators, and 20% decrease in energy consumption is illustrated in the control signal.

7 NOMENCLATURES

α	:the time delay between the road roughness to the front and rear tire
m_b	:vehicle body mass:
J	:vehicle body inertia
m_f	:front unsprung mass
m_r	:rear unsprung mass
$x_b(t)$:displacement of m_b
$\theta(t)$:angular displacement of m_b
$x_f(t)$:displacement of m_f
$x_r(t)$:displacement of m_r
$x_{fd}(t)$:excitation to the front tire
$x_{rd}(t)$:excitation to the rear tire
l_f	:front length
l_r	:rear length
k_{f2}	:front suspension spring stiffness
c_{f2}	:front suspension damping coefficient
k_{r2}	:rear suspension spring stiffness
c_{r2}	:rear suspension damping coefficient
k_{f1}	:front tire stiffness
c_{f1}	:front tire damping coefficient
k_{r1}	:rear tire stiffness
c_{r1}	:rear tire damping coefficient
k_s	:stiffness of the suspension springs
A	:amplitude of the excitation force
f	:frequency of the excitation force

REFERENCES

- [1] Ott, E., Grebogi, C., and Yorke, J. A., Controlling Chaos, Phys Rev Lett, Vol. 64, 1990, pp. 1196–1199.
- [2] Pyragas, K., Continuous Control of Chaos by Self-Controlling Feedback, Physics Letters A, Vol. 170, 1992, pp. 421-428.
- [3] Pyragas, K., Tamas, A., Experimental Control of Chaos by Delayed Self-Controlling Feedback, Phys. Lett. A, Vol. 180, 1993, pp. 99–102.
- [4] Abtahi, M., Chaotic Study and Chaos Control in A Half-Vehicle Model with Semi-Active Suspension Using Discrete Optimal Ott–Grebogi–Yorke Method, J Multi-Body Dynamics, Vol. 231, 2017, pp. 148–155.
- [5] Litak, G., Borowiec, M., Friswell, M., and Szabelski, K., Chaotic Vibration of a Quarter-Car Model Excited by The Road Surface Profile, Communications in Nonlinear Science and Numerical, Vol. 13, 2018, pp. 1373–1383.
- [6] Litak, G., Borowiec, M., Friswell, M., and Przystupa, W., Chaotic Response of Quarter Car Model Forced by A Road Profile with A Stochastic Component, Chaos, Solutions and Fractals, Vol. 39, 2009, pp. 2448–2456.
- [7] Naik, R., Singru, P., Resonance, Stability and Chaotic Vibration of a Quarter Car Vehicle Model with Time-Delay Feedback, Common Nonlinear Sci Numer Simulat, Vol. 16, 2011, pp. 3397–3410.
- [8] Zhu, Q., Ishitobi, M., Chaotic Vibration of a Nonlinear Full-Vehicle Model, International Journal of Solids and Structures, Vol. 43, 2006, pp. 747-759.
- [9] Zhong, S., Chen, Y., Bifurcation of Piecewise-Linear Nonlinear Vibration System of Vehicle Suspension, Applied Mathematics and Mechanics, Vol. 30, 2009, pp. 677–684.
- [10] Fakheari, J., Khanlo, H., Ghayour, M., and Faramarzi, K., The Influence of Road Bumps Characteristics on The Chaotic Vibration of a Nonlinear Full-Vehicle Model with Driver, International Journal of Bifurcation and Chaos, Vol. 26, 2016, pp. 151-161.
- [11] Dehghani, R., Khanlo, H., and Fakhraei, J., Active Chaos Control of a Heavy Articulated Vehicle Equipped with Magnetorheological Damper, Nonlinear Dyn, Vol. 87, 2017, pp. 1923–1942.
- [12] Kucukefe, Y., Adnan, K., Delayed Feedback Control as Applied to Active Suspension of a Ground Vehicle, EUROCON 2009, IEEE.
- [13] Zhang, Z., Chau, K., and Wang, Z., Analysis and Stabilization of Chaos in the Electric-Vehicle Steering System, IEEE Transactions on Vehicular Technology, Vol. 62, 2013, pp. 1-10.
- [14] Koumen, G., Taffo, M., Siewe, S., and Tchawoua, C., Stability Switches and Bifurcation in A Two-Degrees-Of-Freedom Nonlinear Quarter-Car with Small Time-Delayed Feedback Control, Chaos, Solitons and Fractals, Vol. 87, 2016, pp. 226–239.
- [15] Abtahi, M., Melnikov-Based Analysis for Chaotic Dynamics of Spin-Orbit Motion of a Gyrostat Satellite,

- Journal of Multi-Body Dynamics, Vol. 233, 2019, pp. 931-941.
- [16] Chen, W., Zhang, R., Zhao, L., Wang, H., and Wei, Zh., Control of Chaos in Vehicle Lateral Motion Using the Sliding Mode Variable Structure Control, Proc IMechE Part D: J. Automobile Engineering, 2018, pp. 1–14.
- [17] Salarieh, H., Alasty, A., Chaos Control in Uncertain Dynamical Systems Using Nonlinear Delayed Feedback, Chaos, Solutions & Fractals, Vol. 41, 2009, pp. 67-71.
- [18] Metered, H., Musaad Ibrahim, I., Vibration Mitigation of Commercial vehicle Active Tandem Axle Suspension System, SAE Internatiol Journal, Vol. 18, 2022, pp. 02-15-03-0015.
- [19] Abtahi, M., Suppression of Chaotic Vibrations in Suspension System of Vehicle Dynamics Using Chattering-Free Optimal Sliding Mode Control, Journal of the Brazilian Society of Mechanical Sciences and Engineering, Vol. 41, 2019, pp. 209-219.
- [20] Golouje, Y. N., Abtahi, S. M., Chaotic Dynamics of The Vertical Model in Vehicles and Chaos Control of Active Suspension System Via the Fuzzy Fast Terminal Slidin Mode Control, Journal of Mechanical Science and Technology, Vol. 35. No. 1, 2021, pp. 31-43.

Tolerance Geometrical Interference Analysis of Specific Movement Mechanism Under Thermal Strain

Ali Lashkari Zadeh, Seyed Yousef Ahmadi Brooghani, Mojtaba Sheikhi Azqandi*

Department of Mechanical Engineering,
University of Birjand, Birjand, Iran

E-mail: alashkarimec@birjand.ac.ir, syahmadi@birjand.ac.ir,
mojtabasheikhi@birjand.ac.ir

*Corresponding author

Received: 11 September 2023, Revised: 7 April 2024, Accepted: 20 April 2024

Abstract: In sensitive mechanisms, achieving the required accuracy of the final parts at the most suitable price is a complex process. The tolerance design process is essential in design and manufacturing to achieve a quality and low-cost product. Allocation of appropriate tolerances is always time-consuming and challenging, especially for complex products, as it involves many aspects of design, manufacturing, and quality issues. In this research, a program has been written in MATLAB, in which by only one geometry model, all possible interferences of assembled parts for all tolerances and nominal sizes in different production modes have been investigated. By using this program, it is possible to add or reduce applied tolerances to nominal sizes and check the interference of parts for all tolerances. Also, temperature effects must be considered when designing a product that operates in a wide temperature range. This approach could ensure that the values of the output parameters of the mechanism remain stable with various temperature changes. The considered case study is particular clock whose structural parameter tolerances often significantly affect the accuracy of the timing output of the entire movement of the mechanism in the program; the tolerance of the parts of the delay clock mechanism has been studied. By analysing the tolerance of geometric non-interference and considering the strain of the parts due to the operating temperature of the mechanism, 24% of the examined sizes should be reduced to avoid interference and the tolerance of the axis position of the clock should be reduced to ± 0.01 .

Keywords: Geometric Interference Analysis, Mechanism, Operating Temperature Range, Operational Tolerance, Tolerance Analysis

Biographical notes: **Ali Lashkari zadeh** is a PhD student of Mechanical Engineering at the University of Birjand, Iran. His current research focuses on Tolerance analysis. **Seyed Yousef Ahmadi-Brooghani** is Professor of Mechanical engineering at the University of Birjand, Iran. He received his PhD in Mechanical engineering from University of Sheffield. His current research focuses on solid mechanics. **Mojtaba Sheikhi** received his PhD in Mechanical Engineering from University of Semnan in 2013. He is currently Associate Professor at the Department of Mechanical Engineering, University of Birjand, Iran. His current research interest includes optimal design of mechanical parts.

Research paper

COPYRIGHTS

© 2024 by the authors. Licensee Islamic Azad University Isfahan Branch. This article is an open access article distributed under the terms and conditions of the Creative Commons Attribution 4.0 International (CC BY 4.0)

<https://creativecommons.org/licenses/by/4.0/>



1 INTRODUCTION

There are various unknown factors, such as manufacturing errors, which modify the performance of a produced mechanism. Forces, acceleration, and temperature changes cause changes in dimensions and, hence, design tolerances. As a result, they adversely affect the performance of the product. The tolerance analyses of many products have indicated a failure to meet design requirements, signaling the inefficient performance of the system under different operational conditions.

Tolerance analysis methods include worst-case tolerance analysis and statistical methods [1]. Worst-case tolerance analysis considers the worst possible combination of part tolerances, which leads to highly strict tolerances and increases manufacturing costs. On the other hand, statistical tolerance analysis is a more practical and economical tolerance adjustment approach that ensures good efficiency. Some researchers have used this method to examine product tolerances. For instance, Dantan et al. [2] employed the worst-case method based on the Monte Carlo simulation for tolerance analysis. Tolerance analysis can be performed using highly accurate methods of sensitivity analysis [3-4]. Doltsinis and Kong [5] utilized optimization methods, including sensitivity analysis and participation analysis, to design structural parameters. Tolerance analysis was also used by Zang et al. [6], Huang and Zhong [7], Zhou Kai et al. [8] to achieve an optimal design and Shao et al presented a tolerance analysis approach to spur gears [9].

In mechanism design, the best tolerance combination must be applied to manufacture parts by considering multiple objective functions, such as the provision of suitable spaces for parts, conformance to operational requirements, improvement of product quality, and reduction of manufacturing costs [10-12]. Numerous models have so far been developed to represent geometric features, cumulative deviation, and tolerance interval estimation [13].

Conventional tolerance modeling methods are generally classified into tolerance map (T-map), small displacement torsor (SDT), homogeneous transformation matrix (HTM), and other heuristic methods.

T-maps consider vectors for surfaces of various components. However, they use only five standards: planes, cylinders, spheres, cones, and toruses [14-17]. In addition, modeling techniques such as neural networks [18], volumetric envelopes [19], modal analysis [20-21], and graph theory [22-23] have been used to model tolerances between parts and assemblies. Previous research indicates that skin model shapes are very useful for representing product geometry by considering geometric deviations and form errors [24-26]. For instance, finite element analysis has been introduced to help reduce modeling errors and enhance model quality

[27]. Researchers have demonstrated that discrete skin model shapes have a higher potential for assembly simulations, performance analysis, and tolerance analysis [28-30]. Regarding part contact and interference, Faraji and Abbasi [31] stated that the use of the average diameter for common form deviations cannot guarantee the acceptance or rejection of a part in geometric conformity quality control since the relationship between joint strength and average interference is not linear in these cases. This is due to the changes in the friction coefficient at the contact surface based on changes in the radius of curvature and the local contact pressure between the two surfaces. Hence, in the case of oval defects that reduce interference between the two parts below the nominal values, it is best to promptly address the factors causing these defects in the production line and remove defective parts from the production cycle. Researchers demonstrated that geometric parameters and tolerance analysis have a significant effect on the efficiency of mechanical systems [32-33].

In the analysis of mechanical assemblies, one must first perform an interference tolerance analysis before addressing dynamic requirements. Mechanical systems are in a static state before operation. Assimilability analyses of mechanical systems are performed under stationary conditions and fully depend on the tolerance ranges of parts. On the other hand, under static conditions, factors such as gear engagement or position sensor placement are of considerable importance at the beginning of motion or in other initial controls. Given the significance of dimensional and geometric tolerances in these cases, it is necessary to perform tolerance analyses of stationary mechanical systems in addition to examining the effects of external forces on them. For this purpose, the lack of part interference is defined as an objective function in the tolerance analysis of geometric interference.

In this research, a novel tolerance analysis method for mechanisms was presented in the form of a MATLAB program and was used to analyze a model created in SolidWorks. To implement this method, the program creates different tolerances in the three-dimensional model and examines their effect on the lack of interference between the model parts. It must be noted that the proposed technique and the written program do not belong to a specific mechanism and can be applied to any mechanism with any operation. This program calls the three-dimensional model created in SolidWorks only once. It then extracts the nominal values and part tolerances of the three-dimensional model as inputs. Next, each tolerance interval is divided into 10 or 100 equal parts, one or more of these parts are added to the nominal value step by step, and a geometric interference analysis is performed in each step.

For example, if a mechanism is composed of 10 parts, and each part has 10 significant dimensions, there will be a

total of 100 significant dimensions in the problem. Assuming the tolerance intervals of each part are divided into 10, the parts can be assembled with different (permitted and unpermitted) tolerance configurations, leading to a very large possible design space. Accordingly, only one geometric model is created in the MATLAB program, with the nominal and upper and lower tolerance bounds defined as inputs. The nominal dimensions of this model are changed by a tenth (or hundredth) of the corresponding tolerance interval, and geometric interference is examined for each state. Subsequently, tolerances causing part interference in the mechanism are decreased by a tenth (or hundredth) in each step until no interference is observed. A major advantage of this method is the shorter time it needs to reach a set of tolerances that causes no interference. Another advantage is that the designer can ensure that the selected tolerance combination does not result in the locking of the mechanism during and after assembly. Sensitivity analysis on mechanical systems, especially sensitive mechanisms, has certain complications [34-35]. According to the research done so far, the effect of temperature on the performance of sensitive mechanisms has not been done. So, the present research considers the effect of changes in temperature and the appearance of thermal strains and, thus, elastic deformation in the parts during operation. This is an important factor, especially in sensitive mechanisms, which must perform well under a wide range of temperatures. For this purpose, the temperature-related tolerance must be deducted from the design tolerance in part interference analysis. The proposed method is capable of simultaneously changing the design parameters. By analyzing the mechanism's performance under a wide range of temperatures, one can ensure the suitable performance of the product under this temperature range during its service life.

2 TOLERANCE ANALYSIS VIA PROGRAMMING

The proposed tolerance analysis is carried out as a systematic computer procedure. The first step involves an algorithm for computations designed to obtain the tolerances affecting part interference. The design specifications usually depend on the inherent properties of the system. Therefore, the dimensional and geometric deviations of the influential variables due to various sources can directly affect the performance of a mechanical system.

In a geometric interference analysis, possible part interference during assembly is examined by considering the tolerances of the manufactured parts. Using this part, one can modify the tolerances or the nominal dimensions of parts to prevent geometric interferences between them. To analyze geometric interference using the written

MATLAB program, first, all the nominal part dimensions are applied to the initial model. Then, each dimension is changed based on the corresponding defined tolerance. Next, the new model is inspected in terms of interference. The main advantage of the proposed technique (including the MATLAB program) is that remodeling by the user is not required after changing the tolerances and the three-dimensional model.

3 TOLERANCE-BASED INTERFERENCE ANALYSIS

Before the tolerance-based interference analysis, the SolidWorks assembly must be inspected concerning interference in the nominal dimensions. First, the MATLAB program calls SolidWorks in the background and stores all the part dimensions in an Excel file. Next, the upper and lower tolerances suggested for each dimension are entered by the user (or these tolerances are extracted from the model if they have been entered in the model). Subsequently, the MATLAB program divided the interval between the nominal dimension and the upper bound into 10 or 100 increments based on the user's requirements and adds one increment to the nominal value in each step. Then, the three-dimensional model is updated, and the interferences in the model are examined. If any tolerance increment causes interference in a step, the tolerance value of the previous step is stored in an Excel file as the final value, and the program moves on to the next dimension. After all the upper tolerances have been inspected, the program begins examining the lower tolerances. In this case, a tenth or hundredth of the tolerance interval is deducted from the nominal value in each step, and the optimal lower bound is also stored in the Excel file. Figure 1 displays the flowchart of the tolerance-based interference analysis using the written program.

It must be noted that the program modifies the tolerances if this resolves interferences. Sometimes, constraint-based interferences may arise, in which case the constraints must be corrected. Finally, changes in the part lengths due to thermal strain within the operational range of the mechanism are deducted from the tolerance intervals, and the optimal part tolerances appropriate for that operational range are applied to the manufacturing drawings.

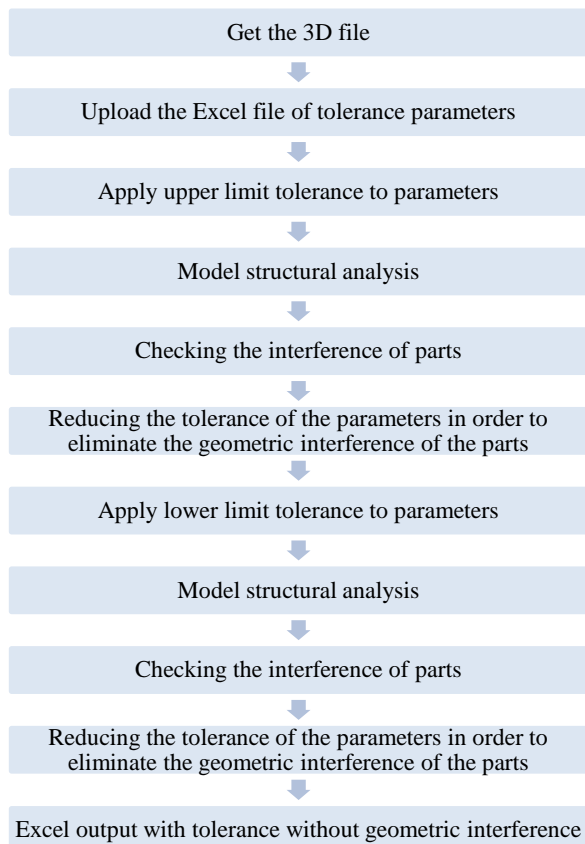


Fig. 1 Steps of the tolerance-based interference analysis.

4 FULL DESCRIPTIONS OF THE TOLERANCE-BASED INTERFERENCE ANALYSIS

4.1. Geometric Modeling

In this part, the MATLAB program calls SolidWorks. MATLAB is linked with SolidWorks and performs the required modifications via related programs on the parts and assemblies designed in SolidWorks to obtain the desired outcome from the tolerance analysis.

Every part has a simple sketch and a few features. In SolidWorks, each dimension in the sketch is exclusively specified with a name. Each of these names is assigned a value, which is the nominal size of the corresponding dimension. For instance, if a part is stored with the name Part.1 and includes a rectangular shape, each dimension of the rectangle is given a name, such as D1. The MATLAB program recognizes these dimensions with the following expressions. An example of this dimensional designation is D1@Sketch1@1.Part.

Next, MATLAB reads the nominal dimensions of each part and places them in front of the corresponding dimension name stored in the previous step. Finally, the names and dimensions are stored in a file.

The upper and lower tolerance bounds of each nominal size are manually entered into the columns of the above-

mentioned Excel file. Subsequently, the written MATLAB program examines the possible interferences caused by the tolerances in SolidWorks by considering their upper and lower bounds. Then, the tolerances written in the Excel file are read, and changes based on these tolerances are applied to the newly created model.

4.2. Changes in The Assembly Based on The New Dimensions

SolidWorks updates the model based on the tolerances in the Excel file for new interference analysis.

4.3. Inspection of Possible Interferences

In this step, the updated model is examined by the proposed method for possible interferences.

4.4. Storing of the Final Tolerance in The Output Excel File

After the final tolerance interval is determined from the interference analysis of the previous step, the new upper and lower bounds are stored in the final output file.

5 CASE STUDY

To demonstrate the implementation steps of the proposed algorithm and its effectiveness in tolerance analysis, this section investigates the mechanism of a highly sensitive and precise mechanical watch. The advanced analysis of geometric interference tolerance considers the presence of temperature variations exceeding one hundred and disregards the impact of component weights. The mechanism depicted in “Fig. 2” is a time-delay clock mechanism designed to function effectively within a temperature range of -33 to +71°C. This mechanism typically comprises three primary components: gear, weight gear, and escapement.

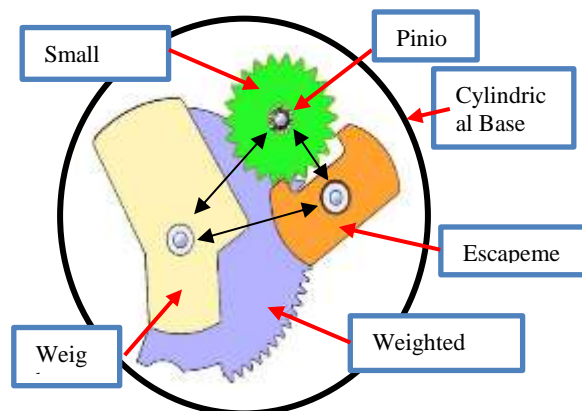


Fig. 2 Geometric model of the various components of the clock mechanism.

All the components of this mechanism are mounted on a cylindrical base plate, and based on experimental tests, its rotational speed is measured at 15000 rpm (revolutions

per minute). In this mechanism, the weight positioned outside the center of the weighted component acts as the driving force, initiating the motion. The rotation of the weight and the weighted gear occurs slowly due to the interplay of gears among the components, and it completes its motion at a specific time. As shown in “Fig. 3”, the movement of the mechanism is considered complete when the initial position of the target circle aligns with the center of the time-delay set.

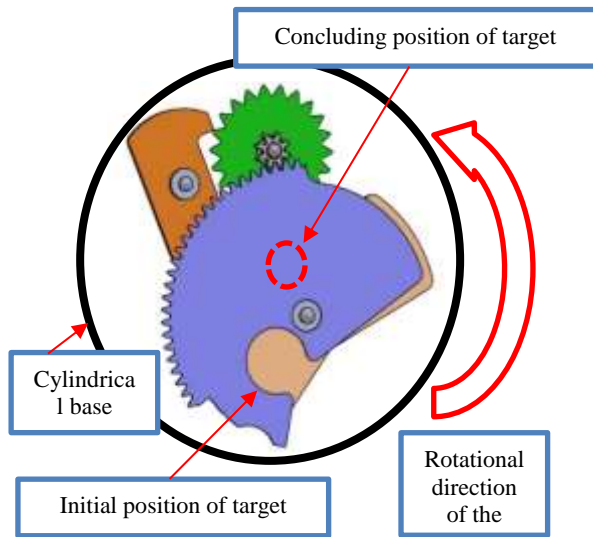


Fig. 3 The starting and ending positions of the motion.

According to the conducted experimental test, the target circle takes 0.07 seconds to reach the center of the assembly accurately. The weight located outside the assembly's center (weight and the weighted gear) is in the form of a bean-shaped weight, which is placed on the weighted gear and is also known as the weighted component. The weight initiates rotation along with the entire assembly. The motion of the weight positioned outside the center of the weighted component is transmitted to other parts by connecting it to the weighted gear, serving as the driving mechanism for the time-delay clock. This situation is depicted in “Fig. 3”.

The escapement is a mechanism that converts continuous rotational motion into intermittent movement. This component serves as an energy regulator and acts as a mechanical oscillator. Due to its control over the rotational speed of the weight, it is often recognized as the heart of the clock. One end of the escapement connects to the rotating base plate of the clock, while the other end engages with the small gear. By combining both rotational and linear forces, this mechanical system generates an oscillating motion. The functionality of this mechanism is significantly influenced by temperature and friction.

The escapement, positioned between the gear set and the oscillator, plays a crucial role in the motor's function. The

regular back-and-forth motion of the oscillator determines the time interval that the escapement transfers to the weight through the gear set. This alternating movement, coupled with the friction between components, leads to a significant energy loss. As a result, the escapement holds the most potential for enhancing the performance of mechanical clocks. With each movement, when the escapement engages in one direction, the small gear returns it to its initial position. As shown in “Fig. 4”, the axes of the time-delay clock mechanism must be installed on a plate with a coordinate tolerance of 0.05 mm, after which the assembly is subjected to angular velocity. The material and mechanical properties of the components of the time-delay clock mechanism are provided in “Table 1”.

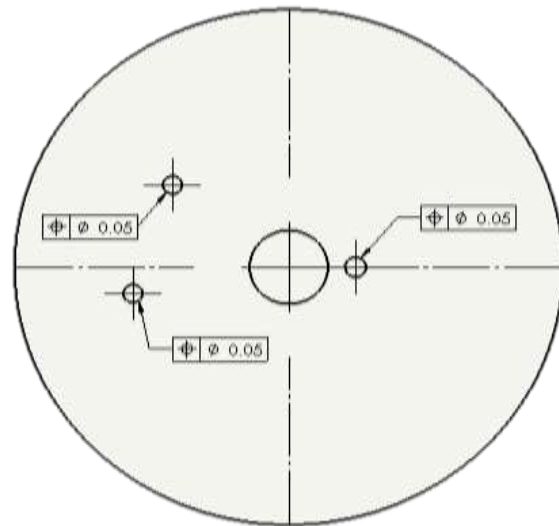


Fig. 4 The tolerance of axis positions (base plate).

Table 1 Material and mechanical properties of the components of the time-delay clock mechanism

Row	Name	Material	Young's modulus	Poisson's ratio	coefficient of thermal expansion
1	Small Gear	C26000	$10 * 10^{-11}$	0.32	$1.9 * 10^{-5}$
2	Pinion	AISI416	$2.07 * 10^{-11}$	0.29	$1.11 * 10^{-5}$
3	Escapement	C26000	$10 * 10^{-11}$	0.32	$1.9 * 10^{-5}$
4	weight	C26000	$10 * 10^{-11}$	0.32	$1.9 * 10^{-5}$
5	weight gear	C26000	$10 * 10^{-11}$	0.32	$1.9 * 10^{-5}$
6	Base Plate	AL2024-T6	$70 * 10^{-11}$	0.25	$2.38 * 10^{-5}$

As a continuation of this research, two components of the mechanism, namely the weighted component and the

base plate, were selected. Six samples of each component were placed in a refrigerator at a temperature of -33°C for a duration of six hours, and one dimension of both components was measured using an optical measurement device. The results related to the weighted component are presented in “Table 2”, while the results related to the base plate are shown in “Table 3”.

Table 2 Effect of temperature on one dimension of six samples of the weighted component

Part Name	Weight piece	Nominal dimension (mm)	4.1mm
Sample	+21°C	-33 °C	Dimension difference
1	4.115	4.114	0.001
2	4.108	4.095	0.013
3	4.096	4.087	0.009
4	4.105	4.096	0.009
5	4.117	4.098	0.019
6	4.078	4.067	0.110

Table 3 Effect of temperature on a dimensional of six cylindrical base plate samples

Part Name	Base Plate	Nominal dimension (mm)	4.45mm
Sample	+21°C	-33 °C	Dimension difference
1	4.494	4.485	0.009
2	4.477	4.476	0.001
3	4.476	4.474	0.002
4	4.484	4.476	0.008
5	4.480	4.472	0.008
6	4.492	4.489	0.003

To highlight the importance of accounting for thermal strain within the operating temperature range of -33°C to +71°C, compared to the design tolerance of time-delay clock mechanism components, an analysis was conducted on the displacement of the main axes of the mechanism concerning the center point of the base plate. The analysis was carried out using the Static-General method. Initially, the ambient temperature was set at 21°C, and then the component experienced thermal stress, reaching temperatures of +71 and -33°C, respectively. The thermal analysis employed the RT8D3C mesh. To validate the results obtained in “Figs. 5a and 5b”, the mesh sensitivity analysis is presented at two temperatures of -33 and 71 degrees Celsius. As can be seen, there is a good compatibility between these two conditions.

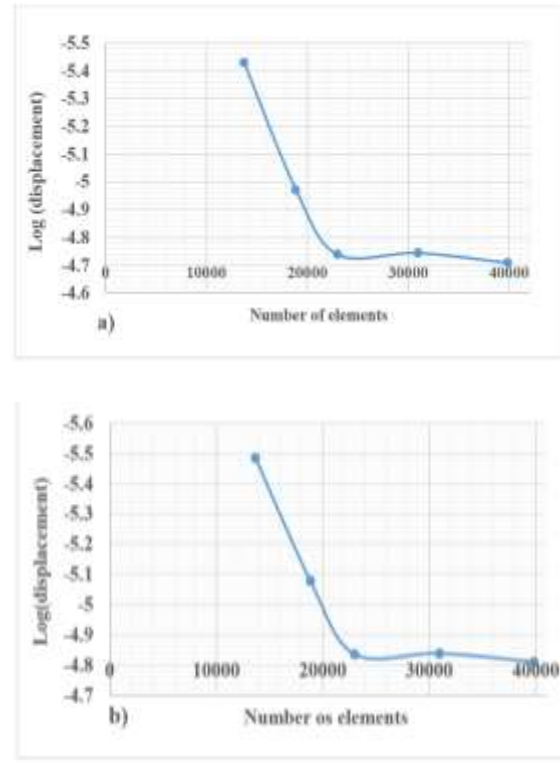


Fig. 5 Mesh sensitivity analysis at temperatures: (a): -33 degree Celsius and, and (b): +71 degree Celsius.

The deformation of the mechanism's base plate and the positioning of the axes were analysed at a temperature of -33°C, and the element displacements at this temperature are illustrated in “Fig. 6”. The positions of the axes are marked with red circles in the Figure.

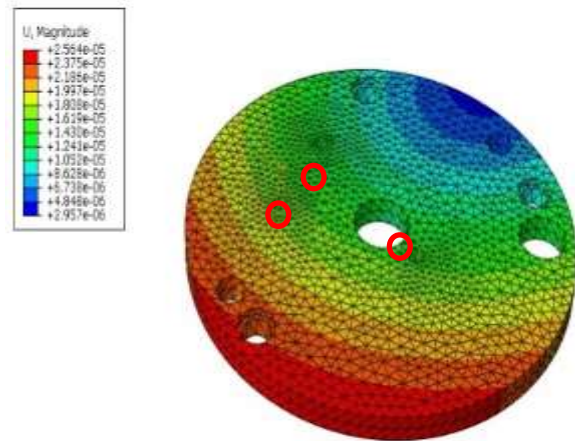


Fig. 6 Change in coordinates of axis positions on the below plate, axis positions at -33°C.

The analysis focused on the change in coordinates of the axis positions on the base plate of the clock mechanism, where the mechanism's axes are located. This analysis was conducted at a temperature of +71°C, and “Fig. 7”

illustrates the displacements of the elements at this temperature.

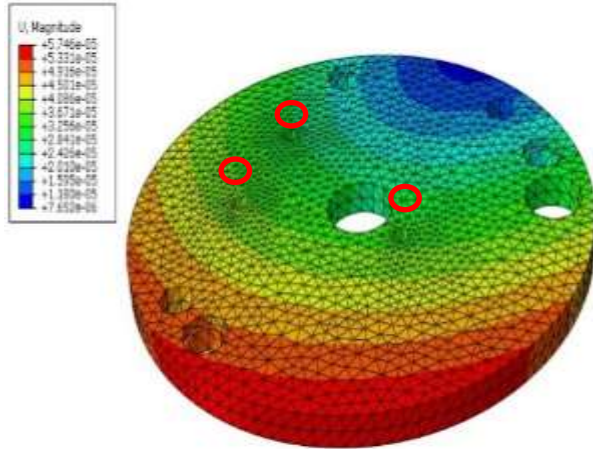


Fig. 7 Change in coordinates of axis positions on the below plate, axis positions at +71°C.

Table 4 displays the positions of the main axes at temperatures of -33 and +71°C. The results in “Table 4” indicate that the positions of the main axes fall within the manufacturing position tolerance specified by the designer, even at temperatures exceeding 100°C. This underscores the importance of conducting a thermal tolerance analysis.

Table 4 Changing the position of the axis of the delay clock in the working temperature range

Row		Dimension (mm)	change of position, mm	change of position, mm
T, °C		+21°C	-33 °C	+71°C
Position 1	X	-6.09	0.018	0.0151
	Y	-4.59		
Position 2	X	-8.15	0.0127	0.0121
	Y	1.48		
Position 3	X	3.50	0.0132	0.0110
	Y	0		

In the clock mechanism, there are 33 dimensions for all its components that require tolerance considerations during the design phase. By dividing each nominal dimension's tolerance range into ten subdivisions, approximately 10^{33} three-dimensional models need to be analysed to investigate geometric interference within both the upper and lower tolerance limits. However, the program has been developed to create only one SolidWorks geometry model using nominal dimensions. All the nominal dimensions, along with their upper and lower tolerance limits, have been inputted into the program through an Excel file. After implementing the

program and conducting the analysis to prevent component interference, it was found that only in one base plate component, the axis position tolerance needs to be adjusted from the initial value of ± 0.05 (before the geometric interference tolerance analysis) to ± 0.03 . This modification ensures that all components remain free from geometric interference at ambient temperature. However, considering that the axis positions undergo a maximum change of ± 0.02 due to thermal strain, the designer must exclude the thermal tolerance from the geometric interference tolerance assessment. As a result, a tolerance of ± 0.01 should be applied to the manufacturing drawings to ensure there are no interference issues during production.

6 CONCLUSIONS

In this research, for presenting the proposed method, coding has been carried out in a way that involves constructing only one geometric model in SolidWorks software. By providing nominal dimensions and upper and lower tolerance limits in an input file, tolerance analysis of the mechanism can be performed. To achieve this, the program can adapt the geometric model for multiple desired configurations, enabling the detection and adjustment of tolerance values that could cause component interference within the mechanism. As a result, during the assembly of the mechanism with different manufacturing tolerances for each component, the movement of various parts will be possible without any interference, ensuring the mechanism functions without any locking issues. In the current study, a precise and sensitive mechanical clock mechanism system was analyzed to showcase the effectiveness of the proposed tolerance analysis method, particularly under conditions of geometric interference. Given the requirement for precise functionality in this mechanism, any changes in the mechanism's shape due to variations in the operating temperature should not be disregarded during the design process. 24% of the examined sizes should be reduced and the tolerance for the clock axis positions in this mechanism has been modified to ± 0.01 . The tolerances have been carefully evaluated to ensure no component interference, and the tolerance for the displacement of the clock axis positions resulting from the operating temperature of the mechanism has also been calculated. The implemented program can be utilized for different types of mechanisms; it is not restricted to a specific one. Consequently, the proposed method is well-suited for precise mechanisms with a substantial number of involved components, demonstrating excellent performance.

REFERENCES

- [1] Wu, F., Dantan, J. Y., Etienne, A., Siadat, A., and Martin P., Improved Algorithm for Tolerance Allocation Based on Monte Carlo Simulation and Discrete Optimization, *Computers & Industrial Engineering*, Vol. 56, No.4, 2009, pp. 1402-1413.
- [2] Dantan, J. Y., Qureshi, A. J., Worst-Case and Statistical Tolerance Analysis Based on Quantified Constraint Satisfaction Problems and Monte Carlo Simulation, *Computer-Aided Design*, Vol. 41, No. 1, 2009, pp. 1-12.
- [3] Shekhi Azqandi, M., Hassanzadeh, M., first-and Second-Order Sensitivity Analysis of Finite Element Models using Extended Complex Variables Method, *Archive of Applied Mechanics*, Vol. 91, 2021, pp. 4263-4277.
- [4] Shekhi Azqandi, M., Hassanzadeh, M., and Arjmand, M., Calculation of Design Shape Sensitivity in Solid Mechanics Through a Novel Hybrid Method using CVM and DSM, *Journal of Stress Analysis*, Vol. 5, No. 1, 2020, pp. 11-20.
- [5] Doltsinis, I., Kang, Z., Robust Design of Structures Using Optimization Methods, *Computer Methods in Applied Mechanics and Engineering*, Vol. 193, No. 23, 2004, pp. 2221-2237.
- [6] Zang, C., Friswell, M., and Mottershead, J., A Review of Robust Optimal Design and Its Application in Dynamics, *Computers and structures*, Vol. 83, No. 4-5, 2005, pp. 315-326.
- [7] Huang, X., Zhang, Y., Robust Tolerance Design for Function Generation Mechanisms with Joint Clearances, *Mechanism and machine theory*, Vol. 45, No. 9, 2010, pp. 1286-1297.
- [8] Zhou, K., Cai, Y., Zhang Z. J., and LI, X. Y., Application of the Theory of Robust Design in Tolerance Analysis, *Transactions of Beijing Institute of Technology*, Vol. 23, 2003, pp. 557-560.
- [9] Shao, N., Ding, X., Liu, J., Tolerance Analysis of Spur Gears Based on Skin Model and Boundary Element Method, *Mechanism and Machine Theory*. Vol. 144, 2020, pp. 103658.
- [10] Geetha, K., Ravindran, D., Kumar, M. S., and Islam, M. N., Concurrent Tolerance Allocation and Scheduling for Complex Assemblies, *Robotics and Computer-Integrated Manufacturing*, Vol. 35, 2015, pp. 84-95.
- [11] Shoukr, D. S. L., Gadallah, M. H., and Metwalli, S. M., The Reduced Tolerance Allocation Problem, *ASME International Mechanical Engineering Congress and Exposition*, Phoenix, IMECE2016-65848, V011T15A023, Arizona, USA, 2016.
- [12] Khodaygan, S., Meta-Model Based Multi-Objective Optimization Method for Computer-Aided Tolerance Design of Compliant Assemblies, *International Journal of Computer Integrated Manufacturing*, Vol. 32, No. 1, 2018, pp. 27-42.
- [13] Delos, V., Arroyave-Tobón, S., and Teissandier, D., Introducing a Projection-Based Method to Compare Three Approaches to Computing the Accumulation of Geometric Variations, In *38th International Design Engineering Technical Conferences and Computers and Information in Engineering Conference*, Quebec City, Canada, 2018.
- [14] Lin, E. E., Zhang H. C., Theoretical Tolerance Stack Up Analysis Based on Tolerance Zone Analysis, *The International Journal of Advanced Manufacturing Technology*, Vol. 17, No. 4, 2001, pp. 257-262.
- [15] Wang, Y., Closed-loop analysis in semantic tolerance modeling, *Journal of Mechanical Design*, Vol. 130 No.6, pp. 061701-061711. 2008.
- [16] Geis, A., Husung, S., Oberänder, A., Weber, C., and Adam, J., Use of Vectorial Tolerances for Direct Representation and Analysis in CAD-Systems, *Procedia Cirp*, Vol. 27, 2015, pp. 230-240.
- [17] Heling, B., Aschenbrenner, A., Walter, M., and Wartzack, S., On Connected Tolerances in Statistical Tolerance-Cost-Optimization of Assemblies with Interrelated Dimension Chains, *Procedia Cirp*, Vol. 43, 2016, pp. 262-267.
- [18] Kopardekar, P., Anand, S., Tolerance Allocation Using Neural Networks, *The International Journal of Advanced Manufacturing Technology*, Vol. 10, No. 4, 1995, pp. 269-276.
- [19] Luo, C., Franciosa, P., Ceglarek, D., Ni, Z., and Jia, F., A Novel Geometric Tolerance Modeling Inspired by Parametric Space Envelope, *IEEE Transactions on Automation Science and Engineering*, Vol. 15, No. 3, 2018, pp. 1386-1398.
- [20] Samper, S., Formosa, F., Form Defects Tolerancing by Natural Modes Analysis, *Journal of Computing and Information Science in Engineering*, Vol. 7, No. 1, 2007, pp. 44-51.
- [21] Homri, L., Goka, E., Levasseur, G., and Dantan, J.-Y., Tolerance Analysis—Form Defects Modeling and Simulation by Modal Decomposition and Optimization, *Computer-Aided Design*, Vol. 91, 2017, pp. 46-59.
- [22] Lin, E. E., Graph-Matrix-Based Automated Tolerance Analysis and Setup Planning in Computer-Aided Process Planning, Ph.D. Dissertation, Industrial Engineering, Texas Tech University, 2000.
- [23] Zhang, K., Li, Y., and Tang, S., An Integrated Modeling Method of Unified Tolerance Representation for The Mechanical Product, *The International Journal of Advanced Manufacturing Technology*, Vol. 46, No. 1, 2010, pp. 217-226.
- [24] Schleich, B., Wartzack, S., Anwer, N., and Mathieu, L., Skin Model Shapes: Offering New Potentials for Modeling Product Shape Variability, In *35th Computers and Information in Engineering Conference*, Boston, Massachusetts, USA, 2015.
- [25] Schleich, B., Anwer, N., Mathieu, L., and Wartzack, S., Skin Model Shapes: A New Paradigm Shifts for Geometric Variations Modeling in Mechanical Engineering, *Computer-Aided Design*, Vol. 50, 2014, pp. 1-15.

- [26] Yacob, F., Semere, D., and Nordgren, E., Octree-Based Generation and Variation Analysis of Skin Model Shapes, *Journal of Manufacturing and Materials Processing*, Vol. 2, No. 3, 2018, pp. 52-73.
- [27] Yan, X., Ballu, A., Generation of Consistent Skin Model Shape Based on FEA Method, *The International Journal of Advanced Manufacturing Technology*, Vol. 92, No. 1, 2017, pp. 789-802.
- [28] Schleich, B., Anwer, N., Mathieu, L., and Wartzack, S., Contact and Mobility Simulation for Mechanical Assemblies Based on Skin Model Shapes, *Journal of Computing and Information Science in Engineering*, Vol. 15, No. 2, 2015, pp. 021009-021009-7.
- [29] Dantan, J. Y., Comparison of Skin Model representations and Tooth Contact Analysis Techniques for Gear tolerance analysis, *Journal of Computing and Information Science in Engineering*, Vol. 15, No. 2, 2015, pp. 021009-7.
- [30] Yan, X., Assembly Simulation and Evaluation Based on Generation of The Virtual Work Piece with Form Defect, Ph.D. Dissertation, Mechanical Engineering, Bordeaux, France, 2018.
- [31] Faraji, F., Abbasi, K., Experimental Study of the Effect of Conventional Manufacturing Geometric Deviation in the Fitted Cylindrical Joint on its Strength, *Karafan Quarterly Scientific Journal*, Vol. 19, No. 1, 2022, pp. 107-123.
- [32] Ghodsbin, J. A., Hatami, H., Numerical Behaviour Study of Expanded Metal Tube Absorbers and Effect of Cross Section Size and Multi-Layer Under Low Axial Velocity Impact Loading, *Amirkabir Journal of Mechanical Engineering*, Vol. 49, No. 4, 2018, pp. 245-248.
- [33] Hatami, H., Fathollahi, A. B., The Theoretical and Numerical Comparison and Investigation of The Effect of Inertia on The Absorbent Collapse Behavior of Single Cell and Two-Cell Reticular Under Impact Loading, *International Journal of Impact Engineering*, Vol. 109, 2017, pp. 224-239.
- [34] Hassanzadeh, M., Mazare, M., Computation of Design Sensitivities in Steady-State Incompressible Laminar Flows Based On New Semi-Analytical Method, *Journal of Scientific Computing*, Vol. 83, No. 12, 2020.
- [35] Sheikhi Azqandi, M., Hassanzadeh, M., and Arjmand, M., Sensitivity Analysis Based on Complex Variables in FEM for Linear Structures, *Advances in Computational Design*, Vol. 4, No. 1, 2019, pp. 15-32.

Nonlinear Mechanical Properties of Random Networks Composed of Nonlinear Fibers

Reyhane Mirkhani, Ali Asghar Alamdar Yazdi*

Department of Textile Engineering, Yazd University, Yazd, Iran

E-mail: mirkhani@stu.yazd.ac.ir, aalamdar@yazd.ac.ir,

*Corresponding author

Saeid Ebrahimi

Department of Mechanical Engineering, Yazd University, Yazd, Iran

E-mail: ebrahimi@yazd.ac.ir

Received: 10 August 2021, Revised: 26 November 2021, Accepted: 10 December 2021

Abstract: The disordered fibrous networks provide load-bearing and main structural to different biological materials such as soft tissues. These networks display a highly nonlinear stress-strain relationship behavior when subjected to mechanical loads. This nonlinear strain-stiffening behavior is dependent on the network microstructure and properties of constituting fiber. We conduct a comprehensive computational study to characterize the importance of material properties of individual fibers as well as the local connectivity or coordination number and bending rigidity in the overall nonlinear mechanical response of a 3D random fiber network. The presented model shows the nonlinear stiffening with increasing applied shear strain more than critical shear strain. We determine the amount of strain-stiffening as a function of network microstructure parameters and the amount of nonlinearity of the fibers. The results show that the constitutive behavior of fibers displays much more strain-stiffening than networks made up of linear fibers. We find that the importance of the nonlinear reaction of individual fiber materials in the general mechanical behavior of networks becomes more important with increasing network connectivity. Furthermore, the amount of stress created in the network under shear increases with the enhanced connectivity of the network due to an increase in the network stiffness. Our model points to the important role of the mechanical response of individual fiber as well as the microstructure of the network in determining the overall mechanical properties of the 3D random network, which could be used to design and better understand the complex biomimetic network systems such as biological tissues and artificial engineering networks.

Keywords: Athermal Fibers, Biopolymer Networks, Lattice Structure, Mechanical Properties, Nonlinear Fiber, Random Networks

Biographical notes: **Reyhane Mirkhani** is a PhD student in Textile Engineering at Yazd University. Her field of research is the Mechanical Behavior of fiber networks. **Aliasghar Alamdar Yazdi** is Assistant Professor of Textile Engineering at Yazd University. His research field of study focuses on the Mechanical Behavior of Yarns and Fabrics. **Saeid Ebrahimi** is currently Associate Professor of Mechanical Engineering at Yazd University and his main research interests are Multibody Systems Dynamics, Robotics, Vibration Analysis of Mechanical Systems and Mechanism Analysis.

Research paper

COPYRIGHTS

© 2024 by the authors. Licensee Islamic Azad University Isfahan Branch. This article is an open access article distributed under the terms and conditions of the Creative Commons Attribution 4.0 International (CC BY 4.0)

<https://creativecommons.org/licenses/by/4.0/>



1 INTRODUCTION

Biopolymer networks as the major part of the structure of living materials need to be recognized and evaluated for their mechanical properties. These networks are present in a wide range such as collagen and the actin cortex of eukaryotic cells [1]. In order to evaluate the shape and structure of the cell as well as its function, it is necessary to know the mechanical properties of the cytoskeleton and the extracellular matrix [2]. The most abundant fibrous protein, which is mainly found in various tissues such as articular cartilage, ligaments, cornea, and tendons, is collagen which shows the nonlinear elastic response [3-4]. This material has been considered as a major component in the performance and mechanical properties of the extracellular matrix and plays a major role in the fiber network [5-6]. Due to the widespread presence of fiber networks in various vital processes such as cellular motility [7], mechanical cell-cell communication [8-9], and stress management in articular cartilage [10], understanding the nonlinear mechanical response of fibrous networks and the effect of architecture parameter on it, are always been considered as challenging issues by researchers.

Various experimental and numerical studies have been performed on biopolymer networks; the results of these studies have shown nonlinear elastic behavior as well as large deformations in the network under different loading conditions [11-14]. In general, based on the elastic properties and network architecture, these types of networks are classified as semi-flexible biopolymer networks [15-16]. Researchers have mainly evaluated the behavior and performance of the fiber network based on affine models. In affine models, it is assumed that fiber segments are deformed based on far-field strain [5]. In these models, the mechanical behavior of the fiber network has been influenced by microstructural parameters such as fiber orientation and cross-link density [11-12]. But in reality, the behavior and mechanical responses of fiber networks, especially biological materials, are nonaffine. This issue has been important because in order to conduct detailed studies on these networks, nonlinear behavior and properties must be considered [17]. To date, various numerical studies have been performed in the form of affine and non-affine models with lattice-based and off-lattice network structures for assessing the origins of the nonlinear elasticity of fibrous networks [18-23].

Previous studies using numerical models have investigated that nonlinear strain-stiffening behavior is related to their architecture and mechanical properties of their fibrous constituents [24-32]. Moreover, the specific structural parameter of networks has been shown to have a significant influence on certain aspects of their mechanical response [33-34]. However, according to the real structure of the fiber network, there

is a need to study and evaluate the network in 3D space, and little attention has been paid to the 3D random networks constituting nonlinear fibers that could play in controlling the nonlinear elasticity of random networks. The primary objective of this study is to provide a thorough investigation of how material properties of individual fibers along with various geometrical network parameters, such as network connectivity, and bending rigidity, affect the nonlinear mechanics of 3D random networks. For this purpose, we present the microstructure of 3D networks as disordered and diluted faced-centered cubic lattices with different connectivity. In the model, the stress-strain response of individual fibers is represented by an exponential function to study the nonlinear mechanical response of 3D random networks, in which nonlinearity is varied from low to high. The computer simulation is used to study the mechanical response of fibrous networks subjected to simple shear. The effects of geometrical parameters of the 3D random networks being composed of nonlinear fibers and their relation to the nonlinearity of the network mechanical response are also characterized. The influence of the nonlinear stress-strain behavior of fibers on the network shear modulus is also studied. The numerical results show that the mechanical properties of constituting fibers and geometrical network parameters have important effects on the mechanical response of 3D random polymer networks.

2 PROCEDURES FOR PAPER SUBMISSION

In this research, by evaluating the research background and the results of previous research, the main parameters in evaluating the mechanical behavior and responses of the fiber network are identified and categorized. Based on the extracted parameters, research scenarios are created to implement the studies. Under the research scenarios, parametric studies are performed using numerical modeling. In this section, research variables are evaluated, as well as research scenarios and numerical models are presented.

2.1. Numerical Model Specifications

In this research, in order to evaluate the mechanical properties and responses of the 3D fiber network, the network microstructure (network connectivity, bending rigidity) and properties of constituting fiber are examined, and the models are implemented based on the change in these parameters and the results are obtained.

Network Structure

Various structures such as lattice-based and off-lattice network structures can be used to perform numerical studies on fiber networks. In this study, because of the superior features of the lattice structure in modeling network architecture, we use this structure to conduct

studies. Due to the conditions and 3D modeling space, we used the faced-centered cubic lattice (FCC) structure to model the fiber network. Figure 1a shows a schematic view of an FCC lattice network.

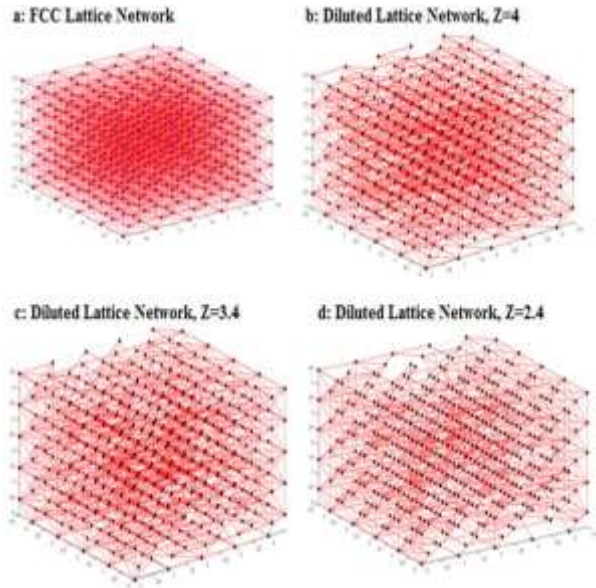


Fig. 1 Fiber network structure: (a): FCC Lattice Network, (b): Diluted Lattice Network $Z=4$, (c): Diluted Lattice Network $Z=3.4$, and (d): Diluted Lattice Network $Z=2.4$.

Network Connectivity

Biopolymer materials mainly form cross-linked network structures. The network connectivity indicates the average number of cross-links in a polymer network. In natural tissues, the average cross-links (Z) of biopolymer materials are between 2 and 4. [20], [35-37]. The network connectivity parameter has been one of the effective criteria in the stabilization and stability of polymer networks, which has an important role in the mechanical properties and network responses under different loading conditions [36]. In this research, to create 3D polymer networks with average variable connectivity ($2 < Z < 4$), first a complete faced-centered cubic lattice network with $W \times W \times W$ dimensions has been created. The maximum number of cross links in 3D networks is 12 ($Z_{max}=12$). The next step is to dilute the network by randomly removing the components with a $q=1-p$ (p is a Possibility of existence) probability in order to adjust the average network connectivity. In this research, we have considered the dimensions of the network as $4.5 \times 4.5 \times 4.5$ ($w = 4.5$ mm). We have also considered the values of network connection (Z) in 3 conditions ($Z = 2.4, 3.6, 4$) in the numerical studies (“Fig. 1. b-d”).

Bending Rigidity

One of the effective parameters in evaluating fiber network responses and their mechanical behavior is dimensionless bending rigidity. This parameter is defined based on the physical and mechanical properties of the fiber segment and is considered as an effective factor in tensile, shear, and bending deformations. In order to numerical model the fiber network composed of elastic athermal fiber, the beam element is used. Assuming the physical properties of the beam element as follows, the dimensionless bending rigidity relationship can be formulated [37].

- A : cross-sectional area of the beam element
- I : second moment of inertia
- E : Young’s modulus
- μ : stretching modulus - $\mu = EA$
- κ : bending rigidity - $\kappa = EI$
- $\bar{\kappa}$: dimensionless bending rigidity - $\bar{\kappa} = \kappa/\mu l^2$

The $\bar{\kappa}$ parameter represents the flexibility of the fibers. Because of its significant effect on the properties of the fiber network, we have considered it as one variable of this research.

Nonlinear Fiber Behavior

The fibers are modeled as Timoshenko beams taking into account their stretching, shear, and bending deformations. For networks composed of linear elastic fibers, the beam segments are assumed to have cross-sectional area A , second moment of inertia I , Young’s modulus E , stretching modulus $\mu = EA$, and bending rigidity $\kappa = EI$, and thus, dimensionless bending rigidity $\bar{\kappa} = \kappa/\mu l^2$ [5]. The dimensionless bending rigidity quantifies the flexibility of the fibers and is varied from 0.001 to 0.1 in the present study reported in the literature [1], [5]. To evaluate the nonlinear behavior of fibers in a 3D network, the exponential function to represent the stress-strain response of nonlinear fibers has been used based on (H. Marbini & M. Rohanifar, 2020) [5]. According to the proposed model, the fibers have an initial linear elastic response followed by an exponential hardening reaction [5], [36]. The proposed relationship between the stress-strain of the fibers is formulated according to Equation (1).

$$\sigma_f = \begin{cases} E\varepsilon & \varepsilon \leq \varepsilon_y \\ EB \left(e^{\frac{\varepsilon - \varepsilon_y}{B}} - 1 \right) + E\varepsilon_y & \varepsilon > \varepsilon_y \end{cases} \quad (1)$$

Where ε_y represents the strain at which the linear behavior of the material switches to exponential form, B is a parameter for controlling the nonlinearity of the material behavior, which varies between 1 and 0.1.

The major purpose of this study is to evaluate the performance and mechanical properties of the fiber networks under shear loading. In this regard, as shown in “Fig. 2”, to apply the shear strain γ to random fiber network, all fibers intersecting the vertical boundary are only fixed in the horizontal and vertical directions, and those attaching to the opposite side boundary are constrained to translate vertically down. The finite shear strain γ is applied incrementally from 0 to 100%. Once the finite element simulation results are obtained, we calculate the shear stress by dividing the summation of forces in the fibers intersecting the upper lattice boundary by W . The differential shear modulus of the networks, also referred to as stiffness herein, at each increment is defined as the slope of the stress-strain response, i.e. $K = d\sigma/d\gamma$, where γ and σ are the applied shear strain and calculated shear stress, respectively. In the following, the stress and stiffness are given in units of μ/l .

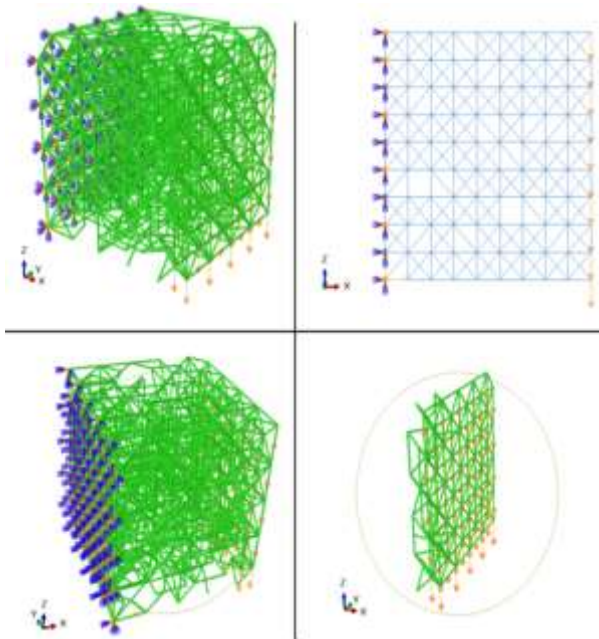


Fig. 2 Initial and boundary conditions of the research models.

2.2. Research Scenarios

In order to evaluate the mechanical behavior and responses of the fiber network accurately, after extracting the main effective variables and parameters, numerical modeling scenarios are defined.

According to the research variables that were introduced in the previous section, the modeling scenarios have been as follows.

- Network connectivity variable: we consider three different values $Z=2.4, 3.4,$ and 4 [20], [35-37] for the average fiber network connectivity.

- Bending rigidity variable: In order to evaluate the performance of the network and its flexibility, the properties of the beam element that represents the fiber segment are defined in such a way that three different values for the dimensionless bending rigidity ($\bar{\kappa}$) are studied (0.1, 0.01 and 0.001).
- Nonlinear fiber variable: Based on the explanations provided in the previous section, it is clear that parameter B in equation 1 is considered to control the nonlinear performance of the material, therefore we considered three different values $B=1, 0.2,$ and 0.1 for slightly nonlinear, nonlinear and highly nonlinear for this parameter as mentioned in literature [5]. Figure 3 shows the nonlinear behavior of the fiber material (normalized stress-strain response curve) based on different values of parameter B [5].

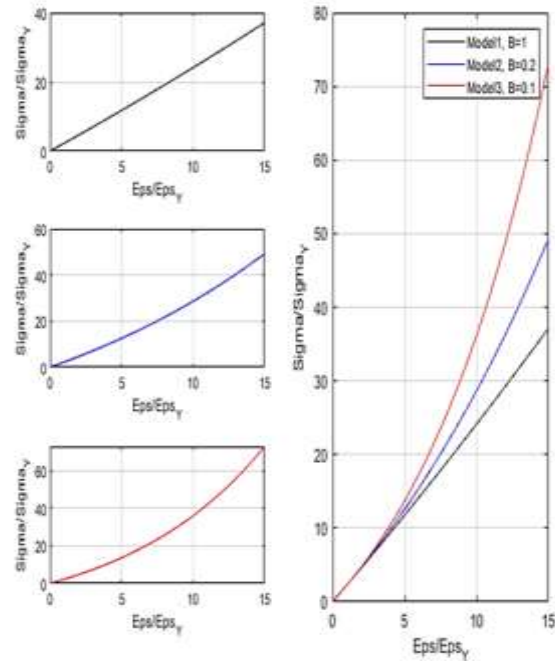


Fig. 3 The normalized stress-strain response of fibers Based on changes in B .

According to the proposed variables and to evaluate the impact of each variable, the numerical modeling scenario is defined taking into account all possible cases and 27 models are planned to model comprehensive parametric studies (“Table 1”). In this research, parametric studies and numerical modeling based on defined scenarios have been performed in Abacus finite element software. In this regard, Python programming language has been used to define the various structures of the fiber network as well as the nonlinear properties of the fiber material.

Table 1 Research modeling scenarios

scenarios NO.	Model Name	Network connectivity (Z)			Non-Linear Material Properties (B)			Dimensionless bending rigidity (\bar{k})		
		Z = 2.4	Z = 3.4	Z = 4	B = 1	B = 0.2	B = 0.1	$\bar{k} = 0.1$	$\bar{k} = 0.01$	$\bar{k} = 0.001$
1	M1	✓			✓			✓		
2	M2	✓			✓				✓	
3	M3	✓			✓					✓
4	M4	✓				✓		✓		
5	M5	✓				✓			✓	
6	M6	✓				✓				✓
7	M7	✓					✓	✓		
8	M8	✓					✓		✓	
9	M9	✓					✓			✓
10	M10		✓		✓			✓		
11	M11		✓		✓				✓	
12	M12		✓		✓					✓
13	M13		✓			✓		✓		
14	M14		✓			✓			✓	
15	M15		✓			✓				✓
16	M6		✓				✓	✓		
17	M17		✓				✓		✓	
18	M18		✓				✓			✓
19	M19			✓	✓			✓		
20	M20			✓	✓				✓	
21	M21			✓	✓					✓
22	M22			✓		✓		✓		
23	M23			✓		✓			✓	
24	M24			✓		✓				✓
25	M25			✓			✓	✓		
26	M26			✓			✓		✓	
27	M27			✓			✓			✓

3 RESULTS AND DISCUSSION

In this section, the results of numerical modeling and parametric studies performed according to research scenarios (“Table 1”) are presented. The outputs of numerical modeling include a wide range of results, which are categorized as follows because of the accurate evaluation of mechanical properties and 3D random network fiber responses.

- Assessment of von Mises stresses
- Assessment of the network shear modulus
- Investigation of bending and stretching energy to total energy
- Differential shear modulus vs. shear stress
- Effect of network connectivity on the mechanical response of 3D random fiber networks

3.1. Assessment of Von Mises Stresses

One of the useful parameters for evaluating the performance of 3D random networks under shear is von Mises stress, the results are presented in “Figs. 4 to 6.”

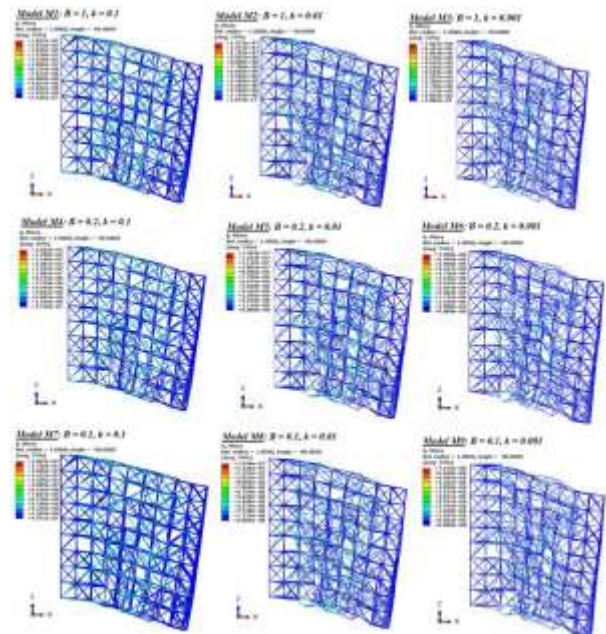


Fig. 4 Von Mises stress results, 3D random fiber network with Z=2.4 (M1 to M9 models).

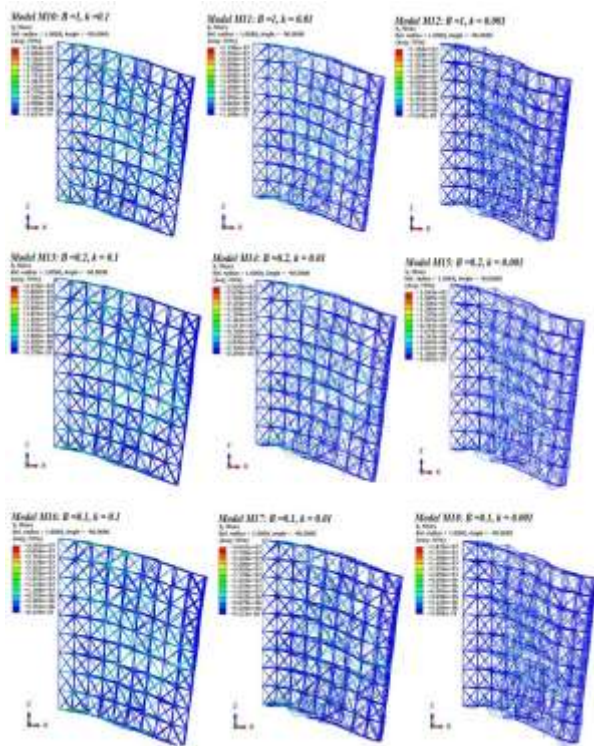


Fig. 5 Von Mises stress results, 3D random fiber network with Z=3.4 (M10 to M18 models).

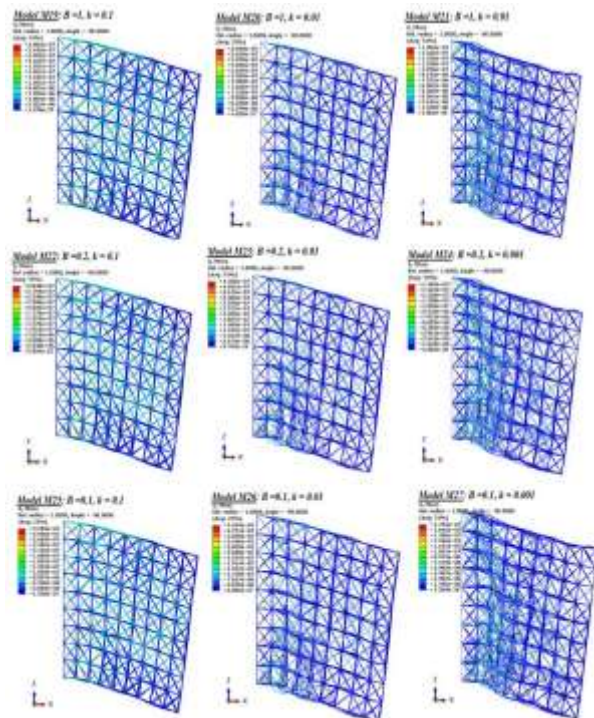


Fig. 6 Von Mises stress results, 3D random fiber network with Z=4 (M19 to M27 models).

Models M₁ to M₉ have a random 3D network structure with an average connectivity (Z=2.4). Figure 4 shows the results of von Mises stress for this network structure

under shear. Models M₁₀ to M₁₈ have a random network with an average connectivity Z=3.4 and models M₁₉ to M₂₇ have a network with Z=4. Figures 5 and 6 show the Von Mises stress under shear for the network with Z=3.4 and Z=4, respectively. Figures 4 to 6 show the von Mises stresses created in the fiber network with Z = 2.4, 3.4, 4, respectively. According to the results, it is clear that by reducing the amount of the dimensionless bending rigidity (k) from 0.1 to 0.001, the stress in the network under shear has decreased. Because of the nature of the k parameter, it is clear that by reducing this parameter, the flexural stiffness of the network is decreased and the stress in the network is reduced. Also, by evaluating the change in parameter B, which represents the degree of nonlinearity of the fiber material, it is determined that with decreasing B from 1 to 0.2, the values of stress are increased. In addition, in the network with highly nonlinear fibers (B = 0.2), the number of plastic distortions and deformations of the fibers is clearly visible.

3.2 Assessment of the Network Shear Modulus

Based on the results of various numerical and experimental studies, it was found that random fiber networks under large shear, exhibit notable strain-stiffening. Therefore, the shear stiffness of these networks increases significantly with strain. This stiffening behavior mainly depends on the fiber bending rigidity and the connectivity of random networks [37-39].

To evaluate the effect of nonlinear fibers on the mechanical behavior of three-dimensional random fiber networks, the shear stiffness of networks composed of nonlinear fibers based on normalized shear strain for different values of the dimensionless bending rigidity is shown in “Fig. 7”. In these diagrams, the shear stiffness K is normalized by the stiffness of a similar network composed of linear elastic fibers. In addition, the applied shear strain normalized by γ_d . γ_d is the far-field shear strain at which the strain in at least one of the fiber sections reaches the yielding strain ϵ_y [5].

Figure 7 plots the normalized shear stiffness of networks composed of nonlinear fibers with different values of the dimensionless bending rigidity ($\bar{\kappa}$) as a function of normalized shear strain. In these plots, the shear stiffness K and shear strain γ is normalized with the stiffness of similar networks composed of linear elastic fibers and by γ_d , which is the far-field shear strain at which the strain in at least one of the fiber segments reaches the yielding strain ϵ_y , equation 1, respectively [5]. As shown in “Fig. 7” with various $\bar{\kappa}$, they display nonlinear mechanical response. Moreover, the mechanical properties of networks with increased nonlinear fiber variable become different from networks composed of only linear elastic fibers, the random 3D fiber network has average network connectivity equal to 2.4 (Z=2.4). According to the results, the shear stiffness changes

proportional to the nonlinear performance of the material.

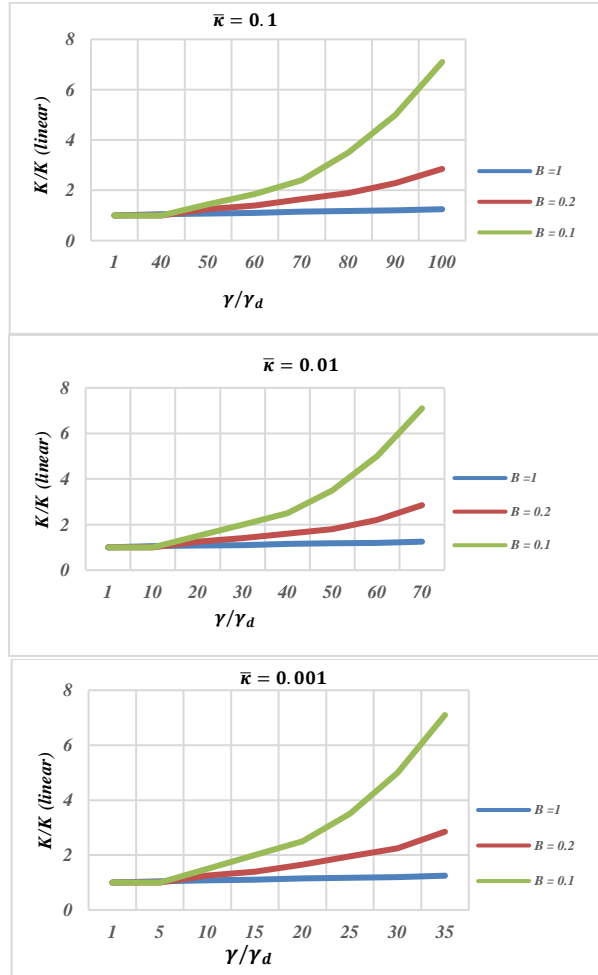


Fig. 7 The effect of nonlinear elastic properties of individual fibers on the mechanical response of fibrous networks, shear stiffness of networks composed of nonlinear fibers based on normalized shear strain for different values of the dimensionless bending rigidity ($\bar{\kappa}$).

In addition, the changes in the first section appear linearly and then exponentially. In addition, the changes in the first section appear linearly and then exponentially. According to the results, with decreasing bending rigidity from 1 to 0.1, the linear region changes from 40% γ to 7% γ , respectively.

3.3. Investigation of Bending and Stretching Energy to Total Energy

Based on the results obtained from modeling in this study, it is clear that with increasing applied shear strain and also with increasing bending rigidity of fibers, the nonlinear behavior of the fiber material becomes more apparent. In this regard, the evaluation of changing in the bending energy (H_b) and stretching energy (H_s) relative to the total applied energy to the random 3D fiber

network, can provide a correct understanding of the mechanical behavior of the 3D random networks. It should be noted that the total energy is equal to the sum of bending energy and stretching energy in the network.

$$H_t = H_b + H_s \quad (2)$$

The stiffening corresponds to a transition from bending- to stretching-dominated behaviour [22]. Figure 8 shows the relative contributions of stretching energy (H_s) and bending energy (H_b) versus the applied shear strain for M_7 to M_9 Models. Models M_7 to M_9 have a highly nonlinear fibre behavior ($B = 0.1$).

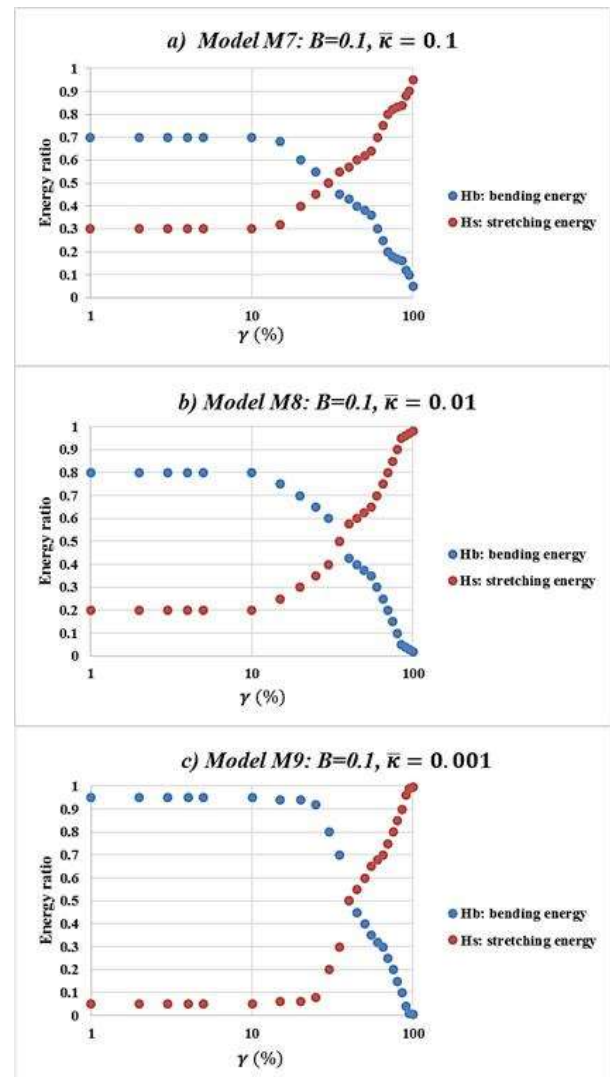


Fig. 8 Relative contributions of stretching energy (H_s) and bending energy (H_b) versus the applied shear strain for M_7 to M_9 Models.

According to “Fig. 8”, it is clear that the bending rigidity ($\bar{\kappa}$) has been an effective component in changing stretching energy H_s and bending energy H_b . By

decreasing this parameter from 0.1 to 0.001, the critical shear strain γ_c changes from 30% γ to 41% γ , respectively. These results indicate that with increased network connectivity and bending stiffness more energy is stored in stretching modes. Therefore, the random network will move from the bending-dominated regime towards an affine, stretch-dominated

3.4. Differential Shear Modulus vs. Shear Stress

Stress-stiffening has been one of the important parameters in studying the mechanical properties of random 3D fiber networks. In this section, variation of the differential shear modulus of nonlinear fiber networks versus the shear stress is presented for different bending rigidity regimes (“Fig. 9”).

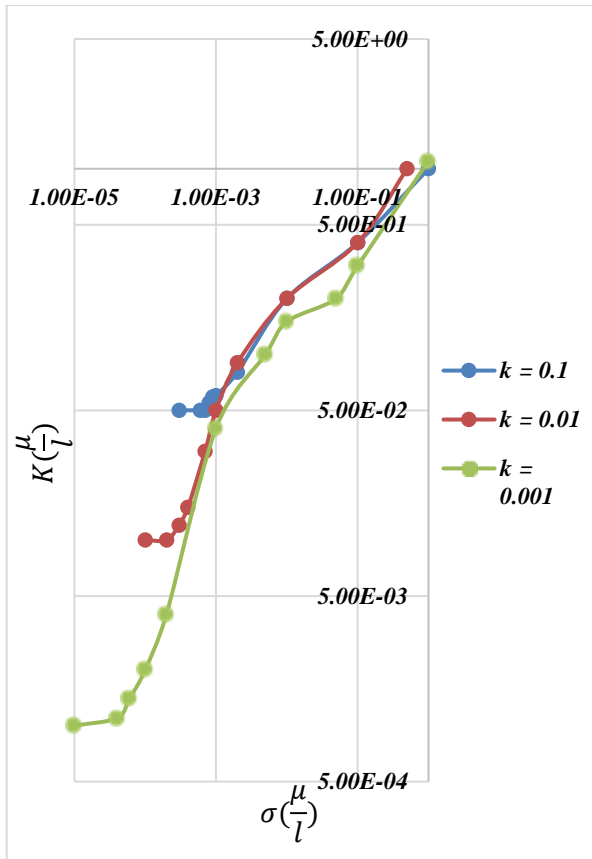


Fig. 9 The variation of the differential shear modulus of nonlinear fiber networks versus the shear stress for different values of the dimensionless bending rigidity (\bar{k}).

In general, the relationship between K and stress (σ) is as follows.

$$K \propto \sigma^\alpha \tag{3}$$

In relation 3, α varies between 0.6 and 1.5 for biopolymer materials, which according to the results of this study, this value is also true for the random 3D fiber networks. The α parameter depends on the bending

rigidity of fibers and varies from about 1.1 ($K = 0.001$) to 0.7 ($K = 0.1$). These findings agree with previous numerical, experimental, and theoretical reports that show that the exponent increases from 0.7 to 1.1 with a decline K for networks [1], [5], [22-23].

3.5. Effect of Network Connectivity on Mechanical Response of 3D Random Fiber Networks

To evaluate the effect of the network connectivity parameter (Z), The shear modulus K is plotted as a function of the applied shear strain for networks composed of nonlinear fiber and based on variation of the network connectivity (Z).

Figure 10 plots the shear modulus as a function of the applied shear strain for networks with various connectivity. An increase in network connectivity enhances the effect of the material nonlinearity of fibers on the network stiffness. Furthermore, the critical strain shifts towards smaller strains with increasing Z , which means that fibers reach their yielding strain at a smaller applied shear strain. The results also show good compatibility between the nonlinear material model and the shear model variation.

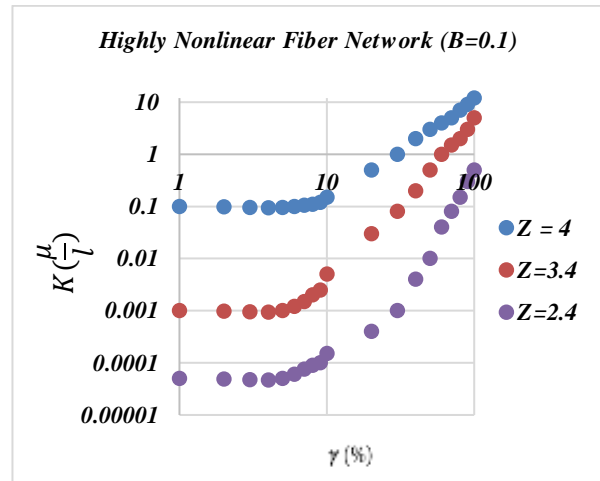


Fig. 10 The shear modulus K vs the applied shear strain for different network connectivity.

4 CONCLUSIONS

In this research, comprehensive parametric studies have been defined and implemented in order to evaluate the mechanical properties and investigate the responses of 3D random fibrous networks under shear loading. In the first step, the effective parameters in 3D random networks were identified and based on the research variables, numerical modeling scenarios have been developed. At this stage, 4 parameters (1- network structure, 2- average network connectivity, 3- bending rigidity and 4- nonlinear fiber behavior) were selected as the main variables of the research. Based on these

parameters, 27 different models have been modeled for conducting studies in Abacus software.

The results of the present study indicate the effect and sensitivity of each of the research variables on the mechanical behavior and responses of a 3D random fibrous network. The general results of this research can be classified as follows:

- Based on the results of the study, it is determined that the parameters of network structure, average network connectivity, bending rigidity, and nonlinear behavior of fiber material are effective factors in the mechanical behavior of 3D random fibrous networks.
- Based on von Mises stress evaluation in 3D fiber networks, it showed that with increasing network connectivity, the amount of stress created in the network under shear increases. This indicates an increase in the stiffness of the network, also a decrease in dimensionless bending rigidity reduces the stresses created in the 3D fiber network.
- The network connectivity parameter (Z) plays an important role in how the nonlinearity of single fibers affects the overall strength of 3D networks.
- The results of the present research show that in the 3D random network with increasing applied shear strain more than γ , significant strain-stiffening is observed. This phenomenon is more pronounced in highly nonlinear fiber networks.
- Examining the relationship between shear modulus and shear stress, it is clear that the variation of the differential shear modulus of nonlinear fiber networks versus the shear stress in 3D random networks has been consistent with theoretical relationships and the results of numerical and experimental research.
- The results of applying the nonlinear fiber material model in 3D random networks show that the exponential function to represent the stress-strain response of nonlinear fibers is well adapted to evaluate the nonlinear behavior of 3D random fibrous networks. The results of the present research show that using the lattice network structure for modeling and evaluating the mechanical behavior of the 3D random fibrous network can be appropriate and efficient.

REFERENCES

- [1] Humphries, D. L., Grogan, J. A., and Gaffney, E. A., The Mechanics of Phantom Mikado Networks, *Journal of Physics Communications*, Vol. 2, No. 5, 2018, pp. 055015.
- [2] Bhadriraju, K., Hansen, L. K., Extracellular Matrix-and Cytoskeleton-Dependent Changes in Cell Shape and Stiffness, *Experimental Cell Research*, Vol. 278, No. 1, 2002, pp. 92-100.
- [3] Lodish, H., Berk, A., Kaiser, C. A., Kaiser, C., Krieger, M., Scott, M. P., and Matsudaira, P., *Molecular Cell Biology*, Macmillan, 2008.
- [4] Hatami-Marbini, H., Etebu, E., Hydration Dependent Biomechanical Properties of The Corneal Stroma, *Experimental Eye Research*, Vol. 116, 2013, pp. 47-54.
- [5] Hatami-Marbini, H., Rohanifar, M., Mechanical Properties of Subisostatic Random Networks Composed of Nonlinear Fibers, *Soft Matter*, Vol. 16, No. 30, 2020, pp. 7156-7164.
- [6] Hatami-Marbini, H., Mofrad, M. R., *Cellular and Biomolecular Mechanics and Mechanobiology*, 2011.
- [7] Reinhart-King, C. A., Dembo, M., and Hammer, D. A., Cell-Cell Mechanical Communication Through Compliant Substrates, *Biophysical Journal*, Vol. 95, No. 12, 2008, pp. 6044-6051.
- [8] Winer, J. P., Oake, S., and Janmey, P. A., Non-Linear Elasticity of Extracellular Matrices Enables Contractile Cells to Communicate Local Position and Orientation, *PloS One*, Vol. 4, No. 7, 2009, pp. e6382.
- [9] Abhilash, A. S., Baker, B. M., Trappmann, B., Chen, C. S., and Shenoy, V. B., Remodeling of Fibrous Extracellular Matrices by Contractile Cells: Predictions From Discrete Fiber Network Simulations, *Biophysical Journal*, Vol. 107, No. 8, 2014, pp. 1829-1840.
- [10] Chen, Y. C., Chen, M., Gaffney, E. A., and Brown, C. P., Effect of Crosslinking in Cartilage-Like Collagen Microstructures, *Journal of the Mechanical Behavior of Biomedical Materials*, Vol. 66, 2017, pp. 138-143.
- [11] MacKintosh, F. C., Käs, J., and Janmey, P. A., Elasticity of Semiflexible Biopolymer Networks, *Physical Review Letters*, Vol. 75, No. 24, 1995, pp. 4425.
- [12] Storm, C., Pastore, J. J., MacKintosh, F. C., Lubensky, T. C., and Janmey, P. A., Nonlinear Elasticity in Biological Gels, *Nature*, Vol. 435, No. 7039, 2005, pp. 191-194.
- [13] Chaudhuri, O., Parekh, S. H., and Fletcher, D. A., Reversible Stress Softening of Actin Networks, *Nature*, Vol. 445, No. 7125, 2007, pp. 295-298.
- [14] Broedersz, C. P., MacKintosh, F. C., Modeling Semiflexible Polymer Networks, *Reviews of Modern Physics*, Vol. 86, No. 3, 2014, pp. 995.
- [15] Meng, F., Terentjev, E. M., Theory of Semiflexible Filaments and Networks, *Polymers*, Vol. 9, No. 2, 2017, pp. 52.
- [16] Hatami-Marbini, H., Picu, C. R., Modeling the Mechanics of Semiflexible Biopolymer Networks: Non-Affine Deformation and Presence of Long-Range Correlations, In *Advances in Soft Matter Mechanics*, Springer, Berlin, Heidelberg, 2012, pp. 119-145.
- [17] Head, D. A., Levine, A. J., and MacKintosh, F. C., Deformation of Cross-Linked Semiflexible Polymer Networks, *Physical Review Letters*, Vol. 91, No. 10, 2003, pp. 108102.

- [18] Rohanifar, M., Hatami-Marbini, H., Numerical Modelling of Mechanical Properties of 2D Cellular Solids with Bi-Modulus Cell Walls, *Mechanics of Advanced Materials and Structures*, Vol. 28, No. 3, 2021, pp. 321-329.
- [19] Sheinman, M., Broedersz, C. P., and MacKintosh, F. C., Nonlinear Effective-Medium Theory of Disordered Spring Networks, *Physical Review E*, Vol.85, No. 2, 2012, pp. 021801.
- [20] Licup, A. J., Sharma, A., and MacKintosh, F. C., Elastic Regimes of Subisostatic Athermal Fiber Networks, *Physical Review E*, Vol. 93, No. 1, 2016, pp. 012407.
- [21] Sharma, A., Licup, A. J., Rens, R., Vahabi, M., Jansen, K. A., Koenderink, G. H., and MacKintosh, F. C., Strain-Driven Criticality Underlies Nonlinear Mechanics of Fibrous Networks, *Physical Review E*, Vol. 94, No. 4, 2016, pp. 042407.
- [22] Licup, A. J., Münster, S., Sharma, A., Sheinman, M., Jawerth, L. M., Fabry, B., and MacKintosh, F. C., Stress Controls the Mechanics of Collagen Networks, *Proceedings of the National Academy of Sciences*, Vol. 112, No. 31, 2015, pp. 9573-9578.
- [23] Jin, T., Stanciulescu, I., Numerical Simulation of Fibrous Biomaterials with Randomly Distributed Fiber Network Structure, *Biomechanics and Modeling in Mechanobiology*, Vol. 15, No. 4, 2016, pp. 817-830.
- [24] Storm, C., Pastore, J. J., Mackintosh, F. C., Lubensky, T. C., Janmey P. A, Nonlinear Elasticity in Biological Gels, *Letters to Nature*, No. 435, 2005, pp. 191-194.
- [25] Gardel, M. L., Shin, J. H., and Weitz, D. A., Elastic Behavior of Cross-Linked and Bundled Actin Networks, *Science*, Vol. 304, 2004, pp. 1301-1305.
- [26] Hatami-Marbini, H., Picu, C. R., Modeling the Mechanics of Semiflexible Biopolymer Networks: Non-Affine Deformation and Presence of Long-Range Correlations, In *Advances in Soft Matter Mechanics*, 1rd ed, Springer, Berlin, Heidelberg, 2012, pp. 119-145.
- [27] Broedersz, C. P., MacKintosh, F. C., Modeling Semiflexible Polymer Networks, *Rev. Mod. Phys*, No. 86, 2014, pp. 995-1036.
- [28] Wilhelm, J., Frey, E., Elasticity of Stiff Polymer Networks, *Phys. Rev. Lett.*, No. 91, Vol. 10, 2003, pp. 108103.
- [29] Head, D. A., Levine, A. J., and MacKintosh, F. C., Deformation of Cross-Linked Semiflexible Polymer Networks, *Phys. Rev. Lett.*, No. 91, Vol. 10, 2003, pp. 108102-1:4.
- [30] Reinhardt, J. W., Gooch, K. J., Agent-Based Modeling Traction Force Mediated Compaction of Cell-Populated Collagen Gels Using Physically Realistic Fibril Mechanics, *J. Biomech. Eng.*, Vol. 136, 2014, pp. 021024:1-9.
- [31] Hatami-Marbini, H., Simulation of the Mechanical Behavior of Random Fiber Networks with Different Microstructure, *Eur Phys J. E. Soft Matter*, Vol. 41, 2018, pp. 1-1: 7
- [32] Hatami-Marbini, H., Scaling Properties of Three-Dimensional Random Fiber Networks, *Philos. Mag. Lett.*, Vol. 96, 2016, pp. 165-174.
- [33] Hatami-Marbini, H., Shriyan, V., Topology Effects on Nonaffine Behavior of Semiflexible Fiber Networks, *Phys. Rev. E.*, Vol. 96, 2017, pp. 062502-1:7.
- [34] Heussinger, C., Frey, E., Floppy Modes and Nonaffine Deformations in Random Fiber Networks, *Phys. Rev. Lett.*, Vol. 97, 2006, pp. 10550-1:4
- [35] Lindström, S. B., Kulachenko, A., Jawerth, L. M., and Vader, D. A., Finite-Strain, Finite-Size Mechanics of Rigidly Cross-Linked Biopolymer Networks, *Soft Matter*, Vol. 9, No. 30, 2013, pp. 7302-7313.
- [36] Broedersz, C. P., Mao, X., Lubensky, T. C., and MacKintosh, F. C., Criticality and Isostaticity in Fiber Networks, *Nature Physics*, Vol. 7, No. 12, 2011, pp. 983-988.
- [37] Yang, L., Van der Werf, K. O., Fitié, C. F., Bennink, M. L., Dijkstra, P. J., and Feijen, J., Mechanical Properties of Native and Cross-Linked Type I Collagen Fibrils, *Biophysical Journal*, Vol. 94, No. 6, 2008, pp. 2204-2211.
- [38] Hatami-Marbini, H., Scaling Properties of Three-Dimensional Random Fiber Networks, *Philosophical Magazine Letters*, Vol. 96, No. 5, 2016, pp. 165-174.
- [39] Piechocka, I. K., Jansen, K. A., Broedersz, C. P., Kurniawan, N. A., MacKintosh, F. C., and Koenderink, G. H., Multi-Scale Strain-Stiffening of Semiflexible Bundle Networks, *Soft Matter*, Vol. 12, No. 7, 2016, pp. 2145-2156.

Bending Optimization of Composite Sandwich Panels with Second-Order Corrugated Cores

Mahdi Shaban *, Sanaz Khoshlesan, Mohammad Sajad Shamsi Monsef

Department of Mechanical Engineering, Faculty of Engineering, Bu-Ali Sina University, Hamedan, Iran

E-mail: m.shaban@basu.ac.ir, mahdishaban22@gmail.com,

s.khoshlesan@alumni.basu.ac.ir, sanaz.khoshlesan@gmail.com,

m.shamsimonsef@alumni.basu.ac.ir, shamsi.sajad785@gmail.com

*Corresponding author

Received: 24 July 2023, Revised: 2 November 2023, Accepted: 10 December 2023

Abstract: Second-order corrugated cores are one type of hierarchical cores that use the common corrugated cores as constituent elements for the main core. This paper attempts to identify and optimize the bending properties of composite sandwich panels with second-order corrugated core. To this end, both first- and second-order corrugated cores are constructed and force-displacement diagrams are extracted in three-point bending tests. Finite element models are created and the deflection results are validated by experiments. Based on the Taguchi method, various finite element models with different geometrical parameters are modeled and reaction force and stiffness are determined. Stiffness formulas for first- and second-order corrugated cores are determined by using regression analysis. The constrained-optimization results are determined to optimize the stiffness of sandwich panels with first- and second-order corrugated cores, separately. The global optimization problem is implemented to compare the first- and second-order configurations.

Keywords: Design of Experiments, Optimization, Sandwich Panel, Second-Order Corrugated Core, Stiffness

Biographical notes: **Mahdi Shaban** received his BSc from Sharif University of Technology in 2007, his MSc from K.N. Toosi University of Technology in 2009, and his PhD degree from Tarbiat Modares University in 2013, all in Mechanical Engineering. In 2014, he joined the Bu-Ali Sina University, Hamedan, where he is currently an Assistant Professor in the field of applied mechanics in the Mechanical Engineering Department. His research interests include advanced materials, smart materials, composite structures, advanced sandwich structures, and Numerical and semi-analytical methods. **Sanaz Khoshlesan** received her MSc in Mechanical Engineering from Bu-Ali Sina University in 2022. Her current research interests are composites, sandwich structure, optimization, corrugated cores, and second-order cores. **Mohammad Sajad Shamsi Monsef** received his BSc and MSc in Mechanical Engineering from Bu-Ali Sina University in 2019, and 2022, respectively. His current research interest includes Composite Structures, sandwich structure, corrugated cores, Finite Element Modeling, Finite Element Analysis, Python Scripting, and Optimization.

Research paper

COPYRIGHTS

© 2024 by the authors. Licensee Islamic Azad University Isfahan Branch. This article is an open access article distributed under the terms and conditions of the Creative Commons Attribution 4.0 International (CC BY 4.0)

<https://creativecommons.org/licenses/by/4.0/>



1 INTRODUCTION

Hierarchical structures are novel structures that have multi-level organization of materials and are widely used in advanced engineering fields such as aerospace, civil, and ocean engineering. These structures have nature-inspired design origins and commonly improve load-bearing capability and crashworthiness compared to traditional structures. Second-order corrugated cores [1] are novel hierarchical cores that use the common corrugated cores as constituent elements for the main core. These structures have the advantages of sandwich panels such as high bending stiffness and low weight at the same time [2].

There are several investigations that studied the mechanical behavior of sandwich panels with corrugated cores. Liang et al. [3] determined the correlation between the transverse displacement of the corrugated panel and external uniform pressure load by implementing normality theory and a simplified beam model. Wang [4] studied the compressive behavior of sandwich panels with multi-layer corrugated linerboards as cushioning media. Bartolozzi et al. [5] present equal properties for sinusoidal corrugated cores based on beam theory and validate them by finite element results. Åslund et al. [6] performed experimental uniaxial compression tests on sandwich panels with corrugated cores to study their buckling. They provided finite element models and validated them with experiments. Berdichevsky and Yu [7] employed asymptotic expansion of the field of the shell theory to determine the equal model for corrugated structures. Kiliçaslan et al [8] exposed multi-layer metal corrugated cores to an axial compression test to determine their energy absorption at different strain rates. They developed a finite element model to extract the stress-strain diagram and compared numerical results with experiments. In the review paper of Dayyani et al. [9], the application of corrugated structures especially in morphing wings is provided.

Blandzi et al. [10] studied sandwich beams with sinusoidal corrugated cores and presented an analytical formulation for bending and buckling them by using the classical Euler–Bernoulli theory. Park et al. [11] used the energy method to determine equal properties for corrugated sheets. In the work done by Kheirikhah and Babaghasabha [12], corrugated sandwich panels with composite faces are modeled and analyzed by using the finite element method. They showed that critical buckling loads increased notably by using corrugated faces. In another work, Kheirikhah et al [13] considered the free vibration of corrugated sandwich panels. Paczos et al. [14] constructed five-layer corrugated beams consisting three corrugated and two facing layers. They determined their vertical displacement by using a three-point bending test. They developed finite element

models and validated numerical results with experiments. Dayyani and Friswell [15] optimized trapezoidal corrugated morphing skins with an elastomeric coating. Han et al. [16] investigated the vibration and buckling of sandwich panels with corrugated cores. They considered that the core is made from composite and filled with foam. They developed shear deformation theory to obtain equal properties of panels. In the work done by Lurie et al. [17], a sandwich panel with a corrugated core is used to design optimum geometry for rescue vehicles in thermal conditions. Shaban and Alibeigloo [18] extended the previous analytical formulation of corrugated cores and determined out-of-plane equal properties of them. They [19] added a piezoelectric sensor and actuator to sandwich panels with corrugated cores to achieve a smart structure.

Du et al. [20] applied three-point bending tests to curved sandwich panels with corrugated cores to determine their failure modes. They also provided analytical formulas for predicting the failure of panels. Zhang et al. [21] studied the failure behavior of sandwich panels with second-order corrugated cores in compression loads. The internal corrugation pattern in their work is similar to the overall pattern. Taghizadeh et al. [22] investigated the effect of corrugated shapes on the energy absorption of sandwich panels with foam-filled corrugated cores. An et al. [23] optimized the stacking sequence of multi-region composite structures by using two-level problems. Fu et al. [24] studied the crush behavior of multilayer corrugated metal tubes subjected to axial impact loads. Zamanifar et al. [25] applied first-order shear deformation theory to the finite strip method to determine the thermal buckling of sandwich panels with the corrugated core. Bahrami-Novin et al. [26] implemented a genetic algorithm for optimizing the geometrical parameters of corrugated sheets.

Yüksel et al. [27] determined a truss model for obtaining equal in-plane stiffness of sandwich panels with corrugated core and filled with foam. Santos et al. [28] optimized Sandwich Panel with a rectangular core by implementing a gradient-based optimization method. They used a plate bending solution to estimate the internal stresses of each layer. Novin et al. [29] determined flexural behavior of sandwich panels with corrugated cores constructed from fiber-metal laminates. They also optimized the structural properties of them. Vakilifard et al. [30] analyzed bending behavior of five-layer sandwich panels with corrugated cores and introduced isotropic multi-layer sandwich panel to eliminate anisotropic properties. In the work of Wang et al. [31], crushing strength analysis of first- and second-order corrugated cores is investigated. Talaie et al. [32] determined out-of-plane core shear modulus for both first- and second-order composite corrugated core. They used first-order shear deformation theory to determine

the deflection equation of the beam subjected to a three-point bending test and compared the analytical results with experimental and numerical results.

Surveying the literature, very few investigations have been found on the investigation of mechanical behavior of sandwich panels with second-order corrugated cores; none of them determine optimized panels. In continuation of the previous work [32], this paper attempts to identify and optimize the bending properties of composite sandwich panels with second-order corrugated core. To this end, the required molds for both first- and second-order corrugated cores are described. Based on the Taguchi method, several finite element models with different geometrical parameters are modeled and reaction force and stiffness are determined. Then, stiffness formulas for first- and second-order corrugated cores are determined by using regression analysis. After that, the constrained-optimization results are determined to optimize the stiffness of sandwich panels with first- and second-order corrugated cores, separately. Finally, the global optimization problem is implemented to compare the first- and second-order configurations.

2 EXPERIMENT MANUFACTURING AND TESTS

2.1. Geometric Characteristics of Sandwich Plates

Figure 1 presents a schematic depiction of sandwich panels with first- and second-order corrugated cores.

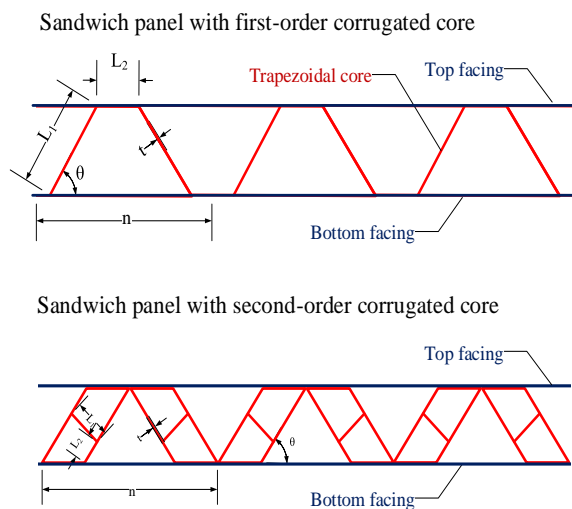


Fig. 11 Schematic representation of sandwich panel with second-order corrugated core.

As shown in “Fig. 1”, the sandwich panel consists of a top facing, bottom facing, and core. The geometrical parameters of corrugated cores are L_1 , L_2 , θ , and n . L_1 and θ are the web length of corrugation and angle of web,

respectively. L_2 denotes the top length of corrugation. n is the unit cell length that represents a full period of trapezoidal corrugation. The thickness of the corrugated core and facings are shown by t and t_c . As shown in “Fig. 1”, the core of the second-order corrugated sandwich panel consists of interior trapezoidal cores. These interior cores rested on the bottom and top facings and created the same angle as the corrugated core, i.e., θ .

2.2. First-Order Sandwich Panel

In this section, the building of a sandwich panel with first-order corrugated core is described. The overall length and width of the panel are 300 mm and 35 mm, respectively. For every component, the E-glass woven is used as fiber. Araldite LY 5052 with Aradur 5052 hardener is used as a resin matrix. For first-order corrugated core, five layers of composites are located in the lower mold. It is noted that the put layer should be impregnated with resin before placing the next layer in the mold. Then, extra fibers out of the mold are cut and the upper mold is placed on the specimen. The trapezoidal corrugated core is exposed to pressure and prepared after the complete curing of the specimen. The constructed specimens have a thickness of 1.25 mm, $L_1=L_2=10$ mm, and $\theta=45^\circ$.

To assemble the facings and core components and obtain a perfect bonding surface between facings and core, the same resin and hardener are used as the adhesive. For achieving a perfect bonding surface between facings and core, the bonded surfaces should be exposed to pressure. But when the corrugated core is subjected to pressure, it deforms and loses its initial form. To overcome this problem, inserts from PVC are provided and used to cause the pressure implemented into the bonding surface without deformation in the shape of a corrugated core. Figures 2(a, b) show how to place inserts into empty cavities of cores. As shown in “Fig. 2(c)”, a reinforced region including internal and external U-cap PVC inserts in both ends is considered to prevent local failures, debonding, and deformations in two ends.

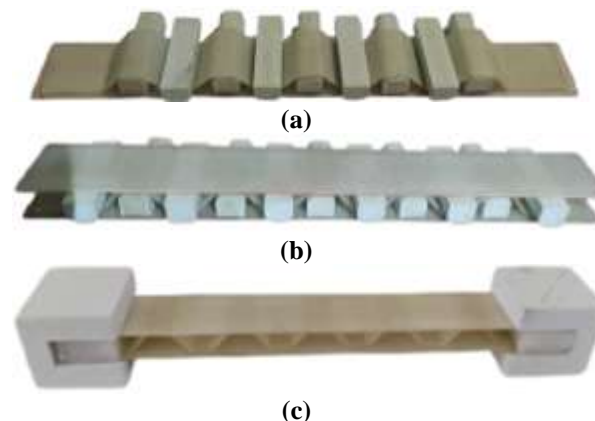


Fig. 2 Manufactured first-order sandwich panels and their inserts.

Based on ASTM D7250, three-point bending tests of the fabricated sandwich panels with first-order corrugated core were conducted in the electronic testing machine SANTAM STM-150 with a loading speed of 0.5 mm/min.

2.3. Second-Order Sandwich Panel

This section describes the manufacturing of sandwich panel with second-order corrugated core. The corrugated parameters are the same as that are used for first-order one. In the first stage, the interior cores should be made. To this end, a couple of molds are provided by using a 3D-printing process. The laminates are positioned in the lower mold and then the upper mold is placed on the laminates. The interior trapezoidal cores are prepared after curing of resin. Figure 3(a) shows the steps of manufacturing interior trapezoidal cores. Next, upper and lower facings should be bonded to trapezoidal cores to provide complete unit cells as shown in “Fig. 3(b)”.

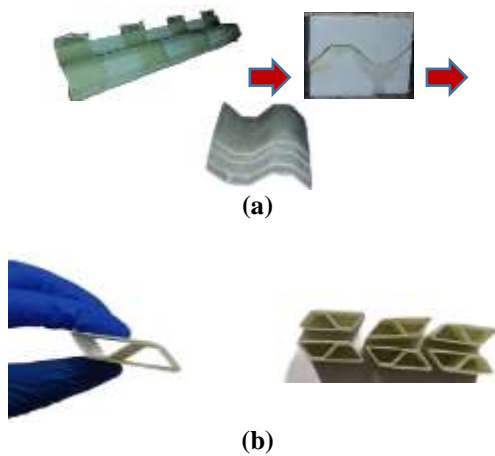


Fig. 3 Interior trapezoidal cores of the second-order corrugated core.

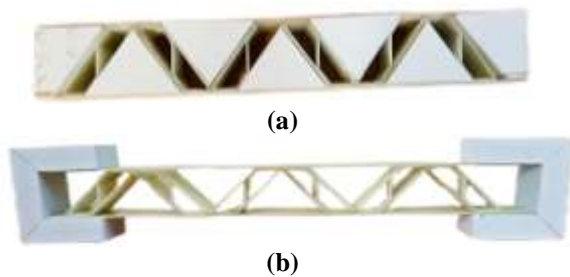


Fig. 4 Manufactured second-order sandwich panels and their inserts.

Similar to first-order corrugated cores, triangle inserts are required to assemble the interior cores as shown in “Fig. 4(a)”. Two outer U-caps are provided to provide local failure of the panel in bending as shown in “Fig. 4(b)”.

3 DESIGNS OF EXPERIMENTS

In this section, empirical formulas are derived for cores shear modulus of first- and second-order corrugated cores based on finite element results that are validated by experiments in previous sections. To investigate the relationship between geometrical parameters of corrugated core, design of experiments (DOE) that is a systematic and effective method is used. Here, Taguchi design method which is one of the famous design methods is used to generate an orthogonal array for four input factors, namely, L1, L2, θ , and t is used. “Table 1” presents the level values of design parameters.

Table 1 Level values of design parameters

Parameters	Parameter symbol	Level values (First-order)	Level values (Second-order)
θ (degree)	A	30,45,60,75	30,45,60,75
t (mm)	B	0.9, 1, 1.1, 1.2	0.9, 1, 1.1, 1.2
L ₂ (mm)	C	10, 20, 40, 60	10, 15
L ₁ (mm)	D	10, 15	10, 15

According to the number of factors and levels, L16 orthogonal array is selected and the FE models are provided. “Table 2 and Table 3” present FE models of first- and second-order corrugated cores.

Table 2 Finite element models of first-order corrugated cores

Experiment number	FEM	Experiment number	FEM
1		9	
2		10	
3		11	
4		12	
5		13	
6		14	
7		15	
8		16	

Three-point bending test is performed in ABAQUS for first- and second-order corrugated sandwich panels. The stiffness of the panel is the slope of the force-displacement diagram and is calculated by dividing the reaction force of the reference point by displacement. The stiffness of first- and second-order corrugated sandwich panels is reported in “Table 4 and Table 5”, respectively.

Table 3 Finite element models of second-order corrugated cores

Experiment number	FEM	Experiment number	FEM
1		9	
2		10	
3		11	
4		12	
5		13	
6		14	
7		15	
8		16	

Table 4 Finite element results of first-order corrugated cores

Expt. No.	α	t	P ₁	P ₂	F (N)	S ^{1st} (N/mm)
1	30	0.9	10	10	25/226	15/288
2	30	1.0	10	20	7/024	4/257
3	30	1.1	15	40	2/26	1/370
4	30	1.2	15	60	1/015	0/615
5	45	0.9	15	20	10/489	6/357
6	45	1.0	15	10	56/279	34/108
7	45	1.1	10	60	1/022	0/619
8	45	1.2	10	40	3/411	2/067
9	60	0.9	10	40	2/443	1/481
10	60	1.0	10	60	1/083	0/656
11	60	1.1	15	10	99/153	60/093
12	60	1.2	15	20	26/179	15/866
13	75	0.9	15	60	0/992	0/601
14	75	1.0	15	40	3/655	2/215
15	75	1.1	10	20	26/404	16/002
16	75	1.2	10	10	16/941	10/267

In the next step, regression analysis is used to generate an equation of force with respect to four design parameters. Regression analysis is carried out in Minitab for multiple orders, namely, linear, quadratic, and cubic polynomial. For each polynomial, the order corresponds with the degree of the equation. In “Table 6”, three statistical parameters are reported, that is, S, R-sq, and R-sq(adj). As shown in this table, the smaller standard error of the regression (S) is for a cubic polynomial that represents that the average distance from the predicted model is little on the other hand, R² or R-sq value together with adjusted R² or R-Sq(adj) value have higher values compared with linear and quadratic models. It means that the design variables, explain up to 94% of the variability of the force. This indicates that the cubic polynomial can suitably predict the reaction force of first- and second-order corrugated cores.

Table 5 Finite element results of second-order corrugated cores

Expt. No.	α	t	P ₁	P ₂	F (N)	S ^{2nd} (N/mm)
1	30	0.9	10	10	4/419	2/946
2	30	1.0	10	10	5/79	3/860
3	30	1.1	15	15	26/67	17/780
4	30	1.2	15	15	29/444	19/629
5	45	0.9	10	15	80/469	53/646
6	45	1.0	10	15	94/424	62/949
7	45	1.1	15	10	81/892	54/595
8	45	1.2	15	10	89/707	59/805
9	60	0.9	15	10	8/416	5/611
10	60	1.0	15	10	3/596	2/397
11	60	1.1	10	15	7/332	4/888
12	60	1.2	10	15	9/436	6/291
13	75	0.9	15	15	6/917	4/611
14	75	1.0	15	15	9/406	6/271
15	75	1.1	10	10	39/898	26/599
16	75	1.2	10	10	50/876	33/917

Table 6 Level values of design parameters

Model	S	R-sq	R-sq(adj)
First-order			
Linear	21.2784	52.47%	35.18%
Quadratic	17.5550	91.18%	55.88%
Cubic	6.06083	99.65%	94.74%
Second-order			
Linear	38.0590	8.97%	0.00%
Quadratic	26.8796	83.49%	38.08%
Cubic	5.50641	99.48%	97.40%

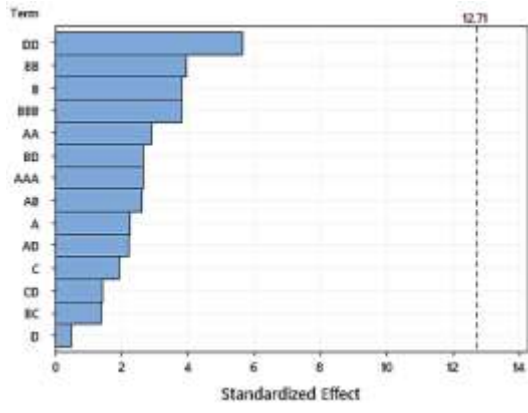
The cubic polynomial for first- and second-order corrugated cores are presented in “Eq. (1) and Eq. (2)”, respectively.

$$\begin{aligned}
 S^{1st} = & 7441.8 - 26.42\alpha - 20377.58t \\
 & + 40.18P_1 + 3.33P_2 \\
 & + 0.64\alpha^2 + 19048.49t^2 \\
 & + 0.034P_1^2 - 12.82\alpha t \\
 & + 0.013\alpha P_2 - 13.273tP_1 \\
 & + 2.885tP_2 - 0.873P_1P_2 \\
 & - 0.003\alpha^3 - 5660t^3
 \end{aligned} \quad (1)$$

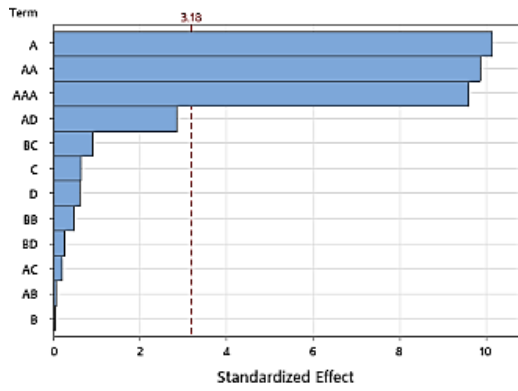
$$\begin{aligned}
 S^{2nd} = & -1215.3 + 73.067\alpha - 8t + 5.667P_1 \\
 & + 4.933P_2 + 1.409\alpha^2 \\
 & + 44.67t^2 + 0.08\alpha t \\
 & + 0.016\alpha P_1 - 0.141\alpha P_2 \\
 & - 6.73tP_1 + 2tP_2 \\
 & + 0.009\alpha^3
 \end{aligned} \quad (2)$$

Figure 5 shows Pareto chart of first- and second-order corrugated cores to determine the magnitude and the importance of the effects. As shown in “Fig 5(a)”, square of the bottom length of the first-order corrugated core,

P2 2, has the most effective term in the formula of the first-order corrugated core. Thickness (either t , t_2 , and t_3) is the second important parameter in bending analysis of the first-order corrugated core. Based on “Fig 5(b)”, the angle of corrugation, α , plays the most important role in the bending of the second-order corrugated core.



(a)



(b)

Fig. 5 Pareto chart of sandwich panels with: (a): first-order corrugated core, and (b): second-order corrugated core.

4 OPTIMIZATIONS

4.1. Constrained-Optimization

In the constrained-optimization problem, the constraints are mass and total length that should be satisfied. For the first-order core, the mass of the constructed specimen is 216.80 gr. In addition, it is assumed that the total length of the sandwich panel is 1m. Four design variables are considered in the optimization problem: α , t , L_1 , and n . To obtain a complete corrugation number, the variable n is considered instead of L_2 . For the first-order core, the parameter L_2 is obtained as follows :

$$L_2 = \frac{L_{total}}{2n} - L_1 \cos(\alpha) \tag{3}$$

The total mass of the first-order core is:

$$m = n \times \rho \times v \tag{4}$$

Where ρ is density and v is the volume of one corrugated core that is calculated as follows:

$$v = 2(L_1 + L_2) \times b \times t \tag{5}$$

For obtaining solution space, the $\pm 1.5\%$ of reference mass tolerance which is about 3.25 gr is considered. The objective function is stiffness, S_{1st} which is obtained from “Eq. (23)”. The stiffness of the reference specimen is 148.48 N/mm. Code scripting in MATLAB software is used to optimize the objective function. “Table 8” presents the optimum parameters of the first-order corrugated core. It can be seen that the stiffness is increased by about 5% compared to the reference specimen. For second-order cores, the parameter L_2 is obtained as follows:

$$L_2 = \left(\frac{L_{total}}{n} - 2L_1 - 2 \right) / 4 \cos(\alpha) - L_1 \cos(\alpha) \tag{6}$$

The volume of one corrugated core is calculated as follows:

$$v = 2 \left[(3L_1 + 2L_2) + (2L_1 \cos(\alpha) + 2L_2) \right] \times b \times t \tag{7}$$

The stiffness of the reference specimen is 107.88 N/mm. The $\pm 1.5\%$ of reference mass tolerance, 329 gr, (about 5.9 gr) is taken into consideration and objective function, S , is obtained from “Eq. (24)”. “Table 7” provides optimum parameters of the second-order corrugated core. It can be concluded that the stiffness is increased by about 24% compared to the reference specimen.

Table 7 Constrained-optimization of first- and second-order corrugated cores

	α	t	P_1	n	S (N/mm)
First-order	74	0.9	14	29	155.85
Second-order	32	1	12	4	134

4.2. Global-Optimization

In this section, the mass is minimized simultaneously to maximize the force. Thus, the objective function is assumed to be S/m . Strictly speaking, in global optimization, mass is not a constraint but is an objective function. “Table 8” presents the results for first- and second-order corrugated cores. As shown in this table, F/m in the second-order corrugated core is about twice of first-order one.

Table 8 Global-optimization of first- and second-order corrugated cores

	α	t	P_l	n	S/m
First-order					
	30	0.9	60	14	13.13
Second-order					
	74	0.9	52	14	28.64

5 CONCLUSIONS

The optimization of the bending behavior of sandwich panels with first- and second-order corrugated composite cores is investigated. For experimental specimens, a couple of molds are provided by using a 3D-printing process, and the corrugated cores are manufactured and then assembled to create sandwich panels. After selecting design parameters, the Taguchi method is used for the design of experiments. Based on Taguchi method results, finite element models are provided and the correspondent stiffness is extracted. The regression analysis is used to generate an equation of stiffness with respect to design parameters and the best stiffness formulas are selected.

In the next step, a constrained optimization problem is considered and the stiffness of sandwich panels is optimized. To compare the first- and second-order configuration, global optimization is considered by considering both the stiffness and mass of the panel and optimized parameters are determined. It is concluded that:

- The geometrical parameters do not have the same effect on the bending behavior of sandwich panels with first- and second-order corrugated cores. As shown, the corrugation angle is the most determinant factor in bending behavior of sandwich panels with second-order corrugated cores. On the other hand, the bottom length of first-order corrugated core is the most determinant factor in bending behavior.

- The influence of geometrical parameters in the increase of stiffness for sandwich panels with second-order corrugated cores is more notable compared with first-order one. In the considered constrained optimization, more improvement can be observed for the stiffness of the sandwich panel with a second-order corrugated core compared to the sandwich panel with a first-order corrugated one.

- By considering both the stiffness and mass of sandwich panels, it is determined that the sandwich panel with a second-order corrugated core has higher (more than twice) stiffness per unit mass than the sandwich panel with a first-order one. This means that sandwich panels with second-order corrugated cores are preferred candidates in structures that should endure high bending loads.

AUTHORS' CONTRIBUTIONS

Conceptualization, M. Sh; Methodology, M. Sh; experiments, software and validation, S. Kh and M.S. Sh.

REFERENCES

- [1] Kooistra, G. W. Deshpande, V. S. and Wadley, H. N. G., Compressive Behavior of Age Hardenable Tetrahedral Lattice Truss Structures Made from Aluminium, *Acta Mater.*, Vol. 52, No. 14, 2004, pp. 4229–4237, doi: 10.1016/j.actamat.2004.05.039.
- [2] Nuño, M., Bühring, J., Rao, M. N., and Schröder, K. U., Delamination Testing of AlSi10Mg Sandwich Structures with Pyramidal Lattice Truss Core made by Laser Powder Bed Fusion, *Chinese J. Mech. Eng. English Ed.*, Vol. 34, No. 1, 2021, doi: 10.1186/s10033-021-00643-7.
- [3] Liang, Y. H., Louca, L. A., and Hobbs, R. E., A Simplified Method in The Static Plastic Analysis of Corrugated Steel Panels, *J. Strain Anal. Eng. Des.*, Vol. 41, No. 2, 2006, pp. 135–149, doi: 10.1243/030932405x30948.
- [4] Wang, D., Cushioning Properties of Multi-Layer Corrugated Sandwich Structures, *J. Sandw. Struct. Mater.*, Vol. 11, No. 1, 2009, pp. 57–66, doi: 10.1177/1099636208100415.
- [5] Bartolozzi, G., Pierini, M., Orrenius, U., and Baldanzini, N., An Equivalent Material Formulation for Sinusoidal Corrugated Cores of Structural Sandwich Panels, *Compos. Struct.*, Vol. 100, 2013, pp. 173–185, doi: 10.1016/j.compstruct.2012.12.042.
- [6] Åslund, P. E., Hägglund, R., Carlsson, L. A., and Isaksson, P., Modeling of Global and Local Buckling of Corrugated Board Panels Loaded in Edge-To-Edge Compression, *J. Sandw. Struct. Mater.*, Vol. 16, No. 3, 2014, pp. 272–292, doi: 10.1177/1099636213519374.
- [7] Ye, Z., Berdichevsky, V. L., and Yu, W., An Equivalent Classical Plate Model of Corrugated Structures, *Int. J. Solids Struct.*, Vol. 51, No. 11–12, 2014, pp. 2073–2083, doi: 10.1016/j.ijsolstr.2014.02.025.
- [8] Kiliçaslan, C., Güden, M., Odaci, I. K., and Taşdemirci, A., Experimental and Numerical Studies on The Quasi-Static and Dynamic Crushing Responses of Multi-Layer Trapezoidal Aluminum Corrugated Sandwiches, *Thin-Walled Struct.*, Vol. 78, 2014, pp. 70–78, doi: 10.1016/j.tws.2014.01.017.
- [9] Dayyani, I., Shaw, A. D., Saavedra Flores, E. I., and Friswell, M. I., The Mechanics of Composite Corrugated Structures: A Review with Applications in Morphing Aircraft, *Compos. Struct.*, Vol. 133, 2015, pp. 358–380, doi: 10.1016/j.compstruct.2015.07.099.
- [10] Magnucka-Blandzi, E., Magnucki, K., and Wittenbeck, L., Mathematical Modeling of Shearing Effect for Sandwich Beams with Sinusoidal Corrugated Cores,

- Appl. Math. Model., Vol. 39, No. 9, 2015, pp. 2796–2808, doi: 10.1016/j.apm.2014.10.069.
- [11] Park, K. J., Jung, K., and Kim, Y. W., Evaluation of Homogenized Effective Properties for Corrugated Composite Panels, *Compos. Struct.*, Vol. 140, 2016, pp. 644–654, doi: 10.1016/j.compstruct.2016.01.002.
- [12] Kheirikhah, M. M., Babaghasabha, V., Bending and Buckling Analysis of Corrugated Composite Sandwich Plates, *J. Brazilian Soc. Mech. Sci. Eng.*, Vol. 38, No. 8, 2016, pp. 2571–2588, doi: 10.1007/s40430-016-0498-6.
- [13] Kheirikhah, M. M., Babaghasabha, V., Naeimi-Abkenari, A., and Khadem, M., Free Vibration Analysis of Corrugated-Face Sheet Composite Sandwich Plates, *J. Brazilian Soc. Mech. Sci. Eng.*, Vol. 38, No. 7, 2016, pp. 1973–1985, doi: 10.1007/s40430-015-0306-8.
- [14] Paczos, P., Wasilewicz, P., and Magnucka-blandzi, E., Experimental and Numerical Investigations of Five-Layered Trapezoidal Beams, *Compos. Struct.*, Vol. 145, 2016, pp. 129–141, doi: 10.1016/j.compstruct.2016.02.079.
- [15] Dayyani, I., Friswell, M. I., Multi-Objective Optimization for The Geometry of Trapezoidal Corrugated Morphing Skins, *Struct. Multidiscip. Optim.*, Vol. 55, No. 1, 2017, pp. 331–345, doi: 10.1007/s00158-016-1476-4.
- [16] Han, B., Qin, K. K., Zhang, Q. C., Zhang, Q., Lu, T. J., and Lu, B. H., Free Vibration and Buckling of Foam-Filled Composite Corrugated Sandwich Plates Under Thermal Loading, *Compos. Struct.*, Vol. 172, 2017, pp. 173–189, doi: 10.1016/j.compstruct.2017.03.051.
- [17] Lurie, S. A., Solyaev, Y. O., Volkov-Bogorodskiy, D. B., Bouznik, V. M., and Koshurina, A. A., Design of the Corrugated-Core Sandwich Panel for The Arctic Rescue Vehicle, *Compos. Struct.*, Vol. 160, 2017, pp. 1007–1019, doi: 10.1016/j.compstruct.2016.10.123.
- [18] Shaban, M., Alibeigloo, A., Three-Dimensional Elasticity Solution for Sandwich Panels with Corrugated Cores by Using Energy Method, *Thin-Walled Struct.*, Vol. 119, 2017, pp. 404–411, doi: dx.doi.org/10.1016/j.tws.2017.06.035.
- [19] Shaban, M., Alibeigloo, A., Global Bending Analysis of Corrugated Sandwich Panels with Integrated Piezoelectric Layers, *Journal of Sandwich Structures and Materials*, 2018.
- [20] Du, B., et al., Fabrication and Bending Behavior of Thermoplastic Composite Curved Corrugated Sandwich Beam with Interface Enhancement, *Int. J. Mech. Sci.*, Vol. 149, No. October, 2018, pp. 101–111, doi: 10.1016/j.ijmecsci.2018.09.049.
- [21] Zhang, J., Ye, Y., Zhu, Y., Qin, Q., and Wang, T. J., Dynamic Collapse of Metal Self-Similar Hierarchical Corrugated Sandwich Plates, *Acta Mech.*, Vol. 230, No. 5, 2019, pp. 1549–1563, doi: 10.1007/s00707-018-2342-9.
- [22] Taghizadeh, S. A., et al., Characterization of Compressive Behavior of Pvc Foam Infilled Composite Sandwich Panels with Different Corrugated Core Shapes, *Thin-Walled Struct.*, Vol. 135, No. October, 2018, pp. 160–172, 2019, doi: 10.1016/j.tws.2018.11.019.
- [23] An, H., Chen, S., and Huang, H., Stacking Sequence Optimization and Blending Design of Laminated Composite Structures, *Struct. Multidiscip. Optim.*, Vol. 59, No. 1, 2019, pp. 1–19, doi: 10.1007/s00158-018-2158-1.
- [24] Fu, B., Liao, C., Xie, L., Li, Z., and Shu, R., A Theoretical Analysis on Crush Characteristics of Corrugated Tube Under Axial Impact and Experimental Verification, *J. Brazilian Soc. Mech. Sci. Eng.*, Vol. 42, No. 10, 2020, doi: 10.1007/s40430-020-02593-y.
- [25] Zamanifar, H., Sarrami-Foroushani, S., and Azhari, M., A Parametric Study on The Mechanical and Thermal Stability of Corrugated-Core Sandwich Plates, *Structures*, Vol. 24, No. January, 2020, pp. 209–226, doi: 10.1016/j.istruc.2020.01.015.
- [26] Bahrami-Novin, N., Mahdavi, E., Shaban, M., and Mazaheri, H., Multi-Objective Optimization of Tensile Properties of The Corrugated Composite Sheet, *J. Compos. Mater.*, Vol. 56, No. 5, 2021, pp. 811–821, doi: 10.1177/00219983211059580.
- [27] Yüksel, E., et al., Experimental Investigation and Pseudoelastic Truss Model for In-Plane Behavior of Corrugated Sandwich Panels with Polyurethane Foam Core, *Structures*, Vol. 29, 2021, pp. 823–842, doi: https://doi.org/10.1016/j.istruc.2020.11.058.
- [28] Santos, L., Izzuddin, B. A., and Macorini, L., Gradient-Based Optimisation of Rectangular Honeycomb Core Sandwich Panels, *Struct. Multidiscip. Optim.*, Vol. 65, No. 9, 2022, pp. 1–18, doi: 10.1007/s00158-022-03341-7.
- [29] Novin, N. B., Shaban, M., and Mazaheri, H., Flexural Response of Fiber - Metal Laminate Face - Sheet / Corrugated Core Sandwich Beams, *J. Brazilian Soc. Mech. Sci. Eng.*, 2022, doi: 10.1007/s40430-022-03492-0.
- [30] Vakilifard, V., Mazaheri, H., and Shaban, M., Bending Behavior and Geometrical Optimization of Five-Layered Corrugated Sandwich Panels with Equal In-Plane Principal Stiffness, *J. Compos. Mater.*, Vol. 56, No. 17, 2022, pp. 2739–2753, doi: 10.1177/00219983221082236.
- [31] Wang, H., Guo, Y., Fu, Y., and Li, D., Out-of-Plane Static Compression and Energy Absorption of Paper Hierarchical Corrugation Sandwich Panels, *J. Strain Anal. Eng. Des.*, vVol. 57, No. 2, 2022, pp. 132–143, doi: 10.1177/03093247211008566.
- [32] Talaie, P., Shaban, M., and Khoshlesan, S., Flexural Analysis of Second-Order Corrugated Composite Cores: Experimental, Numerical, And Theoretical Studies, *J. Strain Anal. Eng. Des.*, 2023

Numerical Analysis of Time Dependent Temperature Distribution inside a Solar Greenhouse

Mahya Mohammadi*

Department of Mechanical Engineering,
K. N. Toosi University of Technology, Tehran, Iran
University of Waterloo, Waterloo, Ontario, Canada
E-mail: mahya.mohammadi@email.kntu.ac.ir
*Corresponding author

Cyrus Aghanajafi

Department of Mechanical Engineering,
K. N. Toosi University of Technology, Tehran,
E-mail: aghanajafi@kntu.ac.ir

Received: 23 January 2020, Revised: 4 June 2020, Accepted: 14 July 2020

Abstract: In the present study, a numerical model is developed to predict time-dependent temperature variations inside a solar greenhouse by solving the continuity, Navier-Stokes, and energy Equations using ANSYS Fluent. This paper considers all heat transfer mechanisms into and out of the greenhouse, including convection, radiation, and conduction. The surface-to-surface model and SIMPLE method are employed to analyse thermal radiation between surfaces within the greenhouse and to couple pressure and velocity in solving the flow-field Equations numerically, respectively. This study specifically investigates the unsteady temperature distribution within a solar greenhouse located in Makran, Iran (latitude: 25.3054°N, longitude: 60.6411°E). The numerical method of this study is validated by comparing its results with experimental data. The high accuracy demonstrated by this approach supports the conclusion that the model can effectively study the flow field and thermal behaviour inside solar greenhouses. It is demonstrated that fluctuating boundary conditions cause the thermal conditions inside the greenhouse to vary dynamically over time. The results depict the spatial variation of temperature distribution at different levels from the soil surface at 13:00 on the first and second days of modelling in Makran. These insights are expected to play a crucial role in improving greenhouse design and management practices in agriculture.

Keywords: Heat Transfer, Iran, Makran, Numerical Model, Surface-To-Surface Model, Solar Greenhouse, Time-Dependent Temperature Variations

Biographical notes: **Mahya Mohammadi** received her PhD in Mechanical Engineering from K. N. Toosi University of Technology in 2022. She completed a visiting period at the University of Waterloo, Canada. Currently, Her research interests focus on fluid mechanics and transfer phenomena, particularly their applications in cancer treatment modeling. **Cyrus Aghanajafi** is a Full Professor at K. N. Toosi University of Technology. He received his PhD in Mechanical Engineering from Tennessee State University, USA. His current research focuses on fluid mechanics, heat transfer, and thermodynamics.

Research paper

COPYRIGHTS

© 2024 by the authors. Licensee Islamic Azad University Isfahan Branch. This article is an open access article distributed under the terms and conditions of the Creative Commons Attribution 4.0 International (CC BY 4.0)

(<https://creativecommons.org/licenses/by/4.0/>)



1 INTRODUCTION

Solar greenhouses are typically defined as enclosures that provide an appropriate environment to grow crops such as plants, flowers, and vegetables [1]. The solar greenhouse industry effectively uses renewable solar energy. There are two types of solar greenhouses: passive and active. In passive solar greenhouses, solar energy is used to heat water, concrete, or other heat-holding materials, with minimal human involvement in the self-regulated warming process [2]. The active system, however, requires electricity or another conventional source of energy [3].

Experimental studies of greenhouses are too expensive, and their results are only useful for specific conditions and geometry. Therefore, numerical models are needed to predict the temperature distribution inside greenhouses. Computational Fluid Dynamics (CFD) is a powerful tool to simulate the climatic conditions within greenhouses [4]. Okushima et al. [5] studied ventilation in greenhouses using CFD for the first time. They compared the results of the numerical method with experimental data [6]. This technique was not used for some time until Bot et al. [7] compared the CFD results of a two-span greenhouse simulation with data obtained by means of sonic anemometry.

CFD has been increasingly used in simulating greenhouse climatic conditions. Bartzanas et al. [8] studied the effect of an insect-proof screen (located in the side openings of a tunnel greenhouse) on airflow and temperature distribution using CFD. They found that airflow was reduced and the thermal gradient increased by using the insect screen. Molina-Aiz et al. [9] studied the effect of wind speed on the inner climatic conditions of the greenhouse using finite element method-based software. The continuity, momentum, energy, turbulent kinetic energy, and dissipation rate Equations were solved. They found that ventilation was a significant parameter affecting crop growth. Tong et al. [10] predicted the temperature distribution inside a Chinese solar greenhouse during three clear days followed by a cloudy day using the CFD method. Radiation, convection, and conduction heat transfer were all assumed in their study to present an accurate prediction. Rodriguez and Velazquez [11] demonstrated the capability of CFD in predicting climate control in a solar greenhouse, considering heat and mass transfer.

A system of Equations for heat and moisture transfer during the drying of copra in a solar greenhouse dryer was numerically solved using the finite difference method by Sadodin and Kashani [12]. Based on the results, it was concluded that this type of dryer can be used in rural areas without electricity grids, with an estimated payback period of about 2.3 years. Lokeswaran and Eswaramoorthy [13] validated their experimental results on natural convection in a solar

greenhouse dryer using Fluent software. They solved the continuity, momentum, and energy Equations simultaneously using the SIMPLE scheme for pressure-velocity coupling.

Deiana et al. [14] investigated the effect of different building materials on the internal temperature of Chinese solar greenhouses throughout the entire cold season, using numerical methods. Chen et al. [15] studied the contribution of an active-passive ventilation wall with phase change material (PCM) in improving the north wall of a solar greenhouse, both numerically and experimentally. They demonstrated the effectiveness of the proposed wall by monitoring the increase in indoor air temperature, daily effective accumulative temperature, and soil temperature.

Tong and Christopher [16] investigated the effect of different parameters on the inner temperature distribution in a Chinese solar greenhouse through sensitivity analysis. He et al. [17] simulated a 2D model of a solar greenhouse using FLUENT to determine the best size for the back wall vent. The discrete ordinates radiation model was used to calculate coupled radiation and convective exchanges. They found that vents were the key factor affecting the greenhouse temperature distribution. Esmaeli and Roshandel [18] optimized the structural properties of a solar greenhouse based on a thermal model to minimize the deviation of the temperature from the suitable temperature range. They found that the optimized parameters are depended on the objective function, varying from year-round performance to seasonal or cultivation period performances.

In this study, a sophisticated numerical model is developed to simulate the climatic conditions within a solar greenhouse, with a specific focus on the thermal behaviour of a greenhouse located in Makran, Iran. This analysis is crucial for optimizing agricultural practices in the region. The model incorporates time-dependent boundary conditions, including solar insolation, sky temperature, outside air temperature, and outside air relative humidity. These parameters are accurately determined and implemented in the simulation software using a user-defined function (UDF) to ensure the precision of the numerical model. The research methodology includes a rigorous validation process, where the model's predictions are compared against experimental data to verify its accuracy. Another significant contribution of this research is providing detailed insights into the temperature distribution within the solar greenhouse in Makran, Iran.

2 MATERIALS AND METHODS

In the current study, a numerical model is employed to simulate the temperature distribution inside a solar

greenhouse. The model's geometry, computational domain, governing Equations, boundary conditions (BCs), effective properties of the layered surfaces, and numerical solution procedure are discussed in the following subsections.

2.1. Model Geometry and Computational Domain

Figure 1 shows the cross-sectional view of the greenhouse. The soil depth under the greenhouse is assumed to be 1.0 m. The greenhouse is modeled as two-dimensional.

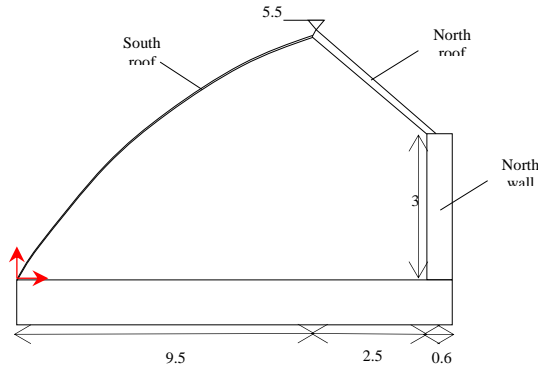


Fig. 1 Cross-sectional view of the greenhouse with dimensions [m].

2.2. Governing Equations

The system is simulated by discretizing space and time using the finite-volume method and solving the incompressible, unsteady, two-dimensional laminar conservation Equations for the velocity and temperature fields on an unstructured grid. The continuity, Navier-Stokes, and energy Equations are represented as [19]:

$$\frac{\partial U_i}{\partial x_i} = 0 \quad (1)$$

$$\rho \frac{\partial U_i}{\partial t} + \rho U_j \frac{\partial U_i}{\partial x_j} = -\frac{\partial p}{\partial x_i} + \frac{\partial}{\partial x_j} (2\mu S_{ji}) + \rho f_i \quad (2)$$

$$\rho \frac{\partial u}{\partial t} + \rho U_i \frac{\partial u}{\partial x_i} = -p \frac{\partial U_j}{\partial x_j} + \frac{\partial}{\partial x_j} (k \frac{\partial T}{\partial x_j} - q_r) + \Phi + Q \quad (3)$$

The vectors U_i and x_i are velocity and position, T is temperature, p is pressure, ρ is density, μ is molecular viscosity, f_i is body force per unit mass, u is the internal energy per unit mass (the most frequent form of u is $u = c_d T$ for liquids and $u = c_v dT$ for gases where c_v is the specific heat at constant volume), k is thermal conductivity, Q is the heat source or sink, q_r is radiation term, Φ is dissipation rate, and S_{ji} is the strain

rate tensor that can be written as follows [19]:

$$S_{ji} = \frac{1}{2} \left(\frac{\partial U_i}{\partial x_j} + \frac{\partial U_j}{\partial x_i} \right) \quad (4)$$

2.2.1. Solar Radiation Model

Solar radiation is a crucial factor influencing the indoor temperature and airflow distribution in a greenhouse. It is assumed that air does not participate in thermal radiation exchange. Thermal radiation heat transfer between surfaces inside the greenhouse is calculated using the Surface-to-Surface (S2S) model. This model can be used to account for radiation exchange in an enclosure with gray-diffuse surfaces. The energy exchange between two surfaces depends in part on their size, separation distance, and orientation. These parameters are accounted for by a geometric function called a view factor. The main assumption of the S2S model is that any absorption, emission, or scattering of radiation can be ignored; therefore, only surface-to-surface radiation needs to be considered for analysis [20].

The energy flux leaving a particular surface consists of emitted and reflected components. The amount of reflected energy flux depends on the incident energy flux from the surroundings, which can be described in relation to the energy flux from all other surfaces. The energy reflected from surface k is [21]:

$$q_{out,k} = \varepsilon_k \sigma T_k^4 + \rho_k q_{in,k} \quad (5)$$

Where $q_{out,k}$, ε_k , σ , ρ_k , and $q_{in,k}$ are energy flux leaving the surface, emissivity, Boltzmann's constant, transmissivity, and energy flux incident on the surface from the surroundings, respectively. The incident energy on a surface from another surface is directly determined by the surface-to-surface view factor, F_{jk} . The view factor F_{jk} represents the fraction of energy leaving surface k that reaches surface j .

The incident energy flux $q_{in,k}$ can be expressed in relation to the energy flux leaving all other surfaces as follows [21]:

$$A_k q_{in,k} = \sum_{j=1}^N A_j q_{out,j} F_{jk} \quad (6)$$

Where A_k is the area of surface k and F_{jk} is the view factor between surface k and surface j . For N surfaces, applying the view factor reciprocity relationship yields [20]:

$$A_j F_{jk} = A_k F_{kj} \text{ for } j = 1, 2, 3, \dots, N \quad (7)$$

So that:

$$q_{in,k} = \sum_{j=1}^N F_{kj} q_{out,j} \quad (8)$$

Therefore:

$$q_{out,k} = \varepsilon_k \sigma T_k^4 + \rho_k \sum_{j=1}^N F_{kj} q_{out,j} \quad (9)$$

Which can be written as [21]:

$$J_k = E_k + \rho_k \sum_{j=1}^N F_{kj} J_j \quad (10)$$

Where J_k represents the radiosity (energy given off) of surface k , and E_k represents the emissive power of surface k . This forms N Equations, which can be reformulated into matrix form as follows [20]:

$$KJ = E \quad (11)$$

Where K is a $N \times N$ matrix, J is the radiosity vector, and E is the emissive power vector. Equation (11) is referred to as the radiosity matrix Equation. The view factor between two finite surfaces i and j is defined as [20]:

$$F_{ij} = \frac{1}{A_i} \int_{A_i} \int_{A_j} \frac{\cos \theta_i \cos \theta_j}{\pi r^2} \delta_{ij} dA_i dA_j \quad (12)$$

Where δ_{ij} is evaluated by the visibility of dA_j to dA_i . $\delta_{ij} = 1$ if dA_j is visible to dA_i and 0 otherwise.

2.3. BCS and Effective Properties of The Layered Surfaces

The thermal radiation heat transfer between the inner surfaces, as well as between the outside surfaces and the sky, is considered due to the temperature difference. The S2S model is applied to calculate the radiation heat transfer between surfaces inside the greenhouse. Natural convection inside the greenhouse, convection between the outside air and the greenhouse surfaces, condensation on the cover, and air filtration are all considered.

The sky temperature is calculated as [22]:

$$T_{sky} = \varepsilon_{sky}^{0.25} (T_{ao} + 273) \quad (13)$$

$$\varepsilon_{sky} = 0.74 + 0.006T_{dp} \quad (14)$$

Where T_{ao} is the outside temperature, ε_{sky} is the sky

emissivity. The dew point temperature, T_{dp} , is a function of the relative humidity and the outside air temperature, and an empirical relationship is used [23]:

$$T_{dp} = (112 + 0.9T_{ao})RH^{0.125} + (0.1T_{ao} - 112) \quad (15)$$

RH is the relative humidity outside the greenhouse. T_{ao} is in $^{\circ}C$ in “Eq. (15)”. The air temperature and relative humidity outside the greenhouse used in this study are shown in “Figs. 2 and 3”.

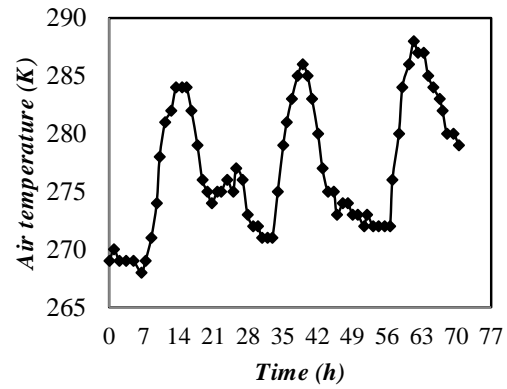


Fig. 2 Air temperature outside [10].

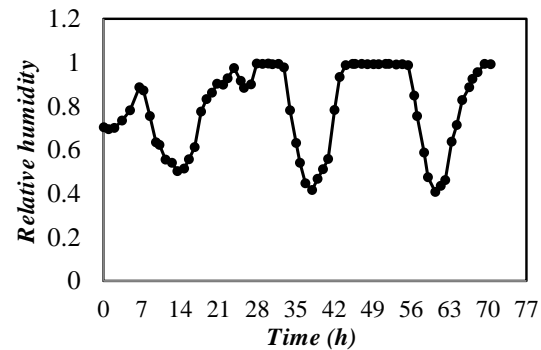


Fig. 3 Air relative humidity [10].

The solar radiation reaching the inner surfaces includes both beam solar radiation and diffuse solar radiation. The beam solar radiation fluxes on the inner surfaces are specified by [10]:

$$q_{b,ground} = q_b \tau_b \quad (16)$$

$$q_{b,northwall} = \frac{\cos \theta_w}{\cos \theta_z} q_{b,ground} \quad (17)$$

$$q_{b,northroof} = \frac{\cos \theta_r}{\cos \theta_z} q_{b,ground} \quad (18)$$

Where q_b is the solar beam radiation flux on a horizontal

surface outside in w/m^2 , depicted in “Fig. 4”. τ_b , θ_z , θ_w and θ_r represent the south roof cover film transmittance for beam radiation, angles of incidence on the horizontal (soil), north wall, and north roof surfaces, respectively. The view factors required for calculating the diffuse solar radiation on the inner surfaces are provided in [10]:

$$\eta_{ab,bc} = \frac{l_{ab} + l_{bc} - l_{ac}}{2l_{ab}} \quad (19)$$

$$\eta_{ab,ad} = \frac{l_{ab} + l_{ad} - l_{bd}}{2l_{ab}} \quad (20)$$

$$\eta_{ab,cd} = \frac{l_{bd} + l_{ac} - l_{bc} - l_{ad}}{2l_{ab}} \quad (21)$$

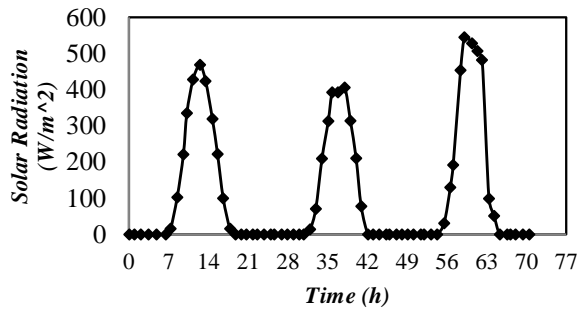


Fig. 4 Total solar radiation outside on a horizontal surface [10].

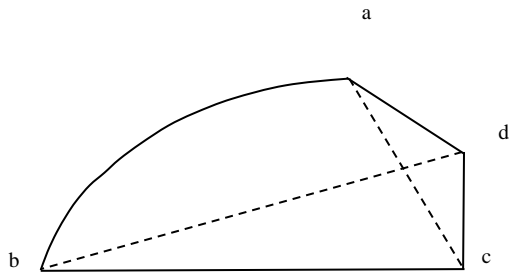


Fig. 5 Scheme of the surface view factor [10].

Figure 5 shows the scheme of the surface view factors. The calculation of diffuse solar radiation fluxes to the inner surfaces is described in [10]:

$$q_{d,ground} = q_{d,southroof} \tau_d \eta_{ab,bc} \quad (22)$$

$$q_{d,northwall} = q_{d,southroof} \tau_d \eta_{ab,cd} \quad (23)$$

$$q_{d,northroof} = q_{d,southroof} \tau_d \eta_{ab,ad} \quad (24)$$

Where $q_{d,southroof}$ is the diffuse radiation flux to the south roof surface in w/m^2 . τ_d is the south roof cover film transmittance for diffuse radiation. The diffuse radiation flux on a horizontal surface is assumed to be 20% of the total solar radiation [10].

The solar radiation flux incident on the south roof can be calculated as [24]:

$$q_{sf,o} = R_b q_b + R_d q_d + R_{re} (q_b + q_d) \quad (25)$$

Where $q_{sf,o}$ is the total solar radiation flux outside the south roof in w/m^2 . q_b , q_d , R_b , R_d , and R_{re} represent beam radiation, diffuse radiation, the ratio of the beam radiation incident flux on the south roof to that on the horizontal surface, the ratio of the diffuse radiation incident flux on the south roof to that on the horizontal surface, and the reflected component, respectively. R_b , R_d , and R_{re} can be calculated as [24]:

$$R_b = \frac{\cos \theta_{sf}}{\cos \theta_z} \quad (26)$$

$$R_d = \frac{1 + \cos \beta}{2} \quad (27)$$

$$R_{re} = \alpha \left(\frac{1 - \cos \beta}{2} \right) \quad (28)$$

Where θ_{sf} , θ_z , β , and α represent the angles of incidence relative to the south roof, the angles of incidence relative to the horizontal surface, the angle between the south roof plane and the horizontal plane, and the reflection coefficient of the ground, respectively. According to “Fig. 6”, the incidence angle of the sloped plane is determined as [25]:

$$\cos \theta = \sin \delta \sin \phi \cos \beta - \sin \delta \cos \phi \sin \beta \cos \gamma + \cos \delta \cos \phi \cos \beta \cos \omega + \cos \delta \sin \phi \sin \beta \cos \gamma \cos \omega + \cos \delta \sin \beta \sin \gamma \sin \omega \quad (29)$$

Where δ , ϕ , γ , and ω are declination, latitude, solar azimuth, and hour angel, respectively. Declination is determined by using “Fig. 7”. ω and γ can be calculated as [25]:

$$\omega = 15^\circ (\text{Solartime} - 12) \quad (30)$$

$$\text{Solar time} = \frac{\text{Standard time} + 4(\text{local solar time} - \text{longitude}) + E}{60} \quad (31)$$

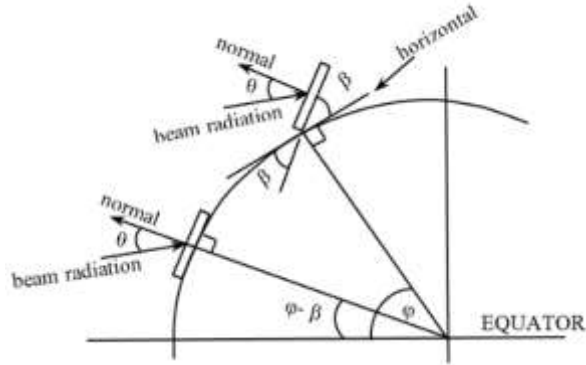


Fig. 6 Section of earth showing, redrawn from [25].

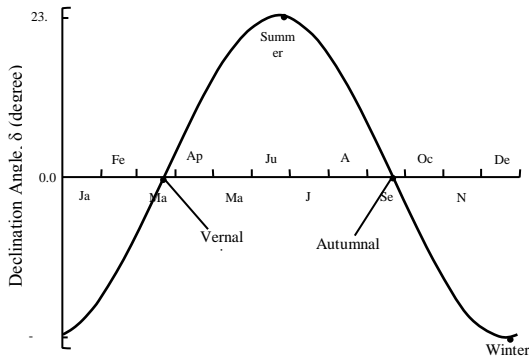


Fig. 7 Variation of the declination angle, redrawn from [26].

$$E = 229.2(0.000075 + 0.001868 \cos B - .032077 \sin B - .014615 \cos 2B - .04089 \sin 2B) \quad (32)$$

$$B = \frac{(n-1)360}{365} \quad (33)$$

Where n is the number of days since the start of the year.

$$\gamma = \sin(\omega) \left| \cos^{-1} \left(\frac{\cos \theta_z \sin \phi - \sin \delta}{\sin \theta_z \cos \phi} \right) \right| \quad (34)$$

Condensation occurred on the inside south roof surface during a certain time range [10]. The latent heat flux (W/m^2) due to condensation, as given by Garzoli [27], is:

$$q_{\text{condensation}} = \frac{h_c L (w_a - w_c)}{c_p} \quad (35)$$

Where h_c is the inside surface heat transfer coefficient, $7.2 (W/m^2K)$ [28]. c_p is the specific heat of air (J/kgK), L is the latent heat of vaporization (J/kg), and w_a and w_c are the humidity ratio in the greenhouse air and the humidity ratio of air saturated at the cover temperature, respectively, with [10]:

$$w_a = \frac{RH}{100} (0.004055 + 0.0001152t_a + 0.00002167t_a^2) \quad (36)$$

$$w_c = 0.004055 + 0.0001152t_c + 0.00002167t_c^2 \quad (37)$$

Where RH is the relative humidity of the greenhouse air, t_a is the greenhouse air temperature in $^{\circ}C$ and, t_c is the cover temperature in $^{\circ}C$.

The total leakage heat losses due to air infiltration are the sum of the sensible and latent leakage losses [29]:

$$q_{\text{inf},s} = \frac{NV\rho c_p \Delta T}{A_{\text{enclosure}}} \quad (38)$$

$$q_{\text{inf},l} = \frac{NV\rho L \Delta \omega}{A_{\text{enclosure}}} \quad (39)$$

Where V , ρ , ΔT , and $\Delta \omega$ represent the volume, air density, air temperature difference between the inside and outside of the greenhouse ($10K$), and air humidity ratio difference between the inside and the outside of the greenhouse, respectively.

The actual physical properties of the layered structures used in this study are listed in “Table 1”.

2.4. Numerical Solution Procedure

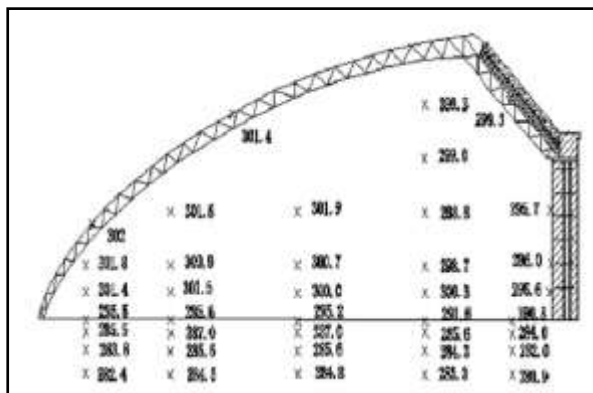
The geometry is created and the grid is generated with the aid of GAMBIT software. The governing Equations are solved numerically using ANSYS FLUENT 14. The unsteady boundary conditions of the greenhouse are implemented via a UDF. The momentum and energy Equations are solved using first-order upwind discretization, while the pressure is solved using standard discretization. The SIMPLE method is employed for pressure-velocity coupling. The convergence criterion is set to 10^{-6} for the energy Equation and 10^{-3} for the other Equations. Additionally, a mesh-free solution is considered.

Table 1 Effective properties of the layered surfaces [10][

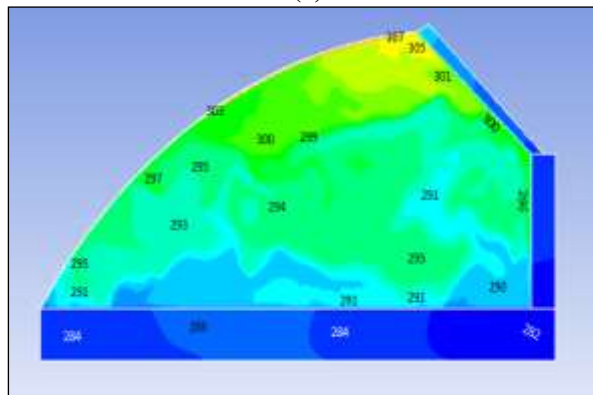
Location	Layers thickness, mm	Density, $\frac{kg}{m^3}$	Specific heat, $\frac{J}{kgK}$	Thermal conductivity, $\frac{W}{mK}$	Emissivity
South roof day time	0.12	1400	1045	0.17	0.9
South roof night time	20	107.8	819	0.03	0.9
North wall inside layer	360	1800	1050	0.81	0.93
North wall middle layer	120	6.9	1329	0.03	
North wall outside layer	120	1800	1050	0.81	0.93
North roof	200	555.8	1091	0.06	0.91
Soil	1000	2050	1010	0.6	0.96

3 RESULTS

The present study is validated by comparing the results with the experimental data of Tong et al. [10]. Figure 8 shows the simulated and measured temperature distributions (K) at 13:00 on February 20, 2004 [10].



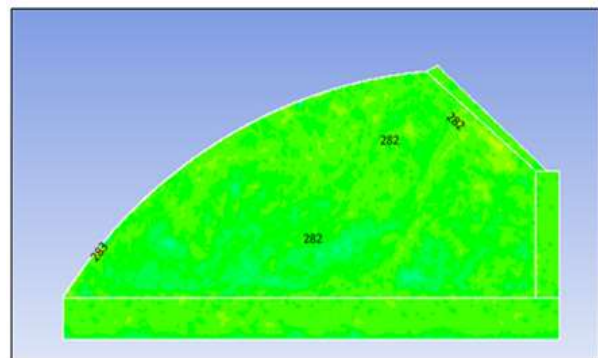
(a)



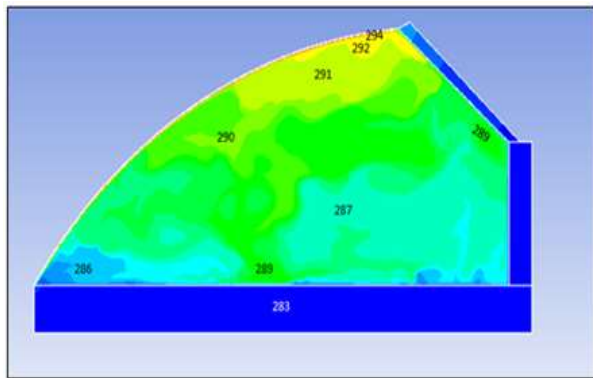
(b)

Fig. 8 Temperature distribution (K): (a): experimental data [10], and (b): numerical result.

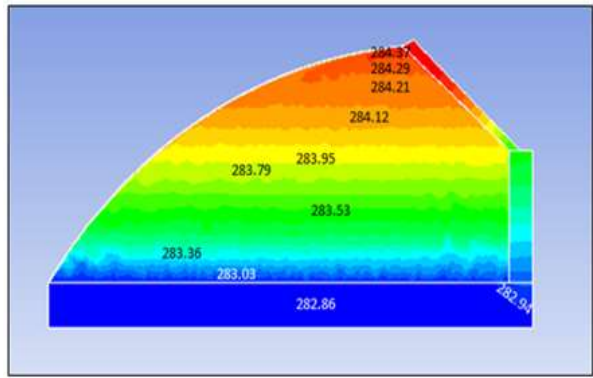
As seen in “Fig. 8”, there is a slight difference between the numerical results and the experimental data. It is concluded that the numerical method used is accurate. Some simplifications are considered in this study; for example, the average properties are considered for the layered structures. The existing difference may be due to these simplifications.



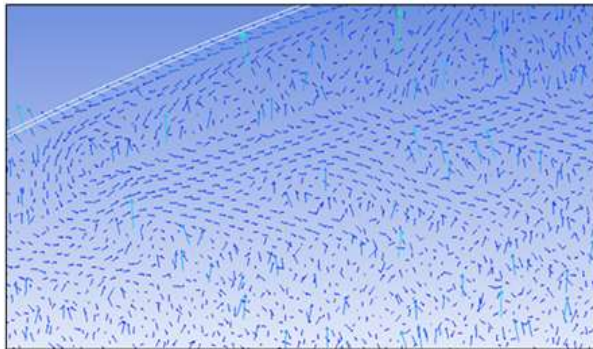
(a)



(b)

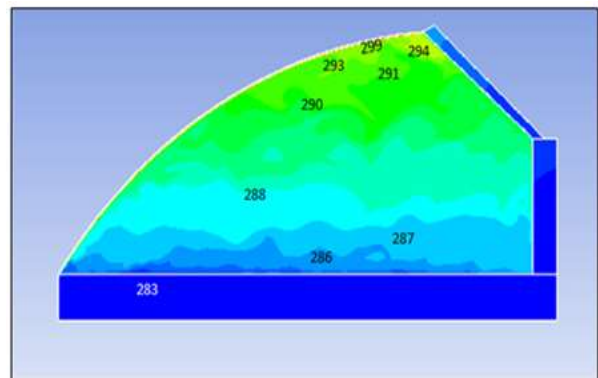


(c)

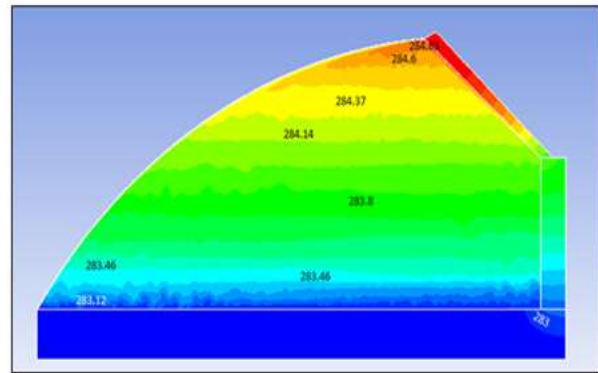


(d)

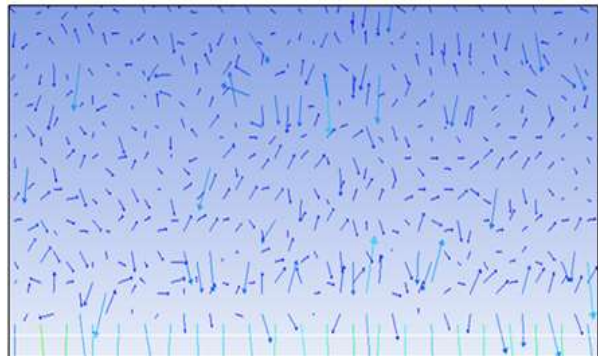
Fig. 9 Temperature distribution (K) at: (a): 8:00, (b): 13:00, and (c): 22:00 (first day). (d): velocity vector at 13:00 near the south roof.



(b)

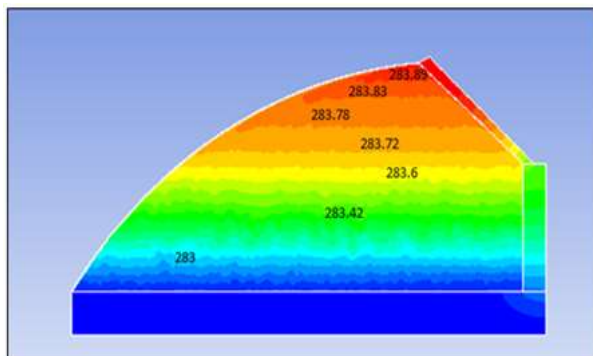


(c)



(d)

Fig. 10 Temperature distribution (K) at: (a): 8:00, (b): 13:00, and (c): 22:00 (second day). (d): velocity vector at 22:00 near the soil surface.



(a)

The above-mentioned method can be used for predicting the temperature distribution inside the greenhouse in different locations. As a case study, the temperature distribution is analyzed in Makran (latitude: 25.3054° N and longitude: 60.6411° E), a semi-desert coastal strip in Baluchestan, Iran, where studying agriculture in this region is significant [30]. The specified climatic conditions are used, considering conduction boundary conditions for inner surfaces and a uniform temperature at a depth of one meter in the soil. Figures 9 and 10 show the temperature contour at different times and the velocity vector near the south roof at certain times.

As seen in “Figs. 9 and 10”, the temperature distribution inside the greenhouse varies at different times due to the time-dependent nature of the incident solar radiation flux. This capability to predict the climatic conditions within the greenhouse can provide valuable insights for optimizing crop production. Understanding how temperature fluctuations correlate with solar radiation over time allows for better management of growing conditions, enhancing the overall efficiency and yield of agricultural practices.

Figures 9 and 10(d) illustrate the fluid motion caused by natural convection due to the temperature differences inside the greenhouse. This highlights the significant role of natural convection in the heat transfer process, influencing the temperature distribution within the solar greenhouse. As seen in “Figs. 9 and 10(b)”, the variation in temperature distribution is significant at 13:00 on both the first and second days. Figure 11 shows the thermal variation along horizontal lines at different y-coordinate levels.

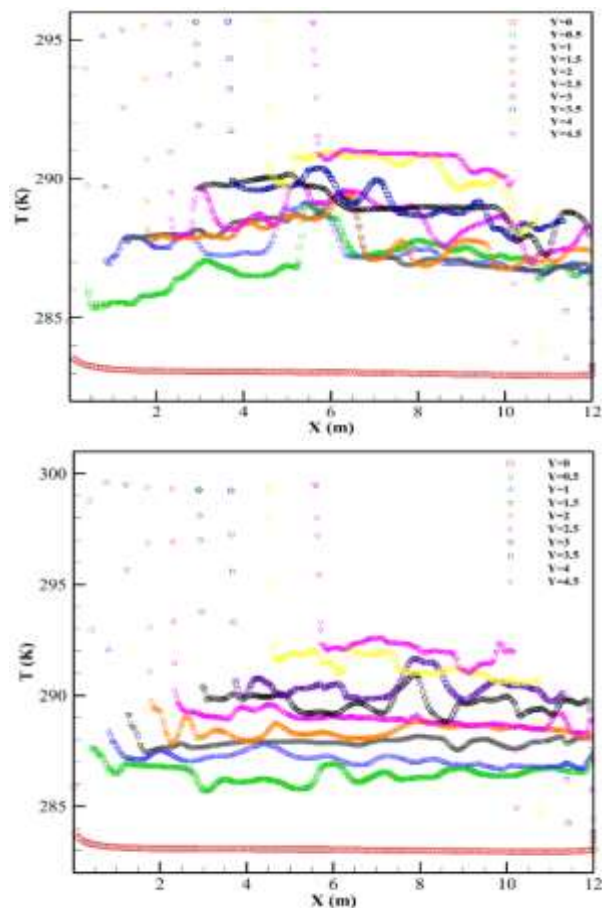


Fig. 11 Temperature distribution along different horizontal lines at: (a): 13:00 (first day), and (b): 13:00 (second day). The center of the coordinates is shown in “Fig. 1”.

The variation in temperature distribution along these horizontal lines is evident in “Fig. 11”, clearly indicating

that the highest temperature occurs near the south roof. Visualizing the thermal distribution along different hypothetical horizontal lines inside the greenhouse is valuable for agricultural purposes in Makran, as it enables accurate prediction of thermal conditions.

4 CONCLUSIONS

This study utilizes the finite volume method with ANSYS Fluent to solve the continuity, Navier-Stokes, and energy Equations, aiming to model the climatic conditions inside a two-dimensional solar greenhouse. The Equations governing the solar radiation model and transient external climatic conditions are detailed and utilized to validate the study against experimental data. As a case study, the study predicts the temperature distribution inside a solar greenhouse in Makran, Iran. The transient nature of boundary conditions results in varying thermal conditions inside the greenhouse at different times. Furthermore, the findings reveal spatial variations in thermal distribution behavior. The research highlights the significant role of natural convection in influencing thermal distribution within the greenhouse. The results demonstrate the capability of the numerical method to accurately simulate the thermal behavior of solar greenhouses, as evidenced by the strong agreement between numerical predictions and experimental data. Consequently, accurate prediction of temperature distribution is crucial for advancing agricultural practices in solar greenhouses.

REFERENCES

- [1] Tawalbeh, M., Aljaghoub, H., Alami, A., and Olabi, A., Selection Criteria of Cooling Technologies for Sustainable Greenhouses: A Comprehensive Review, *Thermal Science and Engineering Progress*, Vol. 38, 2023, pp. 101666, <https://doi.org/10.1016/j.tsep.2023.101666>.
- [2] Ding, D., Design Strategies of Passive Solar Greenhouses: A Bibliometric and Systematic Review, *Ain Shams Engineering Journal*, Vol. 15, No. 5, 2024, pp. 102680, <https://doi.org/10.1016/j.asej.2024.102680>.
- [3] Garg, H. P., *Advances in Solar Energy Technology, Volume 3 Heating, Agricultural and Photovoltaic Applications of Solar Energy* (Softcover Reprint of the Original 1st ed. 1987), Springer Dordrecht, Netherlands, Chap. 5, 2011.
- [4] Fatnassi, H., Bournet, P. E., Boulard, T., Roy, J. C., Molina-Aiz, F. D., and Zaaboul, R., Use of Computational Fluid Dynamic Tools to Model the Coupling of Plant Canopy Activity and Climate in Greenhouses and Closed Plant Growth Systems: A Review, *Biosystems Engineering*, Vol. 230, 2023, pp.

- 388–408,
<https://doi.org/10.1016/j.biosystemseng.2023.04.016>.
- [5] Okushima, L., Sase, S., and Nara, M., A Support System for Natural Ventilation Design of Greenhouse Based on Computational Aerodynamics, *Acta Horticulturae*, Vol. 248, No. 13, 1989, pp. 129–136, 10.17660/ActaHortic.1989.248.13.
- [6] Sase, S., Takakura, T., and Nara, M., Wind Tunnel Testing on Airflow and Temperature Distribution of a Naturally Ventilated Greenhouse, *Acta Horticulturae*, Vol. 148, No. 42, 1984, pp. 329–336, 10.17660/ActaHortic.1984.148.42.
- [7] Mistriotis, A., Bot, G. P., Boulard, T., Feuilloley, P., Papadakis, G., Picuno, P., and Scarascia-Mugnozza, G., *New Techniques in Greenhouse Ventilation Analysis*, AGENG 96 International Conference on Agricultural Engineering, Madrid, 1996, pp. 392–393.
- [8] Bartzanas, T., Boulard, T., and Kittas, C., Numerical Simulation of the Airflow and Temperature Distribution in a Tunnel Greenhouse Equipped with Insect-Proof Screen in the Openings, *Computers and Electronics in Agriculture*, Vol. 34, 2002, pp. 207–221, 10.1016/S0168-1699(01)00188-0.
- [9] Molina-Aiz, F. D., Valera, D. L., and Alvarez, A. J., Measurement and Simulation of Climate inside Almería-Type Greenhouses using Computational Fluid Dynamics, *Agricultural and Forest Meteorology*, Vol. 125, 2004, pp. 33–51, 10.1016/j.agrformet.2004.03.009.
- [10] Tong, G., Christopher, D. M., and Li, B., Numerical Modelling of Temperature Variations in a Chinese Solar Greenhouse, *Computers and Electronics in Agriculture*, Vol. 68, 2009, pp. 129–139, 10.1016/j.compag.2009.05.004.
- [11] Rodriguez, C. E. A., Velazquez, J. F., Heat and Mass Transfer - Advances in Science and Technology Applications, 1st ed., Intech Open, London, United Kingdom, Chap. 6, 2019.
- [12] Sadodin, S., Kashani, T., Numerical Investigation of a Solar Greenhouse Tunnel Drier for Drying of Copra, arXiv preprint arXiv: 1102.2522, 2011, 10.48550/arXiv.1102.4522.
- [13] Lokeswaran, S., Eswaramoorthy, M., An Experimental Analysis of a Solar Greenhouse Drier: Computational Fluid Dynamics (CFD) Validation, *Energy Sources, Part A: Recovery, Utilization, and Environmental Effects*, Vol. 35, No. 21, 2013, pp. 2062–2071, 10.1080/15567036.2010.532195.
- [14] Deiana, A., Fabrizio, E., and Gerboni, R., Energy Performance Optimization of Typical Chinese Solar Greenhouse by Means of Dynamic Simulation, *International Conference on Agriculture Engineering*, Zurich, 2014, pp. 1–8.
- [15] Chen, C., Ling, H., Zhai, Z., Li, Y., Yang, F., Han, F., and Wei, S., Thermal Performance of An Active-Passive Ventilation Wall with Phase Change Material in Solar Greenhouse, *Applied Energy*, Vol. 216, 2018, pp. 602–612, 10.1016/j.apenergy.2018.02.130.
- [16] Tong, G., Christopher, D. M., Sensitivity Analysis of the Air Temperature Variations in a Chinese Solar Greenhouse, *Acta Horticulturae*, Vol. 1170, 2017, pp. 71–78, 10.17660/ActaHortic.2017.1170.7.
- [17] He, X., Wang, J., Guo, S., Zhang, J., Wei, B., Sun, J., and Shu, S., Ventilation Optimization of Solar Greenhouse with Removable Back Walls Based on CFD, *Computers and Electronics in Agriculture*, Vol. 149, 2018, pp. 16–25, 10.1016/j.compag.2017.10.001.
- [18] Esmaeli, H., Roshandel, R., Optimal Design for Solar Greenhouses Based on Climate Conditions, *Renewable Energy*, Vol. 145, 2020, pp. 1255–1265, 10.1016/j.renene.2019.06.090.
- [19] Currie, I. G., *Fundamental Mechanics of Fluid*, 3rd ed., Marcel Dekker Inc., New York, USA, 2003, pp. 3–40.
- [20] ANSYS, *ANSYS Fluent User's Guide*, Ver. 12, Canonsburg, Pennsylvania, USA, 2009.
- [21] Yang, D. K. W., Abakr, Y. A., and Ghazali, N. M., CFD Investigation of the Heat Transfer between an External Heat Source and the Regenerator of a Thermoacoustic Engine, *Procedia Engineering*, Vol. 56, 2013, pp. 835–841, 10.1016/j.proeng.2013.03.204.
- [22] Berdahl, P., Fromberg, R., Thermal Radiance of Clear Skies, *Solar Energy*, Vol. 29, 1982, pp. 299–314.
- [23] Alizadeh, A., *The Principles of Applied Hydrology*, 36th ed., Imam Reza (AS) University, Mashhad, Iran, 2013.
- [24] Tiwari, G. N., *Solar Energy Fundamentals, Design, Modelling and Applications*, 1st ed. Narosa, New Delhi, India, 2002.
- [25] Duffie, J. A., Beckman, W. A., *Solar Engineering of Thermal Process*, 4th ed., John Wiley & Sons, Inc. Hoboken, New Jersey, 2013.
- [26] Padilla, R. V., Simplified Methodology for Designing Parabolic through Solar Power Plants, Ph.D. Dissertation, Department of Chemical and Biomedical Engineering, University of South Florida, Tampa, FL, Apr. 2011.
- [27] Garzoli, K., A Simple Greenhouse Climate Model, *Acta Horticulturae*, Vol. 174, 1985, pp. 393–400, 10.17660/ActaHortic.1985.174.52.
- [28] Garzoli, K. V., Blackwell, I., An Analysis of the Nocturnal Heat Loss from a Single Skin Plastic Greenhouse, *Journal of Agricultural Engineering Research*, Vol. 26, No. 3, 1981, pp. 204–214, 10.1016/0021-8634(81)90105-0.
- [29] Baille, A., Lopez, J. C., Bonachela, S., Gonzalez-Real, M. M., and Montero, J. I., Night Energy Balance in a Heated Low-Cost Plastic Greenhouse, *Agricultural and Forest Meteorology*, Vol. 137, 2006, pp. 107–118, 10.1016/j.agrformet.2006.03.008.
- [30] Noorisameleh, Z., Gough W. A., The Challenge of Climate Change in Agriculture Management in the Persian Gulf-Oman Sea Coasts in Iran, *Transforming Coastal Zone for Sustainable Food and Income Security*. Springer, Cham, 2022, pp. 887–893.